



Aix Marseille Université

Institut Fresnel

École doctorale 352 : Physique et sciences de la matière

Sources optiques fibrées solitoniques pour la spectroscopie et la microscopie non linéaires

Thèse pour obtenir le grade universitaire de docteur
Discipline : Optique, photonique et traitement d'image
Présentée par

Sarah SAINT-JALM

Soutenue le 25 novembre 2014 devant le jury :

Christophe FINOT	Université de Bourgogne	Rapporteur
Marcus MOTZKUS	Heidelberg University	Rapporteur
Albert STOLOW	National Research Council Canada	Examineur
Hervé RIGNEAULT	Institut Fresnel	Directeur de thèse
Esben R. ANDRESEN	Institut Fresnel	Co-directeur de thèse
Alexandre KUDLINSKI	Université Lille 1, PhLAM	Invité



Aix Marseille University

Fresnel Institute

Doctoral school: Physics and science of matter

Soliton-based fiber light sources for nonlinear spectroscopy and microscopy

A thesis submitted for the degree of Doctor of Philosophy

Specialty: Optics, photonics and image processing

Presented on the 25th of November 2014 by

Sarah SAINT-JALM

Defense committee:

Christophe FINOT	Université de Bourgogne
Marcus MOTZKUS	Heidelberg University
Albert STOLOW	National Research Council Canada
Hervé RIGNEAULT	Fresnel Institute
Esben R. ANDRESEN	Fresnel Institute
Alexandre KUDLINSKI	Lille 1 University, PhLAM

Acknowledgments

Three years have past, and so much has happened. I remember the younger version of myself, few years ago, looking up to the majestic PhD Students in all there smartness and glory, thinking that I wouldn't, I couldn't *ever* become one of them. Wrong! I became one of them, and I even managed to make it through the Terrible and Horrible Third Year. And I am so grateful to the many people who, each in their own way, helped me to get there.

First of all, I would like to thank to the directors of the Fresnel Institute, Hugues Giovannini and then Stefan Enoch, for welcoming me in the lab for three years.

Then, I would like to deeply thank Christophe Finot and Marcus Motzkus for reviewing my manuscript, as well as Albert Stolow and Alexandre Kudlinski for accepting to be part of my defense committee. It has been an honor to present you my work.

I am forever grateful to Hervé Rigneault, for giving me the opportunity to work with him, for taking the time off his busy schedule to follow the progress of my work week after week and giving me invaluable guidance, advises and support. Thank you for making Mosaic such a wonderful working place, thank you for inspiring us with your positivity and your scientific vision.

A big big big thank you goes of course to Esben, for always being there to show me how to do everything I had to do, and to answer all my stupid questions while saying they were not stupid. Thank you also for reading and patiently correcting all of my drafts, for the papers and for this manuscript.

Thanks again to Alexandre Kudlinski and the PhLAM laboratory in Lille for providing us with the SC-PBG fibers. Thanks also to Karim Bendahmane for sharing his knowledge about the fiber and showing me how to handle it.

I thank Ludovic Jullien for his insights and suggestions on the chemistry part of this work, Patrick Ferrand for his infinite Labview knowledge and more specifically for helping me design the softwares I used, and Naveen Balla for his help with the pump-probe setup and samples.

A special thanks goes to Pascal Berto, for guiding me through the maze of lock-in amplifiers and SRS, and always being so helpful.

Finally I would like to thank one more time Nicolas Sandeau and Dominique Chauvat for introducing me to my Master's studies that were the starting point of all this.

Now here comes the fun part. From the bottom of my heart, I would like to thank the whole Mosaic group, and all the Fresnel people who ended up hanging out with us. It has been a real pleasure to work with and next to all of you during all this time, thanks to all for being awesome colleagues and friends. Thanks for the moral support, for the laughs, for the lunches and coffee breaks, for the dinners at Mido and elsewhere, for the movie nights and the game nights, for the Calanques hikes, the road trips and the beach sessions, for the housewarming parties and the non-housewarming parties, and above all, for the daily friendliness that made me feel like I belonged.

I thank my many ex- and future ex- office buddies: Deep for all the fun and crazy craziness; Carolina for always being so awesomely random and sweet (and also Louwrens, hi Louwrens!); Wei for being so nice and always bringing cool stuff from China; Juan for not getting too mad when I'm being crazy; and of course César, Xiao, Satish, Saurav and Olivier.

Thanks to Zola, aka Nicest Person Alive, for being so welcoming and friendly, for all the moral support, for all of our conversations and all the good times we had together. Thanks to Chadi, Soufiane (and George!), we missed having you when you left! Also thanks to the others who left, for leading the way: Pascal again, Pierre, Alicja, Dora, Céline and Alla.

Many many misc thanks:

Paulina for all our conversations; Xueqin, Shérazade, and Deep again for being my thesis-writing team mates; Hilton (and Madeleine) for the World Cup screenings (and for taking care of my cat!); Haitham for the breakfasts in Vieux-Port; Alberto and Sid for coping with me being obsessively tidy about the lab (take good care of my laser and fiber!); Susmita for the (free) yoga classes; Naveen and Satish again for all the Indian food; Élodie and Ivan for all the coffee room discussions; and of course Simona, Yoann, Vincent, Marie, Tassos, Petru, Dorian, Hongshan (and all those that I'm afraid I forgot...) for all the moments we shared.

A special danke schön to Carsten for being who he is. (And also for feeding me during the critical writing times).

Merci à tous les membres du personnel administratif qui ont toujours été d'une grande disponibilité et d'une extrême gentillesse : Evelyne, Marc, Nelly, Nadège, Magali, Claire, Émilie, Guylène, Josiane. Un grand merci à Alain pour ma platine de microscope, un immense merci à Jean et Frédéric pour nous assister sans relâche dans nos problèmes informatiques. Merci aussi à Alexandre pour toutes les fois où j'ai eu besoin d'une vis spéciale, d'un fusible spécial ou d'une soudure. Une pensée aussi pour Jean-Pierre qui a réalisé plusieurs pièces mécaniques au début de ma thèse.

Ma plus grande gratitude va bien sûr à ma famille, mon socle, ma pierre angulaire, sans qui rien de tout cela n'aurait été possible. Mon père, pour nous avoir élevés dans l'érudition et l'humour glacé. Mon frère et ma sœur, qui sont les personnes les plus chères à mon cœur : merci d'être là, merci de me faire rire, merci de m'écouter me plaindre et de partager avec moi ces douleurs, ces joies et ces ridicules futilités qui font que nous serons toujours liés. Valérie, merci d'avoir été là pour nous tous, nous savons à quel point nous te sommes redevables. Mes grands-parents bien sûr, ainsi que Nathalie, Ivan, et mes cousins Solal et Noé, pour leur soutien inconditionnel. Devrais-je ajouter mon chat à cette liste ? Bien sûr. Merci Mia.

Une pensée pour ma tante Michèle, que nous avons perdue il y a quelques semaines seulement, et pour le reste de la famille Saint-Jalm – Kassi, avec qui nous avons partagé cette peine.

Et finalement je voudrais adresser un dernier mot à ma mère. Quand j'avais 14 ans, je me suis fait la promesse de dédier toutes mes réussites futures à sa mémoire. Je crois que ceci en est une. C'est donc chose faite.

Contents

Introduction	5
1 Chapter 1: Soliton propagation in optical fibers	9
1.1 Optical fibers	9
1.1.1 Classical optical fibers	9
1.1.2 Photonic crystal fibers	12
1.2 Propagation of a pulse of light in a fiber	16
1.2.1 The nonlinear Schrödinger equation	16
1.2.2 Fourier-transform-limited pulses	25
1.2.3 Separate effects of dispersion and nonlinearities	26
1.2.4 Combined effects of GVD and SPM	30
1.3 Soliton dynamics	31
1.3.1 Soliton formation	31
1.3.2 Soliton self-frequency shift	32
1.3.3 Soliton delay	35
1.4 Conclusion	35
2 Chapter 2: Fiber delivery for TPEF and SHG microscopy	37
2.1 Properties of nonlinear microscopy	37
2.2 Fiber delivery for multiphoton microscopy	39
2.3 A solid-core photonic bandgap fiber for high energy solitons	41
2.3.1 Preliminary study	42
2.3.2 Design and characterization of the second SC-PBG	45
2.4 Two photon fluorescence and second harmonic generation	50
2.4.1 Experimental setup	50
2.4.2 Nonlinear spectroscopy	52
2.4.3 Nonlinear microscopy	53
2.5 Conclusion	55
3 Chapter 3: Pump-probe measurements of transient absorption	57
3.1 Transient absorption	57
3.2 Pump-probe experiment with soliton delay	60
3.3 Experimental results	63
3.4 Conclusion	67

4 Chapter 4: Coherent Raman scattering	69
4.1 Principles of coherent Raman scattering	69
4.1.1 Spontaneous Raman scattering	69
4.1.2 Coherent Raman scattering	71
4.2 Spectral focusing	76
4.2.1 Spectral resolution	76
4.2.2 Principle of spectral focusing	77
4.2.3 Chirping femtosecond pulses	79
4.3 Experimental setup	82
4.4 Characterization on chlorobenzene	84
4.5 Study of a chemical equilibrium	89
4.6 Signal-to-noise ratio	93
4.7 Conclusion	94
Conclusions and perspectives	95
Appendix A	I
Appendix B	V
1 Gaussian pulse	V
2 Sech-squared pulse	VI

List of publications

Some of the results included in this manuscript have been published in peer-reviewed journals and conference proceedings. The list of these publications, up to date on the 1st of October 2014, is presented below.

Journal publications

1. S. Saint-Jalm, P. Berto, L. Jullien, E. R. Andresen and H. Rigneault, “Rapidly tunable and compact coherent Raman scattering light source for molecular spectroscopy” *Journal of Raman Spectroscopy* **45**, 515 – 520 (2014).
<http://dx.doi.org/10.1002/jrs.4514>
2. S. Saint-Jalm, E. R. Andresen, P. Ferrand, A. Bendahmane, A. Mussot, O. Vanvincq, G. Bouwmans, A. Kudlinski and H. Rigneault, “Fiber-based ultrashort pulse delivery for nonlinear imaging using high-energy solitons”, *Journal of Biomedical Optics* **19**, 086021 (2014).
<http://dx.doi.org/10.1117/1.JBO.19.8.086021>

Conference proceedings

1. E. R. Andresen, P. Berto, S. Saint-Jalm and H. Rigneault, “Stimulated Raman scattering microscopy by spectral focussing and fiber-generated soliton as Stokes pulse” *Proceedings of SPIE* **8226**, Multiphoton Microscopy in the Biomedical Sciences XII, 822606 (2012)
<http://dx.doi.org/10.1117/12.906993>
2. A. Bendahmane, A. Mussot, O. Vanvincq, G. Bouwmans, A. Kudlinski, S. Saint-Jalm, E. R. Andresen and H. Rigneault, “Solid-core photonic bandgap fiber for the generation of tunable high-energy solitons.” *Workshop on Specialty Optical Fibers and their Applications* (Optical Society of America), paper W3.36 (2013).
<http://dx.doi.org/10.1364/WSOF.2013.W3.36>

Conference presentations

Parts of this works have also been presented at several international conferences, under the form of oral or poster presentations. These communications are listed here.

1. S. Saint-Jalm, E. R. Andresen and H. Rigneault. Oral presentation: “Fiber based ultra-short pulse delivery for nonlinear spectroscopy and microscopy using high energy solitons.” MicroCOR Workshop: New Frontiers in Non-linear Raman Microscopy, Heidelberg, Germany (2014).
2. S. Saint-Jalm, E. R. Andresen and H. Rigneault. Oral presentation: “Fiber based ultra-short pulse delivery for nonlinear imaging using high energy solitons.” 1st MicroCOR winter school on Chemical Imaging by Coherent Raman and nonlinear microscopy, Les Houches, France (2014).
3. S. Saint-Jalm, E. R. Andresen and H. Rigneault. Oral presentation: “A compact light source for coherent Raman (CARS/SRS) spectroscopy and microscopy.” 12th European Conference on Nonlinear Optical Spectroscopy (ECONOS), Exeter, UK (2013).
4. S. Saint-Jalm, E. R. Andresen and H. Rigneault. Poster presentation: “A compact light source for coherent Raman spectroscopy and microscopy.” Conference on Coherent Raman Scattering Microscopy (MicroCARS 2012), Naurod, Germany (2012).

Introduction

The control of light propagation in optical fibers over long distances constituted a major technological advance which participated in the digital revolution that changed the world at the end of the 20th century. The transmission of information and energy from one place to the other through such a space-saving, flexible and affordable medium has found an immense variety of applications, from telecommunications to industrial micro-machining. In particular, the field of medical imaging has made admirable progress upon the use of optical fibers for diagnosis tools called endoscopes. The word “endoscope” comes from ancient Greek ἔνδον (éndon) that means “in”, “within”; and σκοπέω (skopéō) that means “I look”, “I examine”. The purpose of an endoscope is indeed to look inside the human body, by introducing a fiber or a tube through natural orifices into the organs the physician wants to observe. The light is sent from outside into the body, and the information is transmitted the opposite way under the form of images. In the majority of the endoscopes used on a daily basis and all over the world, the observation technique is based on a simple white-light illumination system and a small camera that acquires and transmits the images. The success of this method is undeniable, as it improved the diagnosis for many diseases.

However, it would be of great benefit for the diagnosis of several diseases if endoscopy techniques could go beyond white-light imaging. For instance, in the case of colorectal cancer, it is impossible to know whether a polyp (an abnormal growth of tissue in a mucous membrane) is benign or precancerous from a white-light observation. It is necessary to proceed to a biopsy of the polyp to determine its nature, which is an invasive operation that could be avoided if the imaging technique was able to analyze the structure on site. This is why research is now focused on finding new contrasts in endoscopy, that could bring structural, chemical, and biological knowledge about the tissue, on top of the information provided by white-light imaging. Among the candidate contrasts to be applied in endoscopy, nonlinear processes are of particular interest. A wide range of nonlinear effects have been discovered and are now used in numerous biology labs for microscopy. They take their origin in the simultaneous absorption of several photons, and the emission of one photon of a different energy. For instance, two-photon excited fluorescence (TPEF), second-harmonic generation (SHG) and third-harmonic generation (THG) are three phenomena generating useful contrasts for the imaging of biological samples. They allow

to reveal structures and biological properties that are invisible in white-light microscopy, sometimes without the need of staining the sample in any way. For example, collagen fibers generate a strong endogenous SHG signal. Coherent Raman scattering techniques, such as coherent anti-Stokes Raman scattering (CARS) and stimulated Raman scattering (SRS), permit to go even further in this direction. Indeed, they are inherently label-free as they probe the molecular vibrations present in the sample.

In order to implement nonlinear microscopy techniques in endoscopic schemes, several challenges have to be addressed. One of them comes from the fact that generating nonlinear signals in a sample requires high excitation powers. This problem has been solved for regular microscopy with the discovery and development of pulsed lasers, which are able to generate ultra short pulses with peak powers high enough to generate observable signals, while maintaining the average powers at levels low enough to avoid photodamage. The propagation of those ultra-short pulses in optical fibers is not trivial precisely because of their high peak powers. In classical fibers, the light propagates in silica, whose dispersion and nonlinear properties distort and broaden the high energy pulses. Several strategies have been developed to circumvent this problem, taking inspiration from the research in the field of optical fibers.

In particular, the invention of photonic crystal fibers (PCFs) has widened the range of possible technical options to tackle problems of ultra-short pulses fiber delivery. Instead of having a core and a cladding made of two distinct materials of different refractive index, PCFs have a micro-structured cladding surrounding either a solid or hollow core. The properties of such fibers then strongly depend on the design of the micro-structure, resulting in an abundant production of new fibers with new designs and new properties. Some of those fibers are able to sustain the propagation of a soliton, a pulse that has the remarkable property of preserving its shape throughout its propagation in the fiber. Solitons possess a set of unique features that makes them of great interest for fiber delivery and nonlinear imaging applications. In addition to the fact that their shape and duration stay unchanged during the propagation, their wavelength and delay are tunable by changing the power of the light at the input of the fiber.

In this work, several light sources based on soliton generation were designed and realized for nonlinear spectroscopy and microscopy. This manuscript is organized as follows:

Chapter 1: A quick review of the different kinds of optical fibers is presented, from the classical step-index fiber to the most recent PCFs. Then, the analytical expressions for pulse propagation in a single-mode fiber are derived from

Maxwell's equations. From this analysis arises the concept of soliton. Finally, the properties of solitons are presented and explained.

Chapter 2: The design and properties of a new fiber are presented. This fiber was fabricated specifically to generate high energy solitons compatible with non-linear microscopy. The fiber delivery abilities of the soliton-based scheme are assessed by realizing TPEF and SHG images of biological samples. The spectroscopic capabilities of the system, provided by the wavelength tuning of the soliton, are also explored.

Chapter 3: The delay shift of solitons depending on the variation of input power is put to use in time-resolved measurement of transient absorption in a pump-probe configuration. The delay scanning based on the MHz variation of input power is shown to be equivalent to the mechanical delay scanning.

Chapter 4: A CRS setup based on soliton generation and spectral focusing is presented. The soliton wavelength shift allows to get two synchronized beams of different frequencies, that are then used as pump and Stokes. The femtosecond pulses are chirped to achieve a good spectral resolution. Both CARS and SRS signals are obtained, and a chemical equilibrium is monitored to prove the interest of the method.

1 Chapter 1: Soliton propagation in optical fibers

1.1 Optical fibers

1.1.1 Classical optical fibers

Optical fibers are cylindrical dielectric waveguides in which light can propagate at optical frequencies along its main axis. Since the first attempts to realize optical guidance in a fiber in the beginning of the 20th century, several breakthroughs in the understanding, design and fabrication of optical fibers have led to a tremendously active field of research as well as to many applications. In the telecommunication domain in particular, optical fibers have reached a mass-production level and are now widely spread and used throughout the entire world to transmit information. Other applications include sensing, medical imaging, power transmission, or even illumination and decoration. On a more fundamental level, optical fibers are used in research and industry, for example in spectroscopy, optical imaging or fabrication of lasers and optical amplifiers.

The propagation of light in an optical fiber can be described in two main ways. If the diameter of the core where the light propagates is big enough compared to the wavelength of the light, a geometrical (or ray optics) approach can be appropriate to describe some of the properties of the fiber. However, in many cases, it is necessary to use electromagnetic theory to describe the set of electromagnetic waves propagating in the fiber, called the *modes* of the fiber [1].

Ray optics representation

The first fiber design found to efficiently transmit light from one end to the other consists in a cylindrical core of high refractive index (n_1) where the light propagates, surrounded by a cladding of low refractive index (n_2) that traps the light through total internal reflection. These fibers are called step-index fibers. Most of the optical fibers are made of fused silica (SiO_2), and the refractive index difference can be slightly modified by chemical doping. The difference in refractive index between the core and the cladding is often very small: $(n_1 - n_2)/n_1 \ll 1$.

Snell's law of refraction predicts a total reflection of light at an interface between two materials of refractive index n_1 and n_2 (with $n_1 > n_2$), for incident angles $\alpha > \alpha_{\min} = \sin^{-1}(n_2/n_1)$ (see Fig. 1.1). For those angles, the light is transmitted through the fiber after multiple reflections. Therefore, there is a cone of light at the input of the fiber for which the incident angles on

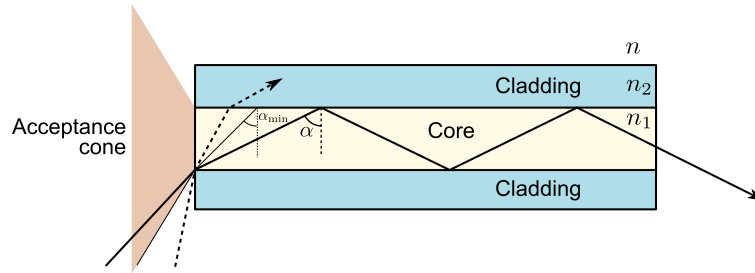


Figure 1.1: Light transmission in a step-index fiber based on multiple total-internal reflections (TIR) at the interface between the core (refractive index n_1) and the cladding (refractive index n_2). The acceptance cone is defined by the minimum incidence angle α_{\min} allowing TIR. The rays entering the fiber from outside this cone will experience power loss due to refraction, and all their energy will be dissipated in the cladding after few reflections.¹

the interface core/cladding are higher than α_{\max} , and for which the light is transmitted. Outside of this cone, the light escapes through refraction in the cladding. This cone of light defines the numerical aperture of the optical fiber. By applying Snell's law to the end of the fiber, the numerical aperture NA can be written:

$$\text{NA} = n \sin \left(\frac{\pi}{2} - \alpha_{\min} \right) = \sqrt{(n_1^2 - n_2^2)}, \quad (1.1)$$

where n is the refractive index of the outside medium. From the simple picture described above, one could assume that any ray entering the fiber within the cone defined by NA can be transmitted. However, when interference effects are taken into account, it becomes clear that only a discrete set of rays are allowed to propagate in the fiber. This is illustrated in Fig. 1.2(a): each ray corresponds to one mode. The drawback of this kind of fiber is the intermodal dispersion. Indeed, there will be a delay between the exit time of two modes, as the rays follow different optical paths.

In graded-index fiber, the refractive index continuously decreases from the central axis to the cladding. It is for example possible to design fibers with a parabolic refractive index profile, where the rays are continuously deflected instead of propagating along straight lines between two reflections. In this case, the intermodal dispersion induced by the fiber is decreased because the difference between the optical paths of small and large incident angles is minimized. In graded-index fiber, the NA varies as a function of the radial distance. It is maximum at the center and decreases when the rays enter closer to the cladding.

¹Modified from image by Gringer, licensed under Public domain via Wikimedia Commons.
<<http://commons.wikimedia.org/wiki/File:Optical-fibre.svg>>

This results in less modes sustained by the fiber and less transmitted light compared to a step-index fiber.

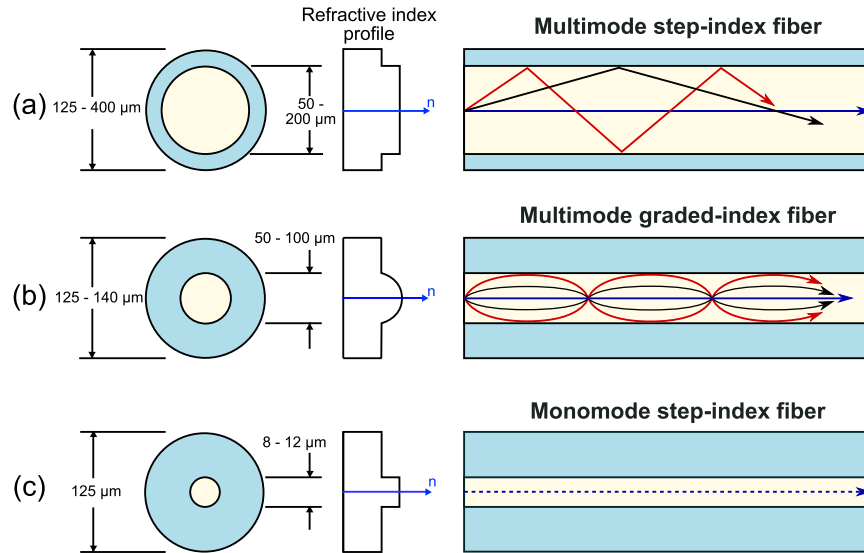


Figure 1.2: Typical dimensions, refractive index profiles, and rays paths in (a) multimode step-index fiber, (b) multimode graded-index fiber and (c) monomode step-index fiber. ²

Mode theory of cylindrical waveguides

The ray optics approach only gives a partial understanding of the light propagation in a fiber. If the diameter of the core is very small, it is even completely irrelevant. To go further, it is necessary to solve Maxwell's equations to find the solutions to the propagation equation that satisfies the boundary conditions. We are interested in the propagation of the light along the main axis of the fiber z , so an important parameter is the propagation constant β , which is the axial component of the wavevector \vec{k} ($|\vec{k}| = k = 2\pi/\lambda$).

Several kinds of modes can be sustained by the fiber. First, the guided modes are the ones that were discussed above. They are trapped in the core of the fiber and differ from each other by the electric field pattern along the fiber's cross-section.

The cladding modes originate from the light outside of the acceptance angle that is then refracted and trapped in the cladding.

²Modified from image by Mrzeon, licensed under Creative Commons Attribution-Share Alike 3.0-2.5-2.0-1.0 via Wikimedia Commons
<http://commons.wikimedia.org/wiki/File:Optical_fiber_types.svg>

Finally, the leaky modes are partially confined to the core region but are attenuated as they propagate. The difference between guided and leaky modes is set by the cutoff condition. A mode remains guided if

$$n_2k < \beta < n_1k, \quad (1.2)$$

the lower boundary being the cutoff condition. If $\beta < n_2k$, the mode is leaky. In classical fibers, this is equivalent to the TIR limit. As β is the projection of $n_1\vec{k}$ onto the z axis, its maximum value is n_1k . The maximum angle allowed by TIR satisfies $\sin(\alpha) = n_2/n_1$. The projection of $n_1\vec{k}$ onto the z axis then gives $\beta = n_2k$ as the minimum value of the propagation constant.

It is customary to introduce the V parameter, also called normalized frequency:

$$V = \frac{2\pi a}{\lambda} \text{NA} = \frac{2\pi a}{\lambda} \sqrt{(n_1^2 - n_2^2)}, \quad (1.3)$$

where a is the radius of the core. Except for the fundamental mode, all modes are cut off when $\beta = n_2k$, which happens at different values of V depending on the modes. For $V < 2.405$, only the fundamental mode is left, then the fiber is monomode. The number of modes M in a multimode fiber can be estimated by:

$$M \approx \frac{V^2}{2}. \quad (1.4)$$

This is the equivalent of the quantization of modes due to interferences in the classical pictures. The number of modes (of angles in the ray optics interpretation) is limited, then if the core becomes smaller, the number of modes decreases until only the one at $\alpha = \pi/2$ is left.

1.1.2 Photonic crystal fibers

A new kind of optical fibers was developed in the 1990s by the group of Philip St. J. Russell [2], called photonic crystal fibers (PCFs). The core of a PCF is made of a periodic arrangement of microscopic air holes running along the whole length the fiber, otherwise made of silica. Their idea was to trap the light in a hollow core by preventing its propagation in the cladding by the means of a 2-D *photonic crystal*. Photonic crystals are periodically organized nanostructures that creates “stop-bands”, or photonic band gaps (PBG), preventing the propagation of light in one, two or three dimensions. However, depending on the design of the fiber, the trapping of the light and its propagation in the core does not always come from the PBG effect. Nevertheless, the name PCF is commonly used for all the micro-structured fibers.

The properties of the fiber strongly depend on the design of the structure of the core. Those properties can also be modified by changing the chemical composition of the fiber, for example by doping the silica. A wide diversity of

PCFs has been fabricated and used for applications as diverse as fiber-optical parametric oscillators and amplifiers [3, 4], artificial black holes [5] or intense supercontinuum generation [6, 7] for fluorescence microscopy [8], optical metrology [9, 10] and optical coherence tomography [11, 12].

Modified total internal reflection

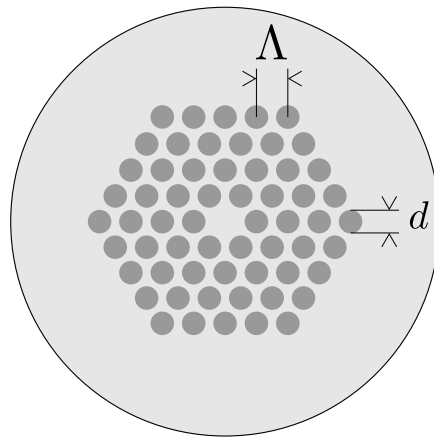


Figure 1.3: Scheme of a solid-core PCF. The light gray area is silica and the darker inclusions are air holes. d is the diameter of a hole, and Λ is the pitch.

The simplest kind of PCFs has a hexagonal pattern of air holes, with one hole missing in the center (see Fig. 1.3), where the light propagates. The guiding is due to the effective refractive index of the silica/air micro-structure (the photonic crystal cladding) compared to the center, only made of silica. Those two areas are equivalent to the cladding and core in classical optical fibers. Two important parameters are the diameter of the hole d and the hole-to-hole distance (or pitch) Λ . The mechanism of guidance is conceptually similar to the TIR in classical fibers, but an advantage of PCFs is the possibility to tailor some of their properties by changing d and/or Λ . For instance, the dispersion of a fiber can be modified by changing the design. This is a big advantage compared to classical fibers where the value of dispersion cannot be changed too far away from the dispersion of the bulk material. In silica fibers, the group-velocity dispersion (GVD) is positive until about $\lambda = 1.3 \mu\text{m}$, which is the zero-dispersion wavelength (ZDW) of silica. With PCFs, the ZDW can be pushed down to optical frequencies.

Another remarkable feature of PCFs is their ability to exhibit single-mode

behavior for a wide range of wavelengths [13]. The V parameter can be written:

$$V = \frac{2\pi a}{\lambda} \sqrt{(n_S^2 - n_{\text{FSM}}^2)}, \quad (1.5)$$

where n_S is the refractive index of silica, and n_{FSM} is the fundamental space-filling mode, which corresponds to the effective refractive index of the infinite photonic crystal cladding without the core.

In classical fibers, V increases when λ decreases, so the fiber becomes multi-mode at short wavelengths. In PCFs, n_{FSM} is wavelength-dependent. Indeed, n_{FSM} is defined as the average index of the photonic crystal cladding, weighted by the field distribution. At shorter wavelengths, the light is more concentrated in the silica, which raises the effective refractive index and decreases the V parameter. Russell and co-workers showed that for $d/\Lambda < 0.4$, a PCF can exhibit an endlessly single mode behavior, the transmission range being limited only by bend losses [14]. This phenomenon has been illustrated by the modal sieve (or modal filtering) picture. Each mode can be characterized by its transverse effective wavelength, which is defined as follows:

$$\lambda_{\text{eff}}^i = \frac{2\pi}{\sqrt{k^2 n_i^2 - \beta^2}}, \quad (1.6)$$

where n_i is the refractive index of the material where the light propagates. This is a measure of the characteristic size of the transverse component of the \vec{k} vector, and it indicates whether a mode is likely to be resonant with particular features in the cross-section of the fiber. The fundamental mode has a high transverse effective wavelength, so it stays trapped in the core. Conversely, the higher-order modes have lower transverse effective wavelength, and they can “escape” between the holes. If the holes are bigger (increased d/Λ), some higher order modes can be also trapped.

Finally, one last advantage of PCFs over classical fibers resides in their small core where the strong confinement of the light can lead to increased intensity, which is useful for studying and using nonlinear effects. However, as the modal filtering is only dependent on the d/Λ ratio, it is also possible to design fibers with large cores, by scaling the whole structure. This is the principle of large-mode area fibers, that are useful if one wants to avoid the nonlinear effects caused by the presence of high powers in silica.

Photonic band-gap fibers

For fibers whose core refractive index is higher than the cladding refractive index (like the ones that were just described), PBG guidance can occur, although in practice TIR guiding dominates.

In the opposite case where the core refractive index is lower than the cladding refractive index, TIR cannot operate. Then, the guidance relies only on the PBG effect [15]. The periodic structures create forbidden zones in the frequency/wavevector diagram through Bragg diffraction. This means that for some wavelengths and directions of \vec{k} , the cladding is a perfect 2D photonic crystal and it allows propagation only along the main axis of the fiber.

Hollow-core photonic bandgap (HC-PBG) fibers. In HC-PBG fibers, the light propagates in an air core [16–19]. A key parameter is again d/Λ , that corresponds here to the air filling fraction of the photonic cladding. The width of photonic band gaps increases for increasing d/Λ . In order to get broad transmission bands, d/Λ has to be higher than 0.9. The broadest bands could be achieved for $d/\Lambda = 1$, but fabricating such a fiber is not feasible.

As the light propagates in air rather than in silica, the fiber can handle very high powers. Consequently, HC-PBG fibers have been used for the fiber delivery of high-energy pulses. The transmission losses of such fibers are theoretically lower than those of conventional all-silica fibers, because the intrinsic transmission of air is much higher than the one of silica. Silica fibers have gone through several decades of technological improvements and have come close to the limit of Rayleigh scattering, with transmission losses as low as 0.15 dB/km. HC-PBG fibers still suffer from losses due to surface roughness. Roberts and co-workers [20] presented a low-loss HC-PBG (1.2 dB/km at 1600 nm) and showed that the design of HC-PBG could be optimized to reach transmission losses of 0.1 dB/km. A trade-off between losses and modality also has to be found, as single-mode HC-PBG have smaller cores and higher losses.

Kagomé fibers. The Kagomé fiber is an interesting type of hollow-core fiber. Indeed, the light propagates in an air core surrounded by an air / silica microstructure, but the fiber does not have photonic band gaps. Its photonic cladding is based on a kagomé lattice of silica [21, 22], whose pattern looks like a Star of David. Its guiding properties are not fully understood, although theoretical studies have developed models to explain its behavior (e.g. [23]). Those fibers exhibit higher losses than other HC-PBG fibers but they have a very wide bandwidth of transmission, which can be put to use in several applications. For instance, Ghenuche and co-workers have taken advantage of the large transmission window of a Kagomé fiber in Raman spectroscopy, where the excitation and the collected signal were transmitted through the same fiber [24]. They have also been used for high power laser beam transmission.

Solid-core photonic bandgap (SC-PBG) fibers. One limit of hollow-core fibers is their fabrication, because the air-filling fraction has to be very high. The

designed fibers are often the result of a trade-off between desired properties and feasibility. In SC-PBG fibers, the core is made of low-index silica, while the photonic cladding is made of an array of high-index silica. For example, Luan and co-workers demonstrated the first SC-PBG fiber with a core made of LLF1 glass and a photonic cladding made of inclusions of SF6 glass. [25]. The possibility to dope silica with diverse rare-earth ions allows to design a wide range of fibers with different properties. The use of SC-PBG fibers is promising in fiber lasers [26, 27] and fiber amplifiers [28], or for the investigation and control of nonlinear effects such as supercontinuum generation and soliton propagation [29–31].

The explanation and understanding of the properties of the wide diversity of PCFs often requires finite element method calculations, or other kind of numerical simulations. However, the analytical description of some properties of PCFs is possible in some cases. In the following, we will discuss the propagation of a pulse of light in a single-mode fiber.

1.2 Propagation of a pulse of light in a fiber

1.2.1 The nonlinear Schrödinger equation

Propagation equation

Like any other electromagnetic phenomenon, the propagation of a pulse of light in a fiber is governed by Maxwell's equations. If there is no free current, no free charge, and the medium is non-magnetic, they can be written:

$$\left\{ \begin{array}{l} \nabla \cdot \mathbf{D} = 0 \\ \nabla \cdot \mathbf{B} = 0 \\ \nabla \times \mathbf{E} = -\frac{\partial \mathbf{B}}{\partial t} \\ \nabla \times \mathbf{B} = \mu_0 \frac{\partial}{\partial t} (\epsilon_0 \mathbf{E} + \mathbf{P}) \end{array} \right. \quad \begin{array}{l} (1.7a) \\ (1.7b) \\ (1.7c) \\ (1.7d) \end{array}$$

By combining Eqs. 1.7c and 1.7d, the propagation equation arises:

$$\nabla \times \nabla \times \mathbf{E}(\mathbf{r}, t) + \frac{1}{c^2} \frac{\partial^2 \mathbf{E}}{\partial t^2}(\mathbf{r}, t) = -\mu_0 \frac{\partial^2 \mathbf{P}}{\partial t^2}(\mathbf{r}, t), \quad (1.8)$$

where $\mathbf{E}(\mathbf{r}, t)$ is the optical electric field in the time domain, \mathbf{r} being the spatial coordinates and $\mathbf{P}(\mathbf{r}, t)$ is the polarization density, describing the reaction of the medium upon excitation by the electric field.

Eq. 1.8 can be adapted into a form suitable for describing the propagation of a pulse in a single-mode fiber by following several steps that will be detailed hereafter [32, 33].

Linear problem

The polarization density is split into a linear and a nonlinear term: $\mathbf{P} = \mathbf{P}_L + \mathbf{P}_{NL}$. First the nonlinear term is set to zero to determine the solution of the linear problem, and then the nonlinear term will be treated as a small perturbation to the system.

The polarization density represents the reaction of the medium upon excitation by an electric field. More precisely, it quantifies the motion of the electrons induced in the medium by the oscillation of the electric field. Due to the inertia of the electrons, the first order susceptibility describing the response of the medium is time dependent, which means that the reaction of the medium is not simultaneous with the excitation. Thus, the linear polarization density can be written:

$$\mathbf{P}_L(\mathbf{r}, t) = \varepsilon_0 \int_{-\infty}^t \chi^{(1)}(\tau) \mathbf{E}(\mathbf{r}, t - \tau) d\tau, \quad (1.9)$$

which is equivalent to the convolution:

$$\mathbf{P}_L(\mathbf{r}, t) = \varepsilon_0 [\chi^{(1)}(t) \otimes \mathbf{E}(\mathbf{r}, t)]. \quad (1.10)$$

Introducing Eq. 1.10 into the propagation equation 1.8:

$$\nabla \times \nabla \times \mathbf{E}(\mathbf{r}, t) + \frac{1}{c^2} \frac{\partial^2 \mathbf{E}}{\partial t^2}(\mathbf{r}, t) = -\varepsilon_0 \mu_0 [\chi^{(1)}(t) \otimes \mathbf{E}(\mathbf{r}, t)]. \quad (1.11)$$

Using the formula for the derivation of a convolution product and the fact that the delta Dirac is the neutral element of the convolution product, we finally get, after factorization:

$$\nabla \times \nabla \times \mathbf{E}(\mathbf{r}, t) + \frac{1}{c^2} \left[(\delta(t) + \chi^{(1)}(t)) \otimes \frac{\partial^2}{\partial t^2} \mathbf{E}(\mathbf{r}, t) \right] = 0, \quad (1.12)$$

where $\delta(t) + \chi^{(1)}(t) = \varepsilon(t)$ is the permittivity tensor.

For solving the linear problem, it is convenient to work in the frequency space, by taking the Fourier transform of the electric field and of the permittivity:

$$\mathbf{E}(\mathbf{r}, t) = \int \tilde{\mathbf{E}}(\mathbf{r}, \omega) e^{-i\omega t} d\omega \quad (1.13)$$

$$\varepsilon(t) = \int \tilde{\varepsilon}(\omega) e^{-i\omega t} d\omega \quad (1.14)$$

By introducing Eqs. 1.13 and 1.14 into Eq. 1.12, it becomes:

$$\nabla \times \nabla \times \int \tilde{\mathbf{E}}(\mathbf{r}, \omega) e^{-i\omega t} d\omega + \frac{1}{c^2} \left[\int \tilde{\varepsilon}(\omega) e^{-i\omega t} d\omega \otimes \frac{\partial^2}{\partial t^2} \int \tilde{\mathbf{E}}(\mathbf{r}, \omega) e^{-i\omega t} d\omega \right] = 0. \quad (1.15)$$

The second derivative with respect to time only acts on the exponential term:

$$\int \nabla \times \nabla \times \tilde{\mathbf{E}}(\mathbf{r}, \omega) e^{-i\omega t} d\omega + \frac{1}{c^2} \left[\int \tilde{\varepsilon}(\omega) e^{-i\omega t} d\omega \otimes (-\omega^2) \int \tilde{\mathbf{E}}(\mathbf{r}, \omega) e^{-i\omega t} d\omega \right] = 0. \quad (1.16)$$

The convolution of the Fourier transform of two functions is equal to the Fourier transform of the product of those functions:

$$\int \nabla \times \nabla \times \tilde{\mathbf{E}}(\mathbf{r}, \omega) e^{-i\omega t} d\omega - \frac{\omega^2}{c^2} \int (\tilde{\varepsilon}(\omega) \tilde{\mathbf{E}}(\mathbf{r}, \omega)) e^{-i\omega t} d\omega = 0. \quad (1.17)$$

In principle,

$$\tilde{\varepsilon}(\omega) = \left(n(\omega) + i \frac{\alpha c}{2\omega} \right)^2, \quad (1.18)$$

where α is the absorption coefficient. However, we consider that $\tilde{\varepsilon}(\omega) = n^2(\omega)$, as the losses are relatively small in silica fibers and will be taken into account later in a perturbative manner. The relation of $n(\omega)$ and $\alpha(\omega)$ with the first-order permittivity $\chi^{(1)}$ is explained in [Appendix A](#).

With Eq. 1.7a and $\tilde{\mathbf{D}} = \tilde{\varepsilon} \tilde{\mathbf{E}}$, we can set $\nabla \cdot \tilde{\mathbf{E}} = 0$, because $n(\omega)$ does not depend on spatial coordinates \mathbf{r} both in the core and in the cladding. This approximation, meant to work in step-gradient index fibers, holds in other cases if index changes occur over length scale much longer than the wavelength.

Then, the factorization of the integral gives:

$$\int \left(\Delta \tilde{\mathbf{E}}(\mathbf{r}, \omega) + \frac{n^2(\omega)\omega^2}{c^2} \tilde{\mathbf{E}}(\mathbf{r}, \omega) \right) e^{-i\omega t} d\omega = 0. \quad (1.19)$$

To obtain the Helmholtz equation:

$$\Delta \tilde{\mathbf{E}}(\mathbf{r}, \omega) + \frac{n^2(\omega)\omega^2}{c^2} \tilde{\mathbf{E}}(\mathbf{r}, \omega) = 0, \quad (1.20)$$

where Δ is the Laplace operator ($\Delta \equiv \nabla^2$).

The electric field is assumed to always stay polarized along the x direction, so scalar quantities can be used instead of vectors in the following calculations. Namely:

$$\mathbf{E}(\mathbf{r}, t) = \frac{1}{2} \left(E(\mathbf{r}, t) e^{-i\omega_0 t} + E^*(\mathbf{r}, t) e^{i\omega_0 t} \right) \hat{x}, \quad (1.21)$$

and the Helmholtz equation can be re-written in its scalar form:

$$\Delta \tilde{E}(\mathbf{r}, \omega) + \frac{n^2(\omega)\omega^2}{c^2} \tilde{E}(\mathbf{r}, \omega) = 0. \quad (1.22)$$

We consider the propagation of a pulse of light at angular frequency ω_0 in an optical fiber, along the z axis. One strategy is to describe the electric field as a product of two functions, in order to separate the variables:

$$E(\mathbf{r}, t) = DF(x, y)A(z, t). \quad (1.23)$$

In the frequency domain:

$$\tilde{E}(\mathbf{r}, \omega) = \tilde{D}F(x, y)\tilde{A}(z, \omega). \quad (1.24)$$

$F(x, y)$ is a dimensionless distribution function, it describes the intensity of the field in the cross-section of the fiber. This function is assumed to be frequency-independent because we only consider quasi-monochromatic pulses, which means that the spectral width $\Delta\omega$ verifies the condition $\Delta\omega/\omega_0 \ll 1$. As $\omega_0 \sim 10^{15}$, this condition is fulfilled for all the pulses in this work. For a 100 fs sech-squared pulse centered around 800 nm, $\Delta\omega/\omega_0 \approx 0.315\lambda/(c\Delta t) = 8.4 \times 10^{-3}$. The use of $F(x, y)$ is also justified by the fact that we assume a single-mode fiber (or more generally, a waveguide with a mode structure). The normalizing constants D and \tilde{D} are introduced so that $|E(\mathbf{r}, t)|^2$ matches the optical power.

$$\tilde{A}(z, \omega) = A_0(\omega)e^{i\beta(\omega)z}. \quad (1.25)$$

$\beta(\omega) = n(\omega)\omega/c$ is the propagation constant that characterizes the propagation of the light pulse in the fiber. It can be expanded in Taylor's series:

$$\beta(\omega) = \beta_0 + (\omega - \omega_0)\beta_1 + \frac{1}{2}(\omega - \omega_0)^2\beta_2 + \Delta\beta, \quad (1.26)$$

where:

$$\beta_0 = \beta(\omega_0), \quad (1.27)$$

$$\beta_1 = \left. \frac{\partial\beta}{\partial\omega} \right|_{\omega_0}, \quad (1.28)$$

$$\beta_2 = \left. \frac{\partial^2\beta}{\partial\omega^2} \right|_{\omega_0}, \quad (1.29)$$

$$(1.30)$$

and $\Delta\beta$ stands for the higher order terms. In order to understand what is the physical meaning of the Taylor coefficients, one can assume a Gaussian profile for $A_0(\omega)$ [34]:

$$A_0(\omega) = A_0 \exp\left(\frac{-(\omega - \omega_0)^2}{4\Gamma}\right), \quad (1.31)$$

where A_0 is the maximum value of the electric field.

By combining Eqs. 1.25, 1.26 and 1.31, the expression for the pulse becomes:

$$\tilde{A}(z, \omega) = \exp \left[-i\beta_0 z - i\beta_1 z(\omega - \omega_0) - \left(\frac{1}{4\Gamma} + \frac{i}{2}\beta_2 z \right) (\omega - \omega_0)^2 \right] \quad (1.32)$$

The higher-order terms can be neglected as a first approach, as the pulse is quasi-monochromatic. However in some cases this approximation does not hold anymore. This point will be discussed in the following sections.

The time evolution of the pulse can be derived from the inverse Fourier transform of Eq. 1.32:

$$A(z, t) = \frac{1}{2\pi} \int_{-\infty}^{+\infty} \tilde{A}(z, \omega) e^{i\omega t} d\omega \quad (1.33)$$

$$= \frac{1}{2\pi} \exp \left[i\omega_0 \left(t - \frac{\beta_0 z}{\omega_0} \right) \right] \int_{-\infty}^{+\infty} \exp [i(t - i\beta_1 z)(\omega - \omega_0)] \quad (1.34)$$

$$\cdot \exp \left[- \left(\frac{1}{4\Gamma} + \frac{i}{2}\beta_2 z \right) (\omega - \omega_0)^2 \right] d\omega$$

$$= \sqrt{\left(\frac{1}{\pi (1/\Gamma + 2i\beta_2 z)} \right)} \exp \left[i\omega_0 \left(t - \frac{\beta_0 z}{\omega_0} \right) \right] \exp \left[- \frac{1}{1/\Gamma + 2i\beta_2} (t - \beta_1 z)^2 \right]. \quad (1.35)$$

The first exponential is a phase term: it has no influence on the intensity of the pulse. $\beta_0 z$ represents the carrier-envelope phase, and corresponds to the phase between the fast oscillations of the carrier and the envelope of the pulse. This quantity evolves with time and space, and the phase-velocity can be defined from this as $v_\phi = \omega_0/\beta_0$. The second exponential shows that the pulse remains Gaussian when it propagates. However, there are two differences between this pulse and the original pulse. First, the pulse is delayed by $\beta_1 z$. The group velocity is defined from this as $v_g = \beta_1^{-1}$. Second, the new “width” of the Gaussian can be written $\Gamma(z)$ such as $1/\Gamma(z) = 1/\Gamma + 2i\beta_2$. From this complex quantity will arise a real part that leads to a change in the actual width of the pulse, and an imaginary part that is responsible for the *chirp* of the pulse. Indeed, β_2 is called the group velocity dispersion, and it describes the different velocities at which travel the several frequencies contained in the pulse. The frequencies of a pulse arrive at a different time at a given point if space, hence the analogy to the chirping of a bird that produces notes of ascending or descending pitch. This will become clear when a more detailed calculation is provided, in Section 1.2.3.

Let us now write the spatial Fourier transform of the electric field:

$$\tilde{E}(\mathbf{r}, \omega) = F(x, y) \int \mathcal{E}(\beta, \omega) e^{-i\beta z} d\beta \quad (1.36)$$

$$= F(x, y) e^{-i\beta_0 z} \int \mathcal{E}(\beta, \omega) e^{-i(\beta - \beta_0)z} d\beta \quad (1.37)$$

$$= \tilde{A}(z, \omega - \omega_0) F(x, y) e^{-i\beta_0 z}, \quad (1.38)$$

β is of the same order of magnitude as β_0 , so $|\beta - \beta_0| < \beta_0$. Then $e^{-i(\beta - \beta_0)z}$ describes a slowly oscillating wave with respect to the one described by $e^{-i\beta_0 z}$, and $\tilde{A}(z, \omega - \omega_0)$ is the slowly varying envelope of the electric field in the frequency domain.

$$\tilde{A}(z, \omega - \omega_0) = \int \mathcal{E}(\beta, \omega) e^{-i(\beta - \beta_0)z} d\beta, \quad (1.39)$$

By introducing Eq. 1.38 into the Helmholtz equation (Eq. 1.22):

$$\begin{aligned} & \left(\frac{\partial^2}{\partial x^2} + \frac{\partial^2}{\partial y^2} + \frac{\partial^2}{\partial z^2} \right) (\tilde{A}(z, \omega - \omega_0) F(x, y) e^{-i\beta_0 z}) \\ & + \frac{n^2(\omega)\omega^2}{c^2} (\tilde{A}(z, \omega - \omega_0) F(x, y) e^{-i\beta_0 z}) = 0. \end{aligned} \quad (1.40)$$

After taking the derivative with respect to z :

$$\begin{aligned} & \tilde{A}(z, \omega - \omega_0) \left[\left(\frac{\partial^2}{\partial x^2} + \frac{\partial^2}{\partial y^2} \right) F(x, y) \right] e^{-i\beta_0 z} \\ & + \frac{\partial^2 \tilde{A}(z, \omega - \omega_0)}{\partial z^2} F(x, y) e^{-i\beta_0 z} \\ & - 2i\beta_0 \frac{\partial \tilde{A}(z, \omega - \omega_0)}{\partial z} F(x, y) e^{-i\beta_0 z} \\ & - \beta_0^2 \tilde{A}(z, \omega - \omega_0) F(x, y) e^{-i\beta_0 z} \\ & + \frac{n^2(\omega)\omega^2}{c^2} \tilde{A}(z, \omega - \omega_0) F(x, y) e^{-i\beta_0 z} = 0. \end{aligned} \quad (1.41)$$

As \tilde{A} is a slowly varying envelope, we can use the slowly varying envelope approximation (SVEA). The SVEA is valid only if the pulse is long enough that the envelope of the pulse varies slowly in time and space compared to a period of its fast oscillations. More precisely, the variation of the slope of \tilde{A} is slow with respect to the slope itself on a distance equal to the wavelength, which means that the second derivative of \tilde{A} can be neglected. The use of the SVEA here is justified because the shorter pulses that are considered here have typical durations of 100 fs and wavelengths between 800 nm and 1 μm , which corresponds to a period of about 3 fs.

With the SVEA, the second member of Eq. 1.41 can be crossed out. Additionally, we introduce $\beta_0^2 = \beta_0^2 - \tilde{\beta}^2 + \tilde{\beta}^2$ in the fourth member of the equation. Upon factorization, the expression becomes:

$$e^{-i\beta_0 z} \left(\tilde{A}(z, \omega - \omega_0) \left[\left(\frac{\partial^2}{\partial x^2} + \frac{\partial^2}{\partial y^2} \right) F(x, y) + \left(\frac{n^2(\omega)\omega^2}{c^2} - \tilde{\beta}^2 \right) F(x, y) \right] + F(x, y) \left[-2i\beta_0 \frac{\partial \tilde{A}(z, \omega - \omega_0)}{\partial z} + (\tilde{\beta}^2 - \beta_0^2) \tilde{A}(z, \omega - \omega_0) \right] \right) = 0. \quad (1.42)$$

The following system is finally obtained:

$$\begin{cases} \left(\frac{\partial^2}{\partial x^2} + \frac{\partial^2}{\partial y^2} \right) F(x, y) + \left(\frac{n^2(\omega)\omega^2}{c^2} - \tilde{\beta}^2 \right) F(x, y) = 0 & (1.43a) \\ 2i\beta_0 \frac{\partial \tilde{A}(z, \omega - \omega_0)}{\partial z} + (\beta_0^2 - \tilde{\beta}^2) \tilde{A}(z, \omega - \omega_0) = 0 & (1.43b) \end{cases}$$

The first equation is an eigenvalue problem: it is possible to find the eigenvalues $\tilde{\beta}^2(\omega)$ corresponding to the eigenmodes $F(x, y)$. This is for example done for the fundamental mode of single-mode fibers of circular symmetry, the solution being a Bessel function, often approximated by a Gaussian function of the form $F(x, y) \approx \exp[-(x^2 + y^2)/w^2]$. In PCFs of higher-order symmetry (often 6), the fundamental mode differs a bit from a Bessel function. Then, the calculation of $\beta(\omega)$ often requires numerical simulations, or it can be measured using white-light interferometry [35]. In the following, we will only consider the case of single-mode fibers.

Nonlinear perturbation to the system

The nonlinearities can now be introduced in the second equation by adding a small perturbation to the system.

The first order perturbation theory applies in the case of an eigenfunction / eigenvalue problem such as:

$$H_0 \Psi = E \Psi, \quad (1.44)$$

where H_0 is an operator and E a number. Let us assume that, by solving this problem, we found an eigenfunction Ψ_0 corresponding to the eigenvalue E_0 . In other terms we have:

$$H_0 \Psi_0 = E_0 \Psi_0. \quad (1.45)$$

Next we consider that the operator H_0 undergoes a small perturbation and becomes $H_0 + \Delta H$. As the variation in the excitation of the system is small,

the characteristic response of the system is still described by the eigenfunction previously found Ψ_0 , and only the eigenvalues are slightly modified. Then:

$$(H_0 + \Delta H)\Psi_0 = E'_0\Psi_0, \quad (1.46)$$

where $E'_0 = E_0 + \Delta E$. An expression for ΔE is given by:

$$\Delta E = \langle \Psi_0 | \Delta H | \Psi_0 \rangle \quad (1.47)$$

$$= \frac{\iint dxdy |\Psi_0|^2 \Delta H}{\iint dxdy |\Psi_0|^2}, \quad (1.48)$$

which is the main result of the first order perturbation theory.

In the case of Eq. 1.43b, the operator is $H = \Delta_{xy} + \frac{n^2\omega^2}{c^2}$, the eigenfunction is $F(x, y)$ and the eigenvalue is $\tilde{\beta}^2$. The first order perturbation theory states that the small perturbation on $n(\omega)$ does not change the eigenfunction $F(x, y)$. However, the refractive index of the medium changes to:

$$n(\omega) \rightarrow n(\omega) + \Delta n, \quad (1.49)$$

where:

$$\Delta n = n_2|E|^2 + i\alpha/(2k_0), \quad (1.50)$$

n_2 being the nonlinear refractive index (in m^2/W) and α is the absorption coefficient. The relation of those two quantities with the third-order permittivity $\chi^{(3)}$ is explained in [Appendix A](#). Then the square of the refractive index changes by $\Delta(n^2) \approx 2n\Delta n$, and the variation of the operator can be written:

$$\Delta H = 2n\Delta n \frac{\omega^2}{c^2}. \quad (1.51)$$

The variation of the eigenvalue $\tilde{\beta}^2$ is derived from Eq. 1.48:

$$\Delta(\tilde{\beta}^2) = \frac{\iint dxdy |F(x, y)|^2 2n\Delta n k_0^2}{\iint dxdy |F(x, y)|^2}. \quad (1.52)$$

The variation of the eigenvalue is: $\Delta(\tilde{\beta}^2) \approx 2\tilde{\beta}\Delta\tilde{\beta}$. For sake of simplicity, we write $\Delta\tilde{\beta} = \Delta\beta$. Then:

$$\Delta\beta = \frac{\Delta(\tilde{\beta}^2)}{2\tilde{\beta}} \quad (1.53)$$

$$= \frac{nk_0^2 \iint \Delta n |F(x, y)|^2 dxdy}{\tilde{\beta} \iint |F(x, y)|^2 dxdy} \quad (1.54)$$

$$= \frac{k_0 \iint \Delta n |F(x, y)|^2 dxdy}{\iint |F(x, y)|^2 dxdy}, \quad (1.55)$$

because $\frac{\beta(\omega)}{n(\omega)} = \frac{\omega}{c} = k_0$. $\tilde{\beta}(\omega)$ then becomes $\tilde{\beta}'(\omega) = \tilde{\beta}(\omega) + \Delta\beta$. $\Delta\beta$ can easily be linked to previous parameters by writing:

$$\Delta\beta = \gamma|A(z, t)|^2 + i\frac{\alpha}{2}, \quad (1.56)$$

where γ is the nonlinear coefficient (in $\text{W}^{-1}\text{m}^{-1}$), defined as:

$$\gamma = \frac{n_2\omega_0}{cA_{\text{eff}}}. \quad (1.57)$$

A_{eff} is the effective area, commonly used in fiber optics:

$$A_{\text{eff}} = \frac{(\iint |F(x, y)|^2 dx dy)^2}{\iint |F(x, y)|^4 dx dy}. \quad (1.58)$$

When introducing Eq. 1.23 and 1.50 into Eq. 1.55:

$$\Delta\beta = D^2 k_0 n_2 \frac{\iint |F(x, y)|^4 dx dy}{\iint |F(x, y)|^2 dx dy} |A(z, t)|^2 + i\frac{\alpha}{2}. \quad (1.59)$$

From this we can see that the normalizing constant D verifies $1/D^2 = \iint |F(x, y)|^2 dx dy$.

Upon the approximation $\tilde{\beta}^2 - \beta_0^2 = (\tilde{\beta} + \beta_0)(\tilde{\beta} - \beta_0) \approx 2\beta_0(\tilde{\beta} - \beta_0)$, Eq. 1.43b becomes:

$$2ik\beta_0 \frac{\partial \tilde{A}(z, \omega - \omega_0)}{\partial z} = -2\beta_0(\tilde{\beta} - \beta_0) \tilde{A}(z, \omega - \omega_0). \quad (1.60)$$

$\tilde{\beta}$ is replaced by its Taylor expansion (Eq. 1.26):

$$\frac{\partial \tilde{A}(z, \omega - \omega_0)}{\partial z} = i \left[(\omega - \omega_0)\beta_1 + \frac{1}{2}(\omega - \omega_0)^2\beta_2 + \Delta\beta \right] \tilde{A}(z, \omega - \omega_0). \quad (1.61)$$

By definition:

$$A(z, t) = \int \tilde{A}(z, \omega - \omega_0) e^{-i(\omega - \omega_0)t} d\omega. \quad (1.62)$$

We first take the derivative of Eq. 1.62 with respect to z :

$$\frac{\partial A(z, t)}{\partial z} = \int \frac{\partial \tilde{A}(z, \omega - \omega_0)}{\partial z} e^{-i(\omega - \omega_0)t} d\omega. \quad (1.63)$$

With Eq. 1.61, the expression becomes:

$$\frac{\partial A(z, t)}{\partial z} = \int i \left[(\omega - \omega_0)\beta_1 + \frac{1}{2}(\omega - \omega_0)^2\beta_2 + \Delta\beta \right] \tilde{A}(z, \omega - \omega_0) e^{-i(\omega - \omega_0)t} d\omega. \quad (1.64)$$

If we separate the terms:

$$\begin{aligned} \frac{\partial A(z, t)}{\partial z} &= \int i(\omega - \omega_0)\beta_1 \tilde{A}(z, \omega - \omega_0) e^{-i(\omega - \omega_0)t} d\omega \\ &+ \int i\frac{1}{2}(\omega - \omega_0)^2 \beta_2 \tilde{A}(z, \omega - \omega_0) e^{-i(\omega - \omega_0)t} d\omega \\ &+ \int i\Delta\beta \tilde{A}(z, \omega - \omega_0) e^{-i(\omega - \omega_0)t} d\omega. \end{aligned} \quad (1.65)$$

Now Eq. 1.62 is derived with respect to t :

$$\frac{\partial A(z, t)}{\partial t} = - \int i(\omega - \omega_0) \tilde{A}(z, \omega - \omega_0) e^{-i(\omega - \omega_0)t} d\omega \quad (1.66)$$

and

$$\frac{\partial^2 A(z, t)}{\partial t^2} = - \int (\omega - \omega_0)^2 \tilde{A}(z, \omega - \omega_0) e^{-i(\omega - \omega_0)t} d\omega \quad (1.67)$$

By comparing Eq. 1.65 to Eqs. 1.66 and 1.67, the following equation appears:

$$\frac{\partial A(z, t)}{\partial z} = -\beta_1 \frac{\partial A(z, t)}{\partial t} - \frac{i}{2}\beta_2 \frac{\partial^2 A(z, t)}{\partial t^2} + i\Delta\beta A(z, t). \quad (1.68)$$

The term proportional to β_1 is canceled when transforming to a reference frame moving with the pulse at the group velocity, by applying the change of variable $t \rightarrow t - \beta_1 z$.

In the following, for the sake of clarity, the slowly varying envelope of the electric field in the time domain will be noted $E(z, t)$. If the absorption is neglected, the usual form of the NLSE is recovered:

$$\frac{\partial E(z, t)}{\partial z} = -\frac{i}{2}\beta_2 \frac{\partial^2 E(z, t)}{\partial t^2} + i\gamma |E(z, t)|^2 E(z, t). \quad (1.69)$$

1.2.2 Fourier-transform-limited pulses

The temporal profile and the spectrum of a pulse of light are related to each other by Fourier transformation. Therefore, there is a direct relationship between the pulse duration of an unchirped pulse and its spectrum, namely, the broader the spectrum is, the smaller the pulse duration will be. If the pulse propagates through a dispersive medium, the pulse duration can be larger than the one given by the Fourier transformation of the spectrum, by it can never be shorter. When a pulse has the shortest duration allowed by its bandwidth, it is called a Fourier-transform-limited pulse. The pulse duration and bandwidth are then linked by the time-bandwidth product, namely $\Delta t \Delta f = C$, where C is a constant that depends on the shape of the pulse. For example, for Gaussian pulses, $C = 2 \ln 2 / \pi \approx 0.441$, while for sech-squared pulses

$C = 4 (\ln(1 + \sqrt{2}))^2 / \pi^2 \approx 0.315$, where the duration and bandwidth are defined as the full-width at half maximum. Those factors are derived from the properties of the Fourier transform, the detailed calculation is shown in [Appendix B](#) for more details.

1.2.3 Separate effects of dispersion and nonlinearities

The NLSE shows that group-velocity dispersion (GVD, β_2) and nonlinearities (γ) are two phenomena playing a major role in the propagation of a pulse of light in a fiber. Let us detail what are the effects of each of them on the pulse propagation, independently from each other.

Group-velocity dispersion

The effects of GVD are exemplified here for Gaussian pulse because it is possible to analytically Fourier transform a Gaussian. The analytical results are therefore only applicable to Gaussian pulses, but the qualitative conclusions are valid for any pulse shape.

γ is set to zero in the NLSE to study the effect of GVD alone.

$$\frac{\partial E(z, t)}{\partial z} = -\frac{i}{2}\beta_2 \frac{\partial^2 E(z, t)}{\partial t^2}. \quad (1.70)$$

This equation can be resolved in the Fourier domain: the Fourier transform of $E(z, t)$ is $\tilde{E}(z, \omega)$ and verifies:

$$\frac{\partial \tilde{E}(z, \omega)}{\partial z} = \frac{i}{2}\beta_2 \omega^2 \tilde{E}(z, \omega). \quad (1.71)$$

The solution is an exponential:

$$\tilde{E}(z, \omega) = \tilde{E}(0, \omega) e^{\frac{i}{2}\beta_2 \omega^2 z}. \quad (1.72)$$

We consider a Gaussian pulse:

$$E(0, t) = E_0 \exp\left(\frac{-t^2}{2\tau^2}\right). \quad (1.73)$$

It is Fourier transformed to obtain $\tilde{E}(0, \omega)$, that is then introduced in Eq. 1.72. The inverse Fourier transform can then be calculated:

$$E(z, t) = E_0 \frac{\tau}{(\tau^2 - i\beta_2 z)^{1/2}} \exp\left(-\frac{t^2}{2(\tau^2 - i\beta_2 z)}\right) \quad (1.74)$$

This can be re-written in the form:

$$E(z, t) = E_1(z) \exp\left(-\frac{t^2}{T_{\text{eff}}(z)^2}\right) \exp(-i\phi_D(z, t)), \quad (1.75)$$

where:

$$E_1(z) = \frac{E_0\tau}{(\tau^4 + \beta_2^2 z^2)^{1/2}}, \quad (1.76)$$

$$T_{\text{eff}}(z) = \left(\frac{\tau^4 + \beta_2^2 z^2}{\tau^2}\right)^{1/2} = \tau \left(1 + \frac{\beta_2^2}{\tau^4} z^2\right)^{1/2} \quad (1.77)$$

and

$$\phi_D(z, t) = \frac{-t^2\beta_2 z}{\tau^4 + \beta_2^2 z^2} + \frac{1}{2} \tan^{-1}\left(\frac{\beta_2 z}{\tau^2}\right). \quad (1.78)$$

It is useful to introduce the dispersion length $L_D = \tau^2/|\beta_2|$, and then

$$T_{\text{eff}}(z) = \left(\frac{\tau^4 + \beta_2^2 z^2}{\tau^2}\right)^{1/2} = \tau [1 + (z/L_D)^2]^{1/2}. \quad (1.79)$$

The pulse remains Gaussian but its duration T_{eff} increases during the propagation along z .

The instantaneous frequency variation (or chirp) is the time derivative of the temporal phase $\phi_D(z, t)$:

$$\delta\omega(z, t) = \frac{2\beta_2 z}{\tau^4 + \beta_2^2 z^2} t. \quad (1.80)$$

This equation shows a linear time dependence: this means that GVD induces a linear chirp on the pulse as it propagates. If β_2 is positive (normal dispersion), at $t < 0$ (the leading part of the pulse), $\delta\omega < 0$, and for $t > 0$ (trailing part of the pulse), $\delta\omega > 0$. In other words, the red travels faster than the blue (like in the majority of the classical materials). On the contrary, if β_2 is negative (anomalous dispersion), the blue travels faster than the red. $T_{\text{eff}}(z)$ depends on β_2^2 , so in both cases, an initially Fourier-transform-limited pulse broadens during the propagation.

In the case of photonic crystal fibers, the GVD can be positive or negative depending on the wavelength. There can be one or several wavelengths for which the GVD is zero, they are called the zero-dispersion wavelengths (ZDW). The dispersion curves for two different PCFs are shown in Fig. 1.4 as an example. Those fibers feature one anomalous dispersion range, two normal dispersion ranges and two ZDW.

The spectrum can be calculated from Eq. 1.72 and 1.73:

$$S(\omega) = |\tilde{E}(z, \omega)|^2 = E_0\pi\tau^2 e^{-\omega^2\tau^2/2}. \quad (1.81)$$

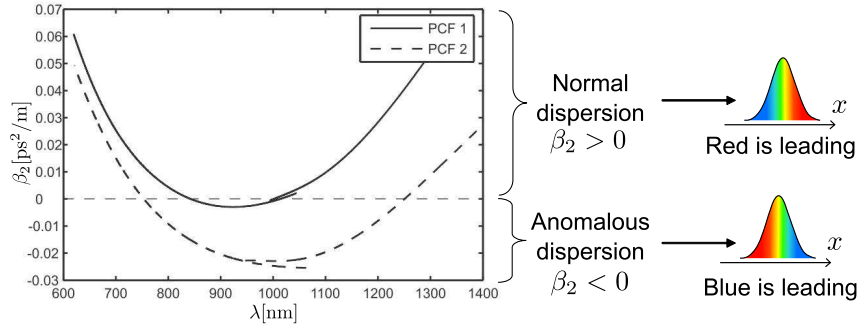


Figure 1.4: Example of group-velocity dispersion for two solid-core PCFs and interpretation for the propagation of the frequencies in the pulse. Graph: Courtesy of Esben R. Andresen.

The spectrum is not z -dependent, it stays identical throughout the propagation. The only effect of GVD is the temporal broadening occurring because the frequencies present in the pulse travel at different velocities in the fiber. Similarly, the higher-order dispersion terms do not affect the spectrum. This is easily seen from the fact that the dispersion amounts to multiplication of $e^{i\phi(\omega)}$ onto $\tilde{E}(\omega)$. The exponential cancels out upon taking the squared norm $|\tilde{E}(\omega)|^2$ to arrive at the spectrum. Figure 1.5(a) sums up the features of GVD that were just described.

Self-phase modulation

The nonlinearities in the fiber cause a change of refractive index in the medium that is proportional to $|E|^2$. This is called the optical Kerr effect, because of its similarities to the Kerr electro-optic effect, where an electric field is applied to a medium and changes its refractive index in a quadratic way. Indeed, as already discussed in Section 1.2.1, the nonlinear coefficient can be written $\gamma = \frac{n_2\omega_0}{cA_{\text{eff}}}$, where n_2 is the nonlinear refractive index such as $\Delta n = n_2|E|^2$.

β_2 is set to zero in the NLSE to study the effect of nonlinearities alone.

$$\frac{\partial E(z, t)}{\partial z} = i\gamma|E(z, t)|^2 E(z, t). \quad (1.82)$$

This equation can be solved in the time domain:

$$E(z, t) = E(0, t)e^{i\gamma|E(0, t)|^2 z}, \quad (1.83)$$

with $E(0, t) = E_0 e^{-t^2/(2\tau^2)}$. The temporal phase $\phi_{\text{NL}}(t) = \gamma|E(0, t)|^2 z$ that is imposed on the pulse is intensity dependent: it is maximum at $t = 0$ and

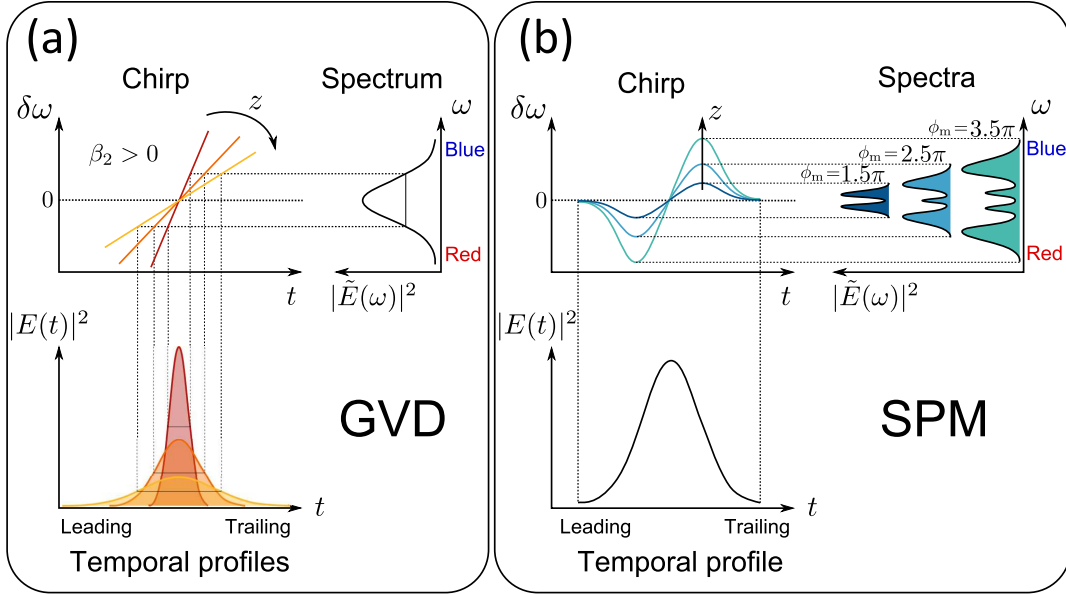


Figure 1.5: Separate effects of (a) GVD and (b) SPM on an unchirped Gaussian pulse propagating in a fiber along direction z . (a) The spectrum stays unchanged, but the pulse temporally broadens when it propagates. The GVD-induced chirp is linear. The scheme was drawn for $\beta_2 > 0$, so the chirp is positive and the red wavelengths go faster than the blue ones. If $\beta_2 < 0$, the pulse broadens in the same way, but the chirp is negative and the blue goes faster than the red. (b) The temporal profile stays unchanged, but SPM generates new frequencies, and the spectrum broadens. The chirp has the shape of the derivative of a Gaussian and its amplitude increases when the pulse propagates. Because of this shape, one frequency can be traveling with two different phases, which can cause constructive or destructive interference, hence the oscillating pattern of the spectrum. The three examples of spectra drawn on the scheme correspond to three values of the maximum nonlinear phase (1.5π , 2.5π and 3.5π). As the spectrum broadens, the Fourier-transform-limited duration of the pulse decreases, but the actual duration of the pulse stays unchanged because of the chirp.

its shape follows the Gaussian profile of the pulse in the time-domain. The nonlinear length L_{NL} can be defined such as $\phi_{\text{NL}}(t) = z/L_{\text{NL}}$, with $L_{\text{NL}} = 1/(\gamma P_0)$. As before, the instantaneous frequency is the derivative of the phase:

$$\delta\omega(z, t) = \frac{2\gamma P_0 z}{\tau^2} t e^{-t^2/\tau^2}. \quad (1.84)$$

This effect is called self-phase modulation (SPM). The change of refractive index induced by the intense optical electric field perturbs the propagation of the pulse. In silica fibers, $n_2 > 0$ so $\delta\omega < 0$ for $t < 0$ at the leading edge and $\delta\omega > 0$ for $t > 0$ at the trailing edge. As in the case of GVD for normal dispersion, the red part of the spectrum goes overall faster than the blue part. However, the dependence is far from being linear as it has the shape of the derivative of a Gaussian.

The spectrum can be estimated from:

$$S(\omega) = \left| \int_{-\infty}^{+\infty} E_0 e^{-t^2/(2\tau^2)} e^{i\gamma|E(0,t)|^2 z} e^{i\omega t} dt \right|^2 \quad (1.85)$$

Simulations can show that this results in spectrum broadening. In other words, new frequencies are continuously created during the propagation of the pulse. The resulting spectrum for unchirped Gaussian pulse experiencing SPM consists of several peaks that appear because each frequency can be generated with two different phases, causing interferences. A first estimation of the broadening can be made from Eq. 1.84. As suggested in Fig. 1.5(b), the spectral width can roughly be estimated by $\delta\omega_{\max}$ in the chirp graph. By calculating the time derivative of Eq. 1.84 and setting it to zero,

$$\delta\omega_{\max} = \sqrt{2} e^{-1/2} \frac{\gamma P_0 z}{T_0}. \quad (1.86)$$

One can notice that $|E(z, t)|^2 = |E(0, t)|^2$ is not z -dependent, therefore the pulse does not get broader or narrower when it propagates. However, as the spectrum broadens, the Fourier-transform-limited duration of the pulse decreases, and one would recover the shorter pulse by compensating for the chirp induced by SPM.

The analytical results above apply only to Gaussian pulses. However, the qualitative conclusions stand for any pulse shape. Any temporal pulse shape will remain unchanged under the action of SPM alone. Indeed, the SPM amounts to multiplication of $e^{i\gamma t}$ onto $E(z, t)$, and this factor disappears upon taking the squared norm of $E(z, t)$. Figure 1.5(b) sums up the features of SPM that were described above.

If the input pulse is initially chirped, the resulting spectrum can be drastically changed. In particular, under some conditions, a negatively chirped pulse experiencing SPM in a fiber can result in spectral compression [36].

1.2.4 Combined effects of GVD and SPM

In many cases, both GVD and SPM are acting on the pulse and one cannot separate their effects. The interplay between those two effects can result in

interesting features. To estimate the relative importance of GVD and SPM, the parameter N is introduced:

$$N^2 = \frac{L_D}{L_{NL}} = \frac{\gamma P_0 T_0^2}{|\beta_2|}. \quad (1.87)$$

If $N \gg 1$, the dispersion length is much longer than the nonlinear length, so SPM dominates. On the contrary, if $N \ll 1$, GVD dominates.

If $N = 1$ and $\beta_2 > 0$, some temporal broadening appears, and the spectral broadening is reduced compared to the SPM-only case. This can be qualitatively understood by looking at Fig.1.5: SPM generate new red frequencies at the leading edge, and new blue frequencies created at the trailing edge. Because of the positive dispersion, the already leading red components travel faster than the already delayed blue components, which results in an extra temporal broadening. On the other hand, the chirp created by GVD lowers the amplitude of the one created by SPM, therefore, the resulting maximum nonlinear phase is reduced and the spectrum broadening is slowed down.

If $N = 1$ and $\beta_2 < 0$, the opposite situation occurs. The red components created at the leading edge are going slower than the blue components created at the trailing edge, which acts against the temporal broadening of the pulse. Furthermore, the negative chirp induced by GVD acts against the spectral broadening caused by SPM. In this case, the combined effects of GVD and SPM create what will further on be called a soliton, which is a chirp-free pulse propagating in the fiber without changing its shape.

1.3 Soliton dynamics

1.3.1 Soliton formation

Let us go back to the resolution of the NLSE (Eq. 1.69), to which an analytical solution can be found in the case of anomalous dispersion ($\beta_2 < 0$). It can be expressed as follows [33]:

$$E(z, t) = \sqrt{P_0} \cdot \operatorname{sech} \left(\frac{t}{T_0} \right) \cdot \exp \left(\frac{i|\beta_2|z}{T_0^2} \right), \quad (1.88)$$

where P_0 is the peak power of the pulse and T_0 is its duration, defined with respect to the full width at half maximum duration by $T_{\text{FWHM}} = 2 \ln(1 + \sqrt{2})T_0$. This solution is independent of the propagated distance z apart from an oscillating phase. This means that the envelope remains unchanged no matter the propagation distance. This describes a fundamental soliton. As suggested before, soliton dynamics relies on the interplay between the two processes involved in the NLSE: the anomalous GVD (β_2) and the SPM created by the nonlinear

Kerr effect (γ) act against each other in a balanced way, which ensures the preservation of the pulse shape. For fundamentals solitons, $N = 1$ and

$$\frac{\gamma P_0 T_0^2}{|\beta_2|} = 1. \quad (1.89)$$

There are also solutions for N equal to integers ≥ 2 , corresponding to higher order solitons. In these cases, the temporal and spectral profiles evolve in a periodic fashion. The spatial period of this “breathing” is equal to $z_0 = \pi/2L_D$. For example, the temporal profile of a third-order soliton successively narrows, broadens, splits in two parts, reshape itself into a unique peak, narrows again and finally broadens back to its original shape. Over the same spatial period, the spectrum also follows a cycle of narrowing, broadening, and change of shape to finally come back to its original state. This can be partially understood by thinking again of the counteracting effects of GVD and SPM. At the beginning, as $L_D/L_{NL} > 1$, the SPM dominates and it broadens the spectrum. The negative GVD temporally compresses the central part of the pulse that is positively chirped by the SPM, resulting in an intensity increase that affects back the SPM (proportional to $|E|^2$). The subsequent periodical evolution due to the mutual interactions of GVD and SPM has been theoretically calculated [37] and experimentally observed [38].

In practice, most of the time the input peak power P_0 and width T_0 do not exactly match the fiber parameters so that N is an integer. Soliton perturbation theory shows that such a pulse adapts its shape and width and evolves into a soliton [39]. An input pulse whose N value is in the range $\tilde{N} - 0.5 < N < \tilde{N} + 0.5$ (\tilde{N} being an integer) will asymptotically evolve to a \tilde{N} -order soliton. This is also the case if the shape of the input pulse does not match the one of the soliton. For example if the input pulse is Gaussian, the pulse will evolve into a sech-square shaped one. Similarly, if the input pulse is negatively chirped, or mildly positively chirped, it can evolve into an unchirped soliton. However if the chirp is too large, the effect of the negative GVD is canceled and the balance between GVD and SPM leading to soliton formation cannot occur. From this, it is clear that the exact match between the input pulse and the fundamental soliton is not required to launch a soliton, and the parameters of the input pulse can widely vary and still evolve into a soliton-like pulse. However, this evolution comes with a major drawback: part of the initial energy is lost under the form of dissipative waves. To avoid this power loss, it is preferable that the input pulse parameters are the closest possible to the soliton parameters.

1.3.2 Soliton self-frequency shift

For long enough pulses (> 5 ps), the expression of $\beta(\omega)$ (see Eq. 1.26) can be truncated at second order. Indeed, for such long pulses, the peak power is

usually not strong enough to generate significant higher-order effects.

However, for short pulses (< 5 ps), the simplest form of the NLSE (Eq. 1.69) is not sufficient to fully describe the behavior of solitons. In particular, the delayed vibrational Raman response of the medium was previously neglected, and turns out to play an important role in soliton dynamics. The full NLSE can be re-written, taking into account the higher-order effects [33]:

$$\frac{\partial E}{\partial z} + \frac{i}{2}\beta_2 \frac{\partial^2 E}{\partial t^2} - i\gamma|E|^2 E = \sum_{p=2}^{\infty} -\frac{(i)^{p-1}}{p!} \beta_i \frac{\partial^p E}{\partial t^p} - \frac{\gamma}{\omega_0} \frac{\partial}{\partial t} (|E|^2 E) - i\gamma T_R E \frac{\partial |E|^2}{\partial t}. \quad (1.90)$$

On the left-hand side are the three terms already present in the classical NLSE, while on the right-hand side are the terms accounting for higher-order dispersion, self-steepening and intrapulse Raman scattering.

Higher-order dispersion, and in particular third-order dispersion β_3 has to be taken into account if the pulse is very short (< 30 fs), when operating at wavelengths close to the zero-dispersion wavelength (ZDW), i.e. for $\beta_2 \approx 0$, or in specific processes such as supercontinuum generation. However, for 100-fs long fundamental solitons propagating at wavelengths far from the ZDW, it has only little influence and can be treated perturbatively.

Self-steepening is a phenomenon that stems from the dependence of the group velocity on the intensity. More precisely, the peak of the pulse has a higher intensity and therefore goes slower than the wings of the peak that have lower intensity. Without GVD, this effect leads to asymmetrical spectra and temporal profiles. If the pulse propagates long enough, an optical shock can even be created. This effect was found to be negligible in the pulses generated in this work.

Conversely, intrapulse Raman scattering is the most important higher-order effect that affects solitons. The parameter T_R is related to the full Raman response function of the medium $R(t)$, that takes into account the electronic (instantaneous) and vibrational (delayed) Raman response:

$$T_R = \int_{-\infty}^{\infty} tR(t)dt. \quad (1.91)$$

Intrapulse Raman scattering originates from the delayed Raman response of the medium. When the pulse is very short (typically ≈ 100 fs), its spectrum is broad enough that an effect similar to stimulated Raman scattering can occur between the blue and the red components, mediated by the vibration modes of silica. Namely, the red part of the spectrum experiences a Raman gain, while the blue part experiences a Raman loss. One can also understand this effect as an energy transfer between the blue and the red part of the spectrum. As a result, the soliton continuously redshifts along its propagation in the fiber, this

phenomenon is called soliton self-frequency shift (SSFS) [40, 41]. By setting all higher-order parameters to zero in Eq. 1.90 and applying the variational method that makes use of the Lagrangian formalism [42], it is possible to estimate the variation of the central frequency of the soliton:

$$\Delta\omega_R \propto -\frac{|\beta_2|z}{T_0^4}. \quad (1.92)$$

The redshift increases proportionally with the distance traveled in the fiber: the longer the fiber, the higher the final redshift at the output. Another consequence of Eq. 1.92 can be brought out by recalling that when more power is injected into the fiber, the duration of the pulse decreases (see Eq. 1.89). The redshift is proportional to T_0^{-4} , so the any small decrease of the duration of the pulse translates to an enhanced redshift. This way, the wavelength of the soliton can be tuned by changing the input power, while the duration of the pulse remains almost constant.

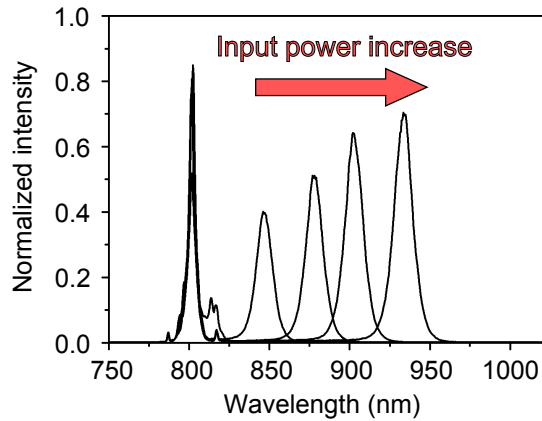


Figure 1.6: Example of increasing soliton redshift with increasing input power. The peak at 800 nm is the residue from the pump laser.

It is important to note that femtosecond higher-order solitons are not stable because of the combined effects of higher-order dispersion, self-steepening and intrapulse Raman scattering, which leads to the breakup of these pulses into their constituents. This is called the soliton decay. When the input power becomes high enough to support a soliton with $N \gg 1$, the spectrum splits into several bands, including one or several red-shifted fundamental solitons and blue-shifted nonsolitonic radiation [43]. For this reason, the solitons that are going to be discussed in the following are all fundamental solitons.

1.3.3 Soliton delay

Due to the SSFS previously described, each soliton follows a trajectory in the wavelength vs. z plane that depends on its peak power P_0 . Until then, the β_1 term in the NLSE was not taken into account because the pulse was always described in a coordinate frame that travels at the group velocity $v_g = \beta^{-1}$, so that the zero of the time axis is always at the center of the soliton. However, it is interesting to notice that two solitons of different P_0 will experience a different $\beta_1(z)$, and there will be a delay between those two solitons at the output of the fiber. Knowing the $\beta_1(\lambda)$ of the fiber and the $\lambda(z)$ of the soliton, it is possible to estimate the delay between the two solitons. This issue will be addressed in more details in Section 3.2.

1.4 Conclusion

Solitons propagating in a fiber possess remarkable features that were detailed in this Chapter. Their three main properties, useful for applications in nonlinear microscopy and spectroscopy, are the following. First, solitons remain close to being Fourier-transform-limited throughout their propagation, which means that femtosecond pulses can be generated and delivered to a sample by the same fiber. Second, their wavelength can be shifted by changing the input power, through the modification of the soliton self-frequency shift. This can be used for generating new frequencies, or get hyperspectral data. Finally, this change of wavelength is associated with a delay shift, that can be useful in time resolved measurements.

2 Chapter 2: Fiber delivery for TPEF and SHG microscopy

Since the first realization in 1990 [44], the development of nonlinear microscopy techniques has led to a powerful set of methods able to provide images of biological samples carrying functional, quantitative and dynamic information [45–47]. Although linear fluorescence microscopy remains one of the most widely used ways of studying biological samples, nonlinear multiphoton microscopy has been used to overcome some of the drawbacks associated with linear techniques.

However, the implementation of nonlinear microscopy techniques often relies on bulky optics, and are therefore not always suited for *in vivo* experiments, especially in the field of medical imaging. A way to circumvent this problem is to use endoscopy techniques, where the light is sent and collected through a tube or an optical fiber. Endoscopes have been used in association with white light imaging techniques for decades. Since the first fiber-based endoscope was invented in 1958 [48], years of development and improvement has resulted in the establishment of endoscopes as widely used tools in the field of medical diagnosis.

The implementation of the new contrasts brought by nonlinear processes in an endoscope-like configuration that allows *in vivo* imaging is of great interest for medical applications. Unfortunately, the generation and observation of nonlinear signals is not compatible with the propagation in the fibers classically used in endoscopy, because of the deleterious effects of the propagation medium that arise when the intensity of light is high, which is necessary for nonlinear microscopy.

First, the properties and requirements of nonlinear microscopy techniques will be briefly summarized, then the way previous studies tackled the problems of fiber delivery for nonlinear microscopy and endoscopy will be presented, finally the new approach that was developed during this work and the obtained results will be detailed.

2.1 Properties of nonlinear microscopy

Nonlinear optical microscopy uses nonlinear light-matter interaction to generate contrast and produce images. The nonlinear processes involve the simultaneous excitation of a molecule by several photons, which is why nonlinear microscopy is also called multiphoton microscopy. Conversely, conventional mi-

croscopy uses linear interactions, for instance, absorption, scattering, refraction and one-photon fluorescence. The energy diagrams of some of the processes used in nonlinear microscopy are presented in Fig. 2.1, along with the energy diagram for one-photon fluorescence, for comparison. In two-photon excited fluorescence (TPEF), the light emission occurs after the vibrational relaxation of the molecule, whereas for second-harmonic generation (SHG) and third-harmonic generation (THG), the excitation and de-excitation are simultaneous. Nonlinear microscopy has several advantages over linear microscopy [49].

As previously mentioned, nonlinear processes rely on the simultaneous excitation of a molecule by several photons. As this is less probable than the excitation of the molecule by a single photon, this implies a high excitation intensity. In practice, when working with unamplified lasers, nonlinear signals will only be observable if the light is tightly focused by a microscope objective; then the processes are efficiently triggered only at the focus of the objective, where the intensity is the highest. This results in an intrinsic optical sectioning that improves the resolution along the optical axis (the z axis), allowing 3D-imaging without the need of a confocal setup. Moreover, the high intensity requirement obliges the use of pulsed laser light for excitation. The use of pulsed light excitation reduces the photodamage, because the time of light exposure is reduced.

Furthermore, the energy of several photons are transferred to the molecule, and this energy is released by the molecule in the form of a single photon of higher energy. Consequently, the excitation occurs at higher wavelengths than the emission. Typically, the excitation lies in the near-infrared (NIR) range, between 800 and 1 μm . This is beneficial for at least two reasons: (i) it is a good compromise between penetration depth that is better at higher wavelengths, and optical resolution that is better at shorter wavelengths due to the diffraction limit; and (ii) this range is ideally located between the high linear absorption of hemoglobin and melanin in the visible, and the high linear absorption of water, in the infrared. This feature, combined with the optical sectioning, reduces the out-of-focus photobleaching: both the linear and the nonlinear absorption of the out-of-focus regions are low. Another reason for the chosen wavelength to be lower than 1 μm is the availability of good quality optics that is better in the visible and NIR ranges.

Finally, endogenous nonlinear processes can abound in biological specimens, which allows to obtain images without the need of staining. For instance, collagen fibers produces a strong SHG signal. Techniques relying on coherent Raman scattering are powerful label-free nonlinear methods, they will be discussed in Chapter 4.

As suggested before, the implementation of nonlinear techniques in an endoscopic modality is problematic because of the high required intensities. The propagation of short pulses with high peak powers is often perturbed by disper-

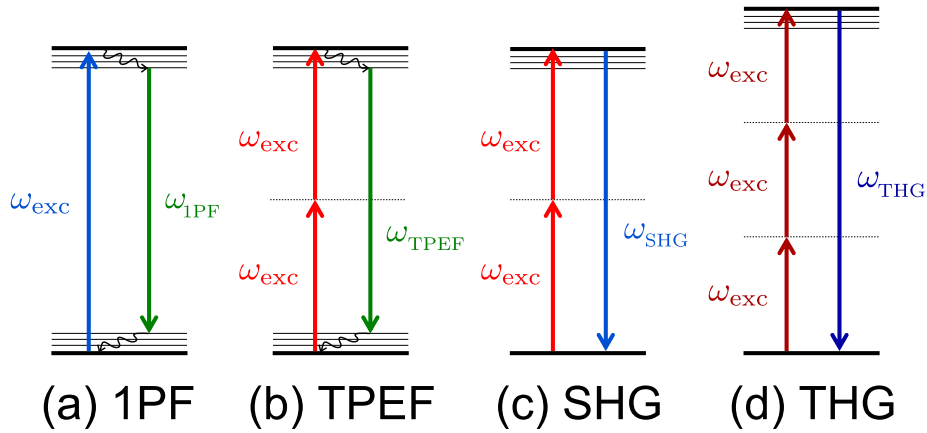


Figure 2.1: Energy diagram of (a) One photon fluorescence (1PF), and of three nonlinear effects among the most commonly used in nonlinear microscopy. (b) Two-photon excited fluorescence (TPEF); (c) Second-harmonic generation (SHG); (d) Third-harmonic generation (THG)

sion and nonlinear effects in the fiber itself. A critical point is then the delivery of a short pulse (typically 100 fs long) to a sample through a fiber.

2.2 Fiber delivery for multiphoton microscopy

The key parameter in nonlinear optics is the peak power of the excitation pulse in the focal volume. Nonlinear processes start to generate observable signals when the applied electric field reaches values non negligible compared to the interatomic electric field (typically, 10^{10} V/m). For example, let us consider an applied electric field of 10^8 V/m. This value corresponds to an instantaneous optical power of about 1 kW, for a beam at visible frequencies focused near its diffraction limit. Then, the corresponding average power for a pulsed laser with 1-ps pulses at 80 MHz is about 80 mW (pulse energy 1 nJ), and it is about 8 mW for 100-fs pulses at 80 MHz (pulse energy 100 pJ). This rough estimation emphasizes the advantage of short pulses in nonlinear microscopy: they allow to increase the peak power without increasing the average power and the total amount of energy sent to the sample, which is beneficial from the photodamage point of view.

The need of ultra-short pulses in nonlinear microscopy imposes the use of single-mode fibers in order to avoid the effects of mode dispersion present in multimode fibers (see Section 1.1.1).

The typical values of group-velocity dispersion (GVD) and nonlinearity (SPM) for classical step-index single-mode fibers strongly perturb the propagation of short pulses. GVD and SPM temporally and spectrally modifies the pulse; at

the output of the fiber, it is often temporally broadened, chirped and distorted. Atherton and Reed circumvented this problem by applying a strong negative frequency chirp to the 100-fs pulse before the propagation in the fiber [50]. This way, the duration of the pulse was increased to several ps to reduce the peak power and limit the effects of SPM. The positive GVD in the fiber nearly restored the pulse duration at the output of the fiber. Clark and co-workers presented a different pre-compensation scheme [51]. The pulse was first spectrally broadened through SPM in a SMF, then temporally compressed and negatively chirped by a series of prisms. Finally, it is spectrally compressed in a second SMF, also used for delivery. The SPM of the second fiber counteracted the effects of the SPM of the first fiber because of the negative GVD in between, which was also set to compensate for the positive GVD of both fibers.

The excitation and collection of the signals through the same fiber proved difficult with standard fibers because of the small overlap of the fundamental mode with the back-scattered signal. This point was improved with the introduction of double-clad fibers. Several groups designed two-photon fluorescence endoscopes based on negatively pre-chirped pulses sent to the sample via double-clad SMFs [52–54]. The scanning was done with piezoelectric actuators and the signal was collected in the epi direction and transmitted to the detectors through the outer multi-mode clad of the fiber.

The interesting new features of PCFs (see Section 1.1.2) were also put to use for fiber delivery and multiphoton endoscopy in a double-clad geometry. Double-clad solid-core PCFs transmitted negatively pre-chirped pulses in their core for excitation and collected the signal by confining it in a second cladding made of silica, by the means of an outer ring of air holes. Microelectromechanical system (MEMS) mirrors were used for the scanning [55–57].

The common point of those techniques is that the pulse propagates in silica. Pre-compensating systems have been developed to counteract the dispersion of the medium, by the means of grating pairs, prisms, or other pieces of fiber. This way, a negatively chirped pulse is brought back to its Fourier-transform-limited shape after traveling through the positive GVD medium. However, pre-compensation comes with a number of difficulties [58, 59]. First, it only compensates for group-velocity dispersion, without considering the higher-order dispersion or the nonlinearities, which may be a problem in some cases. Second, any pre-compensation system only gives a transform-limited output pulse within a narrow input parameter range. It is then difficult to adapt it for tunable pulses for example, as the pre-compensation parameters will be different at other wavelengths.

Hollow-core photonic bandgap fibers [60–63] are a possible solution to this problem. In this case, the light propagates in air rather than in silica, so it experiences a very low nonlinearity. Similarly, large mode area fibers [64] were designed to minimize the effect of nonlinearities by allowing the pulse to

propagate over a larger area, so with a lower power density. However, the tunability provided by soliton redshift cannot be achieved in this kind of fibers. Tunable solitons have been observed in hollow-core and large mode area fibers [65, 66], but the input power requirements are too high for standard femtosecond light sources available in many biology labs (see e.g. Ref. [67]). Indeed, Ti:sapphire lasers commonly used for multiphoton microscopy are universally high-repetition-rate (between 50 and 100 MHz) to facilitate high-speed image acquisition [68]. This means that their pulse energy stays below about 50 nJ, too low for the solitons in hollow-core fibers, that require input pulse energies of several hundreds of nJ.

Recently, Er and Yb doped fiber lasers have been put to use in a new type of all-fiber-optic endoscopes [69, 70]. These are very promising technologies that allow the development of very compact systems. However, the maximum gain of erbium is located at 1.55 μm and the maximum gain of ytterbium at 1.03 μm , while a lot of applications in imaging of biological samples use wavelengths between 800 nm and 1 μm , for the reasons detailed in Section 2.1.

2.3 A solid-core photonic bandgap fiber for high energy solitons

As explained in section 1.3, solitons are intrinsically Fourier-transform-limited at the output of the fiber. This is a convenient way of obtaining ultra-short pulses at the tip of a fiber without the need of any pre-compensation system, because the properties of the fiber themselves adjust the incoming pulse to shape it into a Fourier-transform-limited soliton. Moreover, they possess features that are useful in several schemes for nonlinear microscopy and spectroscopy: upon variation of the input power, they are tunable over a wide range (typically 100 nm or more), and their delay can be adjusted over a few ps.

However, these features come with a number of drawbacks, including the fixed power for a soliton at a given wavelength in a given fiber. Indeed, if more power is coupled into the fiber, it will only result in further redshift through SSFS. Equation 1.89 indicates that the power of the soliton depends on the ratio $|\beta_2|/\gamma$, which are parameters of the fiber. This was the guideline for a fiber design developed at IRCICA laboratory in Lille (France) in order to obtain high-energy solitons compatible with standard Ti:Sapphire lasers. Furthermore, the solitons are expected to be in the 800 – 1000 nm range, which is of interest for nonlinear microscopy.

2.3.1 Preliminary study

A first fiber, hereafter referred to as SC-PBG-1, was already available at the beginning of this work, as it was designed and fabricated in IRCICA for previous studies [71–73]. Its ability to generate solitons adapted to nonlinear microscopy was tested as a preliminary study. Fig. 2.2(a) shows the scanning electron microscopy (SEM) image of the cross-section of the fiber. The structure is based on silica, with a doubly periodic network of air holes and germanium doped silica rods. The Ge-doped silica rods (light gray regions) have a diameter of $2.19\ \mu\text{m}$ and are separated by a pitch of $3.09\ \mu\text{m}$. Their refractive index profile is parabolic with a maximum refractive index difference of 32×10^{-3} relative to the pure silica background (dark gray region). Air holes (black regions) of $2.33\ \mu\text{m}$ diameter were added periodically to the cladding.

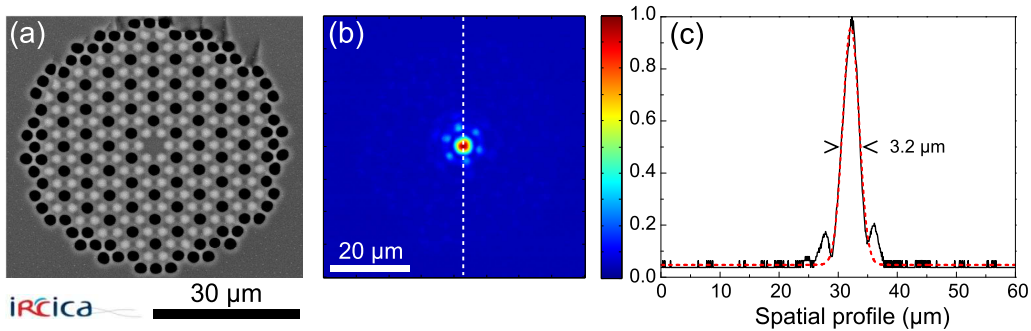


Figure 2.2: (a) Scanning electron microscopy (SEM) image of the core and photonic cladding of the SC-PBG-1 fiber. The dark gray area is the silica, the light gray dots are the Ge-doped rods and the black dots are the air holes. Courtesy of A. Kudlinski. (b) Image of the fundamental mode on a CMOS camera. (c) Spatial profile along the dotted white line in (b). Dotted red line: Gaussian fit.

The setup used for testing the properties of SC-PBG-1 is shown in 2.3. A 80 MHz femtosecond Ti:Sapphire laser tunable between 800 and 1080 nm was used as pump light. An aspheric lens of short focal length ($f = 6.24\ \text{mm}$) mounted on a 3-axis micrometric stage was used for coupling the light in a 10-m portion of SC-PBG-1. To get coupling to the fundamental mode, the exit end of the fiber was imaged on a CMOS camera, and alternative detection paths allowed to measure power with a powermeter (PM) or a photodiode (PD), auto-correlation trace with an autocorrelator (AC), and spectrum with an optical spectrum analyzer (OSA).

Solitons are efficiently generated when the light is coupled to the fundamental mode, so the coupling parameters are critical. To get coupling to the fundamental mode, the exit end of the fiber was imaged on a CMOS camera (DCC1555,

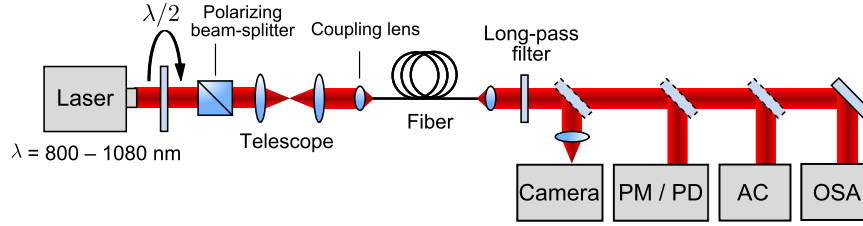


Figure 2.3: Optical setup for the characterization of the SC-PBG-1 fiber. PM: powermeter, PD: photodiode, AC: autocorrelator, OSA: optical spectrum analyzer.

Thorlabs) and the intensity of this mode was maximized. This mode is characterized by a main lobe and six small side lobes. In practice, the optimization is done by maximizing the intensity in the central lobe. This is why a CMOS camera had to be used, as a mere power optimization would most of the time only find local maxima, corresponding to the modes guided by the Ge-doped silica rods. Figure 2.2(b) shows the image obtained on the CMOS camera after coupling to the fundamental mode. Its spatial profile along the dotted white line. Fig. 2.2(c) shows the fit of the spatial profile by a Gaussian function of width $3.2 \mu\text{m}$.

The anomalous dispersion region where the propagation of solitons is possible starts at wavelengths higher than the zero-dispersion wavelength (ZDW) of SC-PBG-1 that was measured to be 905 nm . Efficient soliton generation was only observed from about 950 nm , as pumping wavelengths too close to the ZDW leads to supercontinuum generation. The wavelengths of the spectrally separated solitons were then between 1100 and 1250 nm . An example of spectrum is presented in Fig. 2.4. The spectrum of the 1160 nm soliton is well fitted with a sech-squared function, giving a spectral width of $14.8 \mu\text{m}$. This corresponds to a 96 fs Fourier-transform-limited duration. Unfortunately, the autocorrelation could not be performed at this wavelength to confirm this value because of the limited spectral range of the autocorrelator.

The power of the generated solitons was measured at several pump wavelengths, for several input power and soliton wavelengths. Two quantities are then of particular interest: the soliton pulse energy, calculated from the soliton power and repetition rate of the laser; and the soliton formation efficiency, defined as the soliton power divided by the input power.

When the redshift increases, the energy of solitons increases as well, which can be understood because of the increase in the input power. However, as the input power and redshift increase, the soliton formation efficiency decreases. The solitons are then more powerful but the losses are higher. The soliton energies are between 200 and 600 pJ , which is of the good order of magnitude

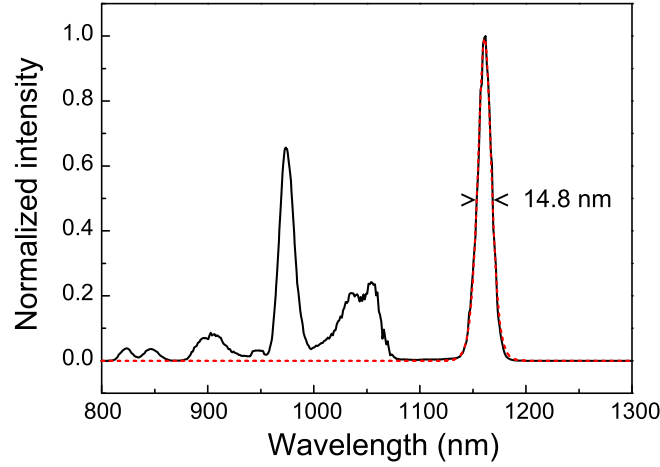


Figure 2.4: Spectrum of the light at the output of a 10-m portion of SC-PBG-1 pumped at 975 nm with 420 mW input power. Power of the soliton: 34 mW. Solid black line: experimental at, dashed red line: sech-squared fit.

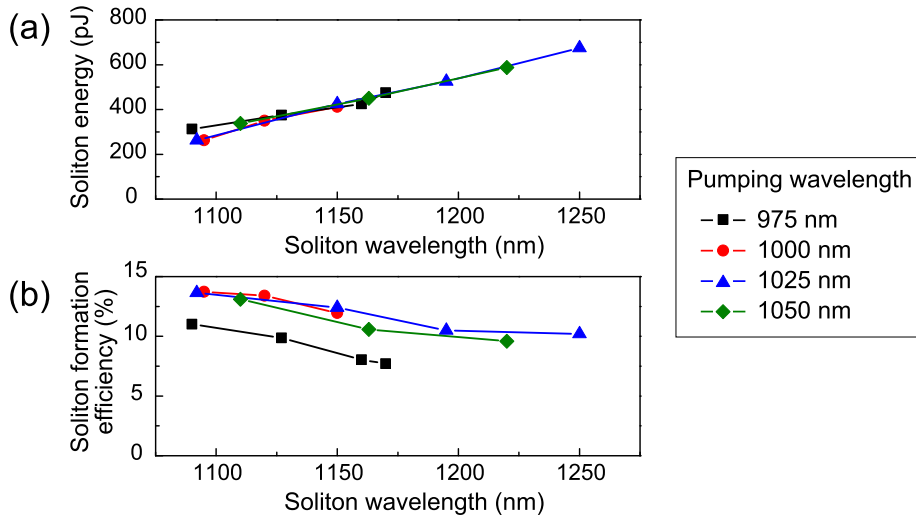


Figure 2.5: (a) Soliton energy and (b) soliton formation efficiency as a function of soliton wavelengths for four pumping wavelengths from 975 nm to 1050 nm.

for nonlinear microscopy. This also corresponds to a 3 to 5-fold enhancement of the pulse energy for classical PCFs [74]. The soliton formation efficiencies from 10 to 15 % are also relatively good. However, due to the high ZDW, the wavelength range is higher than what is usually used in nonlinear microscopy. For this reason, the design of the fiber was slightly modified to get a second

SC-PBG fiber, described in the next section.

2.3.2 Design and characterization of the second SC-PBG

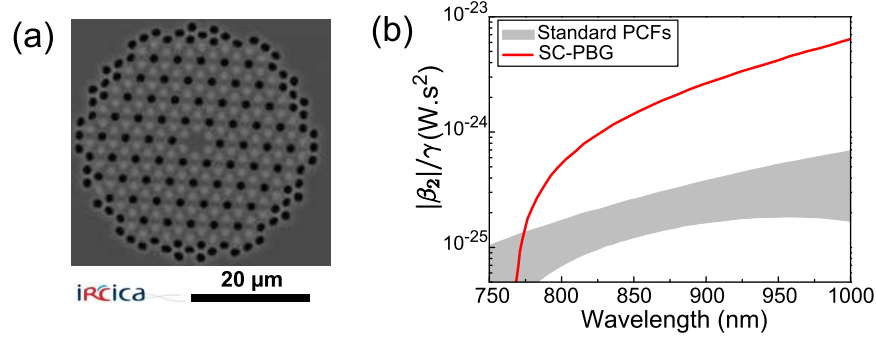


Figure 2.6: (a) SEM image of the cross-section of the core and photonic cladding of the SC-PBG. The dark gray area is the silica, the light gray dots are the Ge-doped rods and the black dots are the air holes. Courtesy of A. Kudlinski. (b) Calculated $|\beta_2|/\gamma$ ratio for standard PCFs and SC-PBG-2.

In view of the promising results detailed above, a second fiber (SC-PBG-2) was designed and fabricated by A. Kudlinski in IRCICA. The strategy was to modify the geometrical parameters of the fiber in order to have a high $|\beta_2|/\gamma$ ratio, and get high energy solitons with a 800 nm pump laser. The SEM image of the cross-section of the core and micro-structured cladding of SC-PBG-2 is shown in Fig. 2.6(a). The Ge-doped silica rods have a diameter of 1.51 μm, are separated by a pitch of 2.40 μm; and the air holes have a diameter of 1.47 μm. Figure 2.6(b) compares the $|\beta_2|/\gamma$ ratio of this fiber (red line), obtained by finite element calculations, with the typical values for standard PCFs (gray area). The increase in the 850 – 1000 nm range is about an order of magnitude. Indeed, for usual air / silica PCFs, high values of $|\beta_2|/\gamma$ require structures with small pitches (Λ) and high air fraction (d/Λ), which make the fibers difficult to manufacture and use. This constraint restricts the $|\beta_2|/\gamma$ ratio to small values. The high $|\beta_2|/\gamma$ ratio should lead to high energy solitons in the desired wavelength range. Moreover, the ZDW of the SC-PBG-2 is 760 nm, so the pumping at 800 nm should allow soliton propagation.

The SC-PBG-2 fiber was first characterized spatially. NIR femtosecond pulses (800 nm, 30 fs, 1 GHz) were launched in sections of the fiber of various lengths for characterization at different input powers. The light was coupled into the fiber with an aspheric lens. The aspheric lens was chosen and the beam diameter was adjusted so that the coupling angle defined by the diameter and focal length of the lens matched the numerical aperture of the fiber, of about $\text{NA} = 0.2$. After

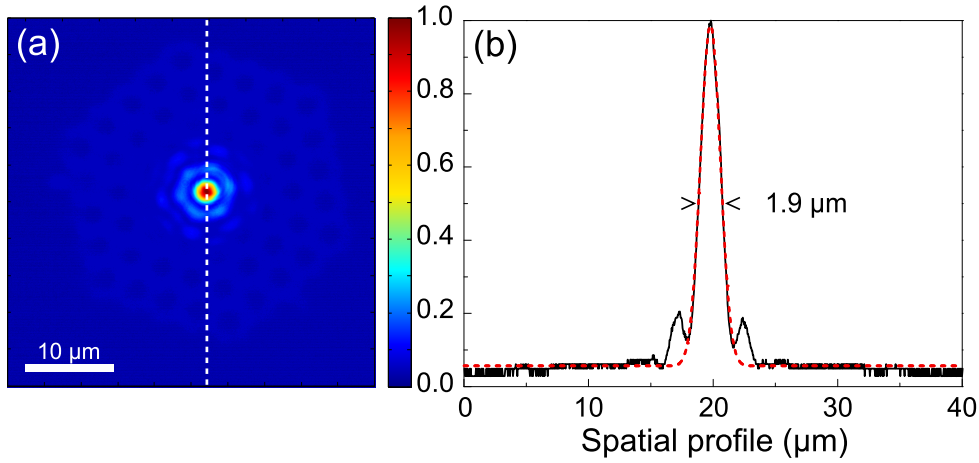


Figure 2.7: (a) Image of the output tip of the SC-PBG-2 fiber on a CMOS camera, after maximization of the fundamental mode. Colorbar: normalized intensity. (b) Spatial profile along the dotted white line in (a). Dotted red line: Gaussian fit.

several trials, a lens of focal length $f = 11$ mm and a beam diameter $D = 4$ mm were chosen.

Figure 2.7(a) shows the image of the tip of the fiber when the fundamental mode is maximized, and Fig. 2.7(b) shows the spatial profile of this mode. The central peak is well fitted by a Gaussian function of width $1.9 \mu\text{m}$, showing that the fundamental mode is Gaussian.

Next, the nonlinear properties of the SC-PBG-2 fiber were characterized. The input power was controlled by a half-wave plate and a polarizing beam splitter. The resulting solitons were filtered from the residue of the laser light at 800 nm as well as blue-shifted dispersive waves by longpass filters (Semrock LP830RU or Thorlabs FEL850) and some of their properties were measured, such as average power, spectrum (USB2000, Ocean Optics), and duration through their autocorrelation trace (Mini, APE).

An example of output spectrum is shown in Fig. 2.8. The red-shifted soliton is perfectly fitted by a squared hyperbolic-secant function (dotted red line). The inset of Fig. 2.8 shows the autocorrelation trace for the 900 nm soliton corresponding to the spectrum. For sech-squared pulses, the width FWHM of the autocorrelation trace was divided by 1.54 in order to recover the pulse duration, which in this case was found to be 90 fs. The Fourier-transform-limited duration calculated from the Fourier transform of the spectrum with the following formula (see Section 1.2.2):

$$\Delta t_{\text{FTL}} = \frac{4 [\ln(1 + \sqrt{2})]^2 \lambda^2 c}{\pi^2 \Delta \lambda}, \quad (2.1)$$

valid for sech-squared pulses. The Fourier-transform limited duration corresponding to the soliton spectral width $\Delta\lambda = 10.7$ nm is $\Delta t_{\text{FTL}} = 80$ fs. The small discrepancy observed between this value and the measured duration can be explained by the dispersion of the optics between the fiber and the autocorrelator (lens, filter, halfwave plate), estimated to be about 800 fs². This is verified by a simple calculation described in Section 4.2.3. This confirms that the soliton is Fourier-transform-limited at the output of the fiber.

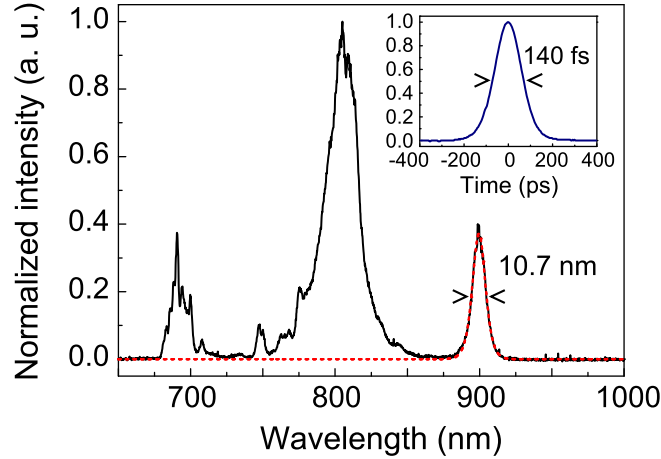


Figure 2.8: Black line: spectrum of the output of the fiber. Dotted red line: squared hyperbolic-secant fit of the soliton. Inset: autocorrelation trace of the 900 nm soliton.

Figure 2.9(a) shows the measured energy of the solitons through the whole tunability window, for five fiber lengths. The energy of the solitons are as high as 120 pJ, which is compatible with nonlinear imaging applications. Shorter fibers produce higher energy solitons, this is due to the losses that increase with the propagation length. For comparison, the energy of one soliton generated in a classical PCF (the one used for the experiments presented later on in Chapter 4) was 30 pJ, at 875 nm and for a 50 cm piece of fiber. This is almost 3 times lower than the power of the 875 nm soliton generated in the 3 m long SC-PBG-2 fiber.

The soliton formation efficiency is shown in Fig. 2.9(b). It is up to 20 % for short soliton wavelengths, and it decreases with increasing soliton redshift. For short fibers, it is approximately between 10 and 15 %, which is equivalent to the first fiber, SC-PBG-1. For the longer fibers, it is extremely low (below 3 %). This point will be addressed in the following.

For each measured point in Fig. 2.9(a), the effective $|\beta_2|/\gamma$ ratio is calculated with Eq. 1.89(b). The power was measured with a regular powermeter, and the obtained data were corrected to take into account the transmission of the

optical filter that was used for separating the soliton from the rest of the output light. Knowing that the solitons were Fourier-transform limited, their duration was calculated from the measured spectra with Eq. 2.1. Figure 2.10 shows the comparison between the experimental value, calculated in the way that was just described; and the theoretical $|\beta_2|/\gamma$ ratio, obtained from finite element method calculations that were performed for the design of the fiber.

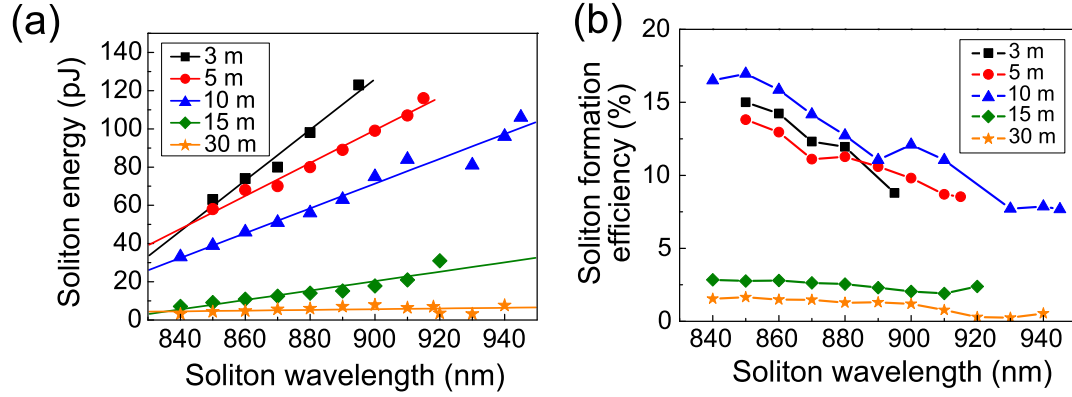


Figure 2.9: (a) Energy of the soliton as a function of soliton wavelength for fiber lengths from 3 to 30 m. The full lines are linear fits of the experimental points for each fiber. Fiber input average powers were (at 1 GHz): 420 – 1400 mW (3 m); 420 – 1360 mW (5 m); 200 – 1380 mW (10 m); 250 – 1300 mW (15 m); 200 – 1400 mW (30 m). (b) Soliton formation efficiency as a function of soliton wavelength for fiber lengths from 3 to 30 m.

A good agreement can be found between the simulation and the experiment for fibers up to 10 m. However, in longer fibers, the calculated $|\beta_2|/\gamma$ ratios are lower than the theory. In a similar fashion, the highest redshift accessible via SSFS increases with fiber length, but it reaches a maximum value at $L = 10$ m (see Fig. 2.11). Moreover, as it was mentioned before, the soliton formation efficiency is also very low for the two longer fibers.

In fibers longer than 15 m, several mechanisms can explain the lower values of the effective $|\beta_2|/\gamma$, the end of the redshift and the low efficiency. First, the third-order dispersion arising when the soliton gets closer to the PBG edge decelerates the SSFS in the fiber [71]. Second, the attenuation experienced by the pulse when it propagates increases the nonlinear length $L_{NL} = 1/(\gamma P_0)$ which is the characteristic length needed for the soliton to adapt to any changes. At a certain point the soliton can no longer follow the changes in P_0 , ceases to redshift, and temporally broadens under dispersion. In the end, the redshifted pulse loses its soliton nature during propagation, and Eq. 1.89 is no longer valid. Figure 2.11 can be interpreted as the redshift vs. fiber length. In view of the

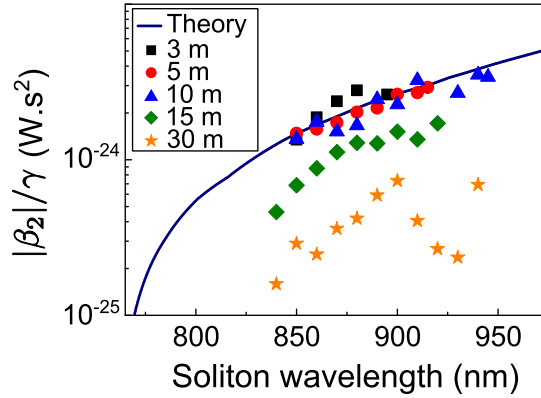


Figure 2.10: Theoretical $|\beta_2|/\gamma$ ratio (dark blue line) from finite elements calculations, and experimental values of this ratio (markers) retrieved from measurement of the energy (data in Fig. 2.9(a)) and the retrieval of their duration from the Fourier transform of the spectrum of the solitons, plotted against soliton wavelengths, for several fiber lengths.

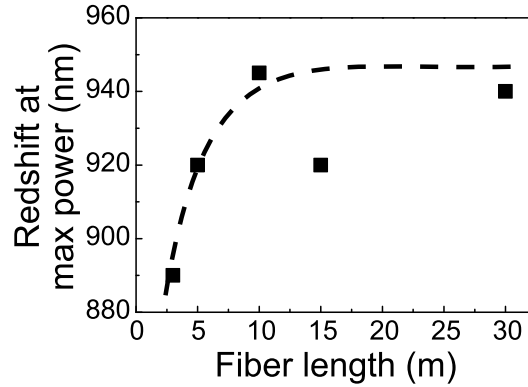


Figure 2.11: Redshift of the soliton at maximum input power for varying fiber lengths. The dashed line is a guide to the eye.

above explanation, that soliton nature of the pulse can be seen as retained until the plateau.

Finally, a 100 nm tuning range was obtained for the soliton. The length of the fiber must be less than 10 m so that Eq. 1.89 is still valid and the output pulse is Fourier-transform-limited. Then, the fiber length should be chosen according to the tunability and power requirements for the application.

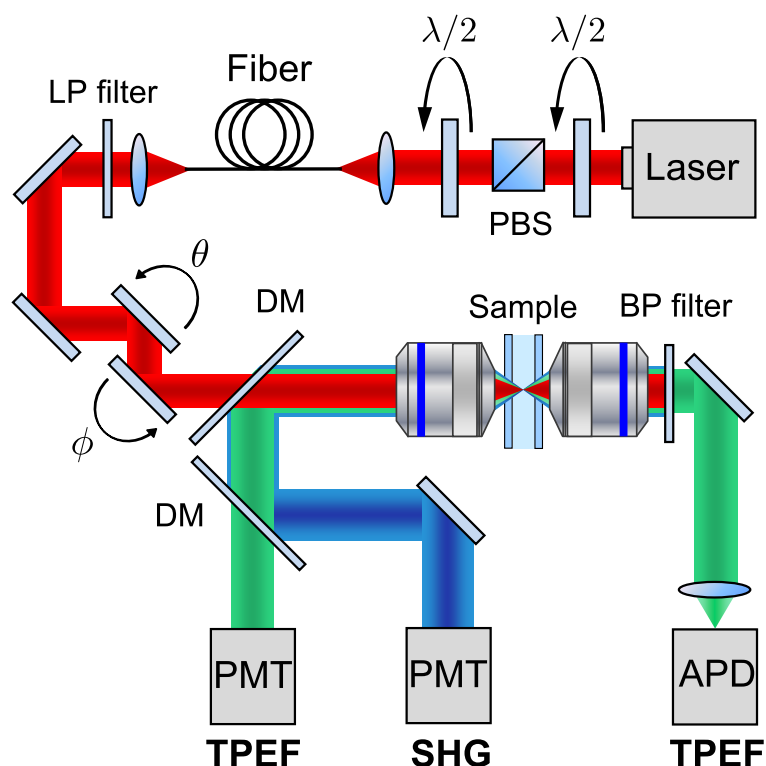


Figure 2.12: Scheme of the microspectroscopy and microscopy setup. PBS: polarizing beam splitter, $\lambda/2$: half-wave plate, DM: dichroic mirror, LP/BP filter: longpass/bandpass filter, PMT: photomultiplier tube, APD: avalanche photodiode.

2.4 Two photon fluorescence and second harmonic generation

One of the simplest ways to take advantage of the short duration of the pulses obtained at the tip of the fiber is to directly send them to a sample and attempt to generate nonlinear signals to provide contrast. This section sums up the results obtained with this approach.

2.4.1 Experimental setup

We conducted two sets of experiments based on the excitation of the sample by the optical solitons generated in the fiber. First we performed microspectroscopy on liquid samples, and then we did microscopy on several samples, including biological ones.

The solitons were generated by coupling 800 nm light from either a 80 MHz (Chameleon from Coherent Inc., 150 fs) or a 1 GHz laser (GigaJet20 from

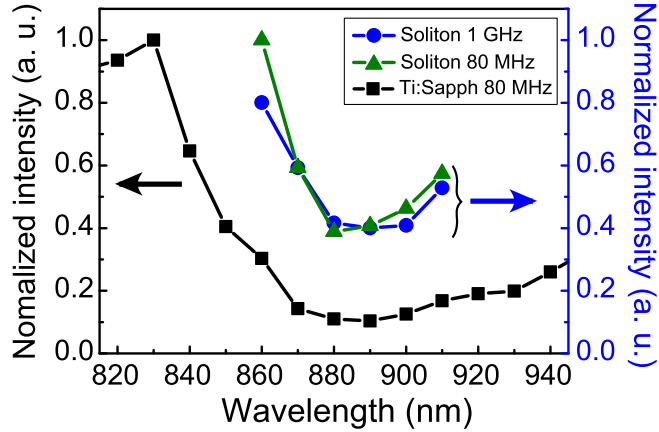


Figure 2.13: TPEF spectra of a 170 μM solution of rhodamine 6G in water. Black squares: reference spectrum, measured by exciting the sample with the tunable fs light directly coming from the 80 MHz Ti:Sapphire laser (without passing through the fiber). Blue circles: spectrum acquired under excitation with solitons generated in a 10 m SC-PBG-2 fiber pumped with a 800 nm, 1 GHz laser. Green triangles: spectrum acquired under excitation with solitons generated in a 10 m SC-PBG-2 fiber pumped with a 800 nm, 80 MHz laser.

LaserQuantum, 30 fs) into the SC-PBG-2 fiber. The 10 m fiber was used for spectroscopic application because it displays the best trade-off between tunability and soliton power, and the 3 m fiber was used for microscopy to get high soliton power. As before, the soliton wavelength was controlled by changing the input power, and it was filtered from residual and dispersive waves with a long-pass filter to ensure that the soliton was the only excitation pulse reaching the sample. For microspectroscopy, the light was focused on the sample by a long working distance objective (Olympus 20x, $\text{NA} = 0.45$) and collected by another objective ($\text{NA} = 0.60$) in the forward direction. We detected the TPEF on an APD after a set of longpass and bandpass filters.

For microscopy, we used a high NA objective (Nikon 40x, $\text{NA} = 1.15$, water immersion) and scanned the focus across the sample with galvanometric mirrors to make TPEF and SHG images in an epi-detection scheme by using two PMTs and an appropriate set of filters and dichroic mirrors.

A scheme representing the two setups combined is shown in Fig. 2.12.

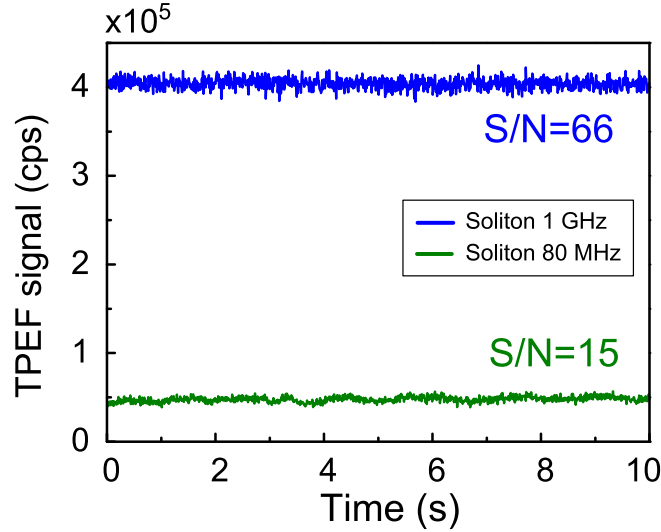


Figure 2.14: TPEF traces under excitation with 870 nm solitons at 1 GHz (blue line) and 80 MHz (green line), with the corresponding signal to noise ratios (in $\text{cps}^{1/2}$). Powers at the focus: black curve: 15 mW; blue: 5 mW; green: 2 mW.

2.4.2 Nonlinear spectroscopy

We investigated the TPEF response of an aqueous solution of rhodamine 6G with the setup described above. We first compared the fluorescent levels and the signal to noise ratios in the cases of the excitation by solitons generated in the fiber at 80 MHz and at 1 GHz.

The TPEF signal at a given wavelength depends on pulse power, duration and repetition rate f_{rep} in the following way [75]:

$$\langle F \rangle \propto \frac{P_{\text{av}}^2}{f_{\text{rep}} \cdot T_0} = 4P_0^2 \cdot T_0 \cdot f_{\text{rep}}, \quad (2.2)$$

where P_{av} is the average power and P_0 is the peak power. The energy and duration of one soliton at a given wavelength is fixed by the fiber parameters. Consequently, the only way to significantly increase the TPEF signal in this scheme is to increase the repetition rate.

More specifically, we expect the fluorescence signal to scale linearly with the repetition rate. If the TPEF photon count S_{1sol} arising from excitation with a single soliton has mean $\langle S_{\text{1sol}} \rangle$ and standard deviation σ_{1sol} , then it follows from the properties of the standard deviation that the TPEF count rate arising from a train of solitons at repetition rate f_{rep} has mean $\langle S \rangle \propto f_{\text{rep}} \langle S_{\text{1sol}} \rangle$ and standard deviation $\sigma \propto \sqrt{f_{\text{rep}}} \sigma_{\text{1sol}}$. We can then expect both the noise and the signal to noise ratio to scale with the square root of the repetition rate.

We measure a 10-fold increase of the fluorescence counts and a 4-fold increase of the signal to noise ratio under a 12.5-fold increase of the repetition rate (from 80 MHz to 1 GHz), as shown in Fig. 2.14. The experiment data seem to generally follow the trend predicted by the above calculation. This indicates that we observe only limited saturation effects in the sample when increasing the repetition rate.

This emphasizes the advantages of increasing the repetition rate in terms of signal level and signal to noise ratio. Previous studies also suggest that photo-damage associated with multiphoton excitation fluorescence decreases when the repetition rate increases while keeping a constant signal rate [76]. Indeed, for some processes

Figure 2.13 shows the TPEF spectra of the same rhodamine 6G solution. The two spectra (blue circles and green triangles) obtained with excitation by solitons at 80 MHz and 1 GHz were normalized with respect to their average power and repetition rate, taking into account the small saturation effect previously measured. The agreement between the two spectra is very good, proving the reliability of the soliton as a light source with only little influence of the parameters of the pumping laser (spectrum, duration, chirp). Another spectrum was performed as a control, using the fs pulse directly coming from the 80 MHz Ti:sapphire laser (black squares) for excitation. The spectra show a good qualitative agreement. Our measurements are also consistent with the two-photon absorption cross section values for rhodamine 6G found in the literature [75, 77]. However, no quantitative information can be retrieved from the comparison between this spectrum and two first spectra because many parameters vary (spectral width, pulse duration, beam shape).

The speed of wavelength tuning is only limited by the capabilities of the devices used to change the power at the input of the fiber. For example, with a Pockels cell, one could get wavelength switching frequencies up to few MHz. In the current configuration, the wavelength tuning is repeatable enough to operate in an automated fashion over the course of a set of experiments (typically few hours).

2.4.3 Nonlinear microscopy

To demonstrate the imaging capabilities of our system, we performed images of several samples, including biological ones (see Fig. 2.15). We generated the solitons at 1 GHz repetition rate in a 3 m fiber to operate at high excitation power and low redshift (850–890 nm). We first tested the two epi-detection channels separately to obtain images of samples known for their strong TPEF and SHG signals, respectively. Figure 2.15(a) shows a TPEF image of a fixed *Drosophila* embryo, where the formaldehyde fixation process is responsible for inducing the fluorescence signal. Figure 2.15(b) shows the SHG image of BaTiO₃

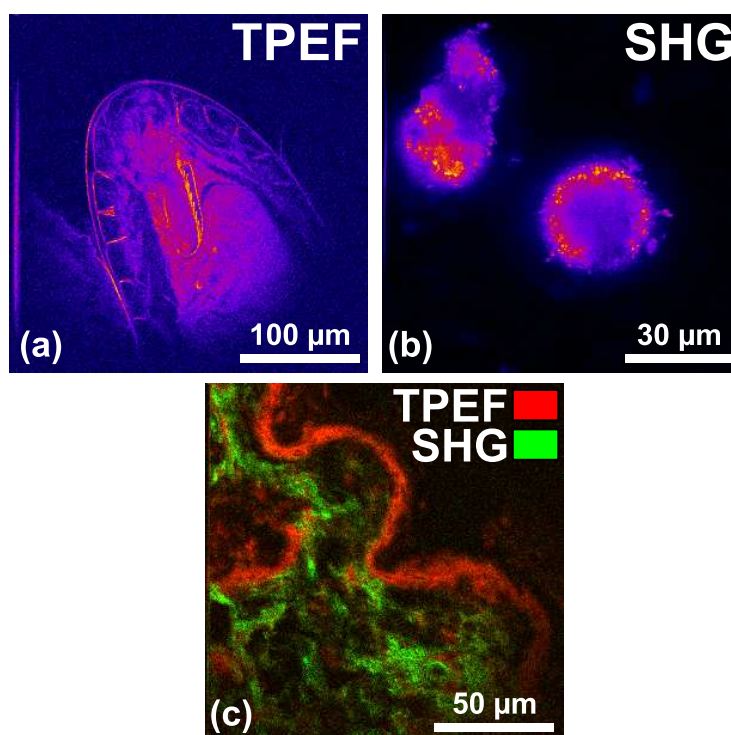


Figure 2.15: 300 x 300 pixels TPEF and SHG images with 10 accumulations each. (a) TPEF image of a fixed *Drosophila* embryo obtained with a 870 nm soliton excitation and a 50 μs dwell time. (b) SHG image of BaTiO₃ crystals obtained with a 850 nm soliton excitation and a 70 μs dwell time. (c) Composite image of fixed mouse tumor skin tissue obtained with a 870 nm soliton excitation and a 70 μs dwell time. TPEF is shown in red and SHG in green. Powers in the sample plane: (a) 40 mW; (b) 50 mW; (c) 55 mW.

crystals. In both cases, the 50–70 μs dwell times that were used are comparable with the ones typically used in nonlinear microscopy. The multiphoton signal is about 10 times lower than images with standard Ti:Sapphire excitation. We have identified the reason for this discrepancy to be the spatial profile of the soliton that is singly-peaked but not Gaussian. The microscope we used was not set up to compensate for this effect, which results in a bias against the soliton in this context. We then used the two channels to perform a multimodal image of a biological sample. Figure 2.15(c) shows a composite TPEF/SHG image of fixed mouse tumor skin tissue showing structural features that are not distinguishable in white light microscopy. The SHG emitting structures can be identified as collagen fibers, whereas TPEF comes from the stratum corneum.

2.5 Conclusion

Soliton generation and redshift in a solid-core photonic bandgap fiber was applied for the femtosecond fiber delivery in a microspectroscopy and microscopy scheme. The fiber design was optimized to allow the generation of a high energy soliton, and the laws of soliton dynamics ensured Fourier-transform-limited pulse at the exit end of the fiber, with no need of pre-compensation for dispersion. For those reasons, the soliton excitation scheme is efficient for the generation of observable nonlinear signals (such as TPEF and SHG) in the focal volume. Furthermore, the power-dependent redshift of the soliton provides a 100 nm tunability range, opening the door to spectroscopic applications and hyperspectral imaging.

3 Chapter 3: Pump-probe measurements of transient absorption

3.1 Transient absorption

Time-resolved spectroscopy has been used since the 1950s to study the dynamics of physical, chemical, or biological processes. The first techniques to be used were the accelerated and stopped flow method [78], based on the flowing of the liquid sample in a tube, and the flash photolysis [79], relying on the emission of a short flash of light from a high-pressure gas filled discharge tube. With the first technique, it was possible to study the kinetics of biochemical reactions at first on the millisecond scale, while the second technique improved over the years to reach the nanosecond scale. The development of ultrafast lasers allowed to push down this limit and access picosecond and femtosecond time scales. A wide variety of techniques have been implemented so far for studying dynamic samples, such as fluorescent lifetime measurements, pump-probe methods or time-resolved coherent anti-Stokes Raman scattering.

The principle of pump-probe experiments is the following. Two synchronized beams of light are sent to the sample. One of the beam passes through a delay line, so that the relative position of the two pulse trains can be changed. Then, the first pulse reaching the sample modifies its state, and this state is probed by the second pulse, at different times depending on the position of the delay line. The transient absorption of the probe beam caused by the action of the pump beam on the sample is measured by monitoring the change of intensity of the probe beam. This allows to release the constraint on the time response of the detectors, and the time resolution depends on the pulse duration only. Femtosecond resolution can then be achieved with the need of ultrafast detectors. When scanning the delay stage, a time trace that probes the dynamics of the process is recovered. Two types of setups are classically used. The first configuration is a mono-color scheme, where the two beams come from the same laser, are split in two, and recombined in the sample with different angles in order to only detect the probe beam. The second configuration is a two-color scheme, where the second beam is generated from the first one, with parametric generation, harmonic generation or supercontinuum generation, for example. Then the excitation can potentially be done in a collinear configuration, with optical filters to separate the beams. In a spectroscopic modality, the frequency of the pump or probe beam can be changed to access dynamic spectral information.

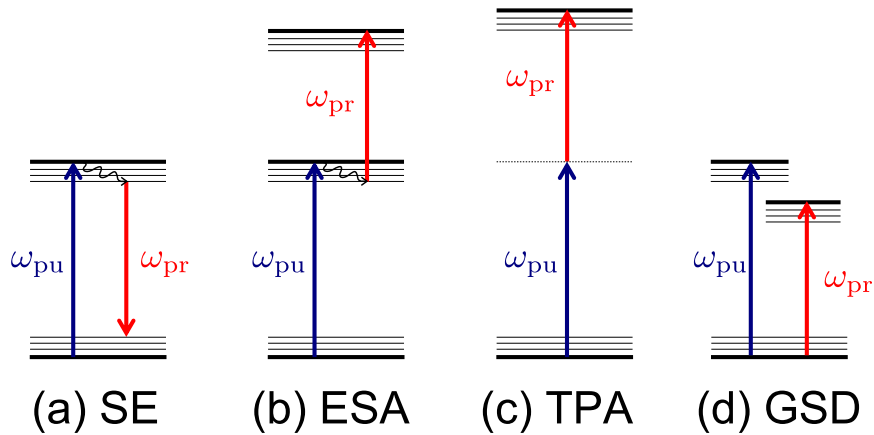


Figure 3.1: Energy diagrams for (a) stimulated emission, (b) excited state absorption, (c) two-photon absorption and (d) ground-state depletion.

Several processes can contribute to transient absorption signal in pump-probe experiments [80]. Each of them either increases or decreases the detected absorption of the probe beam. This change can be expressed in terms of change of intensity of the probe beam ΔI or change of absorption ΔA , those two quantities having opposite signs. In the following, the pump-probe signal is defined as the change in intensity $\Delta I = I_2 - I_1$, where I_2 is the intensity of the probe beam when the pump beam is present, and I_1 is the intensity of the probe beam alone.

Stimulated emission. In stimulated emission, a photon impinging on a molecule in an exciting state can de-excite it, causing the emission of a coherent photon, identical to the first one. This is the basic principle of light amplification in lasers. In a pump-probe scheme, the pump pulse brings the molecules to an excited state (see Fig. 3.1(a)), so the efficiency of stimulated emission is higher compared to the case where the probe beam is alone ($\Delta I > 0$). The probe beam is then interrogating the transient excited state of the molecule, and its lifetime, typically in the picosecond range.

Excited state absorption. The pump beam brings the molecule to an excited state, from which occurs the absorption of the probe beam (see Fig. 3.1(b)). When the pump beam is absent, the absorption from the excited state does not occur. The pump-probe signal is then negative ($\Delta I < 0$). Like stimulated emission, excited state absorption probes the lifetime of the excited state. Conversely, two-photon absorption is the simultaneous absorption of two photons via a virtual state (see Fig. 3.1(c)). It also generates a negative pump-probe signal, but its simultaneous nature ensure that no TPA signal persists when the pump and probe pulses do not overlap anymore.

Ground-state depletion. In this case, the pump and the probe beam are both

absorbed from the ground state (see Fig. 3.1(d)). When the pump beam is present, its absorption is competing with the absorption of the probe beam, finally the pump-probe signal is negative ($\Delta I < 0$). In other words, the absorption of the pump beam causes a transient depletion of the population of the ground states, which decreases the efficiency of absorption of the probe beam.

Other processes can further contribute to the measured pump-probe signal. For example, cross-phase modulation (XPM) results from the change of refractive index of the medium when strongly illuminated. This local change of refractive index due to the pump beam acts as a lens for the probe beam. Therefore, the divergence of the beam is slightly modified, which can be interpreted as a gain or loss in signal if the detector does not collect the entire cone of light emitted by the sample. Depending on the sample and the experimental conditions, this effect can generate positive or negative pump-probe signal. A second process that can be detected as well is the stimulated Raman scattering (SRS). Due to the vibrational resonances of the molecular bonds in the sample, an energy transfer occurs from the low wavelength beam to the high wavelength beam. The origin and properties of SRS will be discussed in detail in Chapter 4. Depending on the wavelengths of the pump and probe beams, the pump-probe signal due to SRS can be either positive or negative. Like TPA, both XPM and SRS are instantaneous processes, so their effects are present only when the pump and probe pulses overlap.

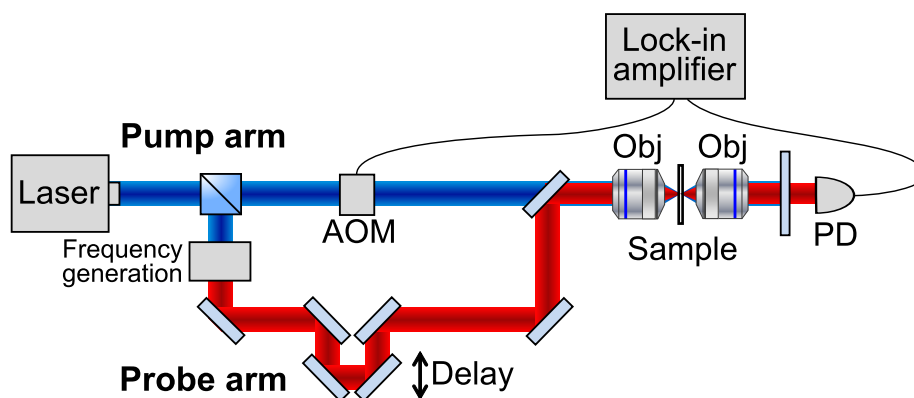


Figure 3.2: Setup for nonlinear pump-probe microscopy. AOM: acousto-optic modulator, PD: photodiode.

Nonlinear absorption has been observed by directly monitoring the intensity of the probe beam, for example for studying photosynthetic systems (see for instance the review from Berara and co-workers [81]). However, the power requirements for directly measuring nonlinear absorption are high for processes that give rise to absorption changes of the order of 10^{-3} and less, where the noise coming from laser fluctuations start to overcome the signal. Fu and co-

workers [82] presented in 2007 an alternative scheme to improve the sensitivity of nonlinear transient absorption measurements. The pump beam is modulated at a frequency f by an acousto-optic modulator (AOM), and the resulting modulation of the intensity of the probe beam is detected with a photodiode and demodulated in a lock-in amplifier to recover pump-probe signals with a typical sensitivity of 10^{-6} . The scheme of the setup is shown in Fig. 3.2.

Warren's group pioneered this field [83, 84] and used a transient absorption microscopy setup for the study of melanin. Melanin is a pigment naturally present in plants and animals [85]. In particular, there is melanin in human hair, skin and eyes. In skin, melanin is produced and stored in cells called melanocytes, which are responsible for skin color. Melanin plays a photoprotective role against UV light, by absorbing UV radiation and dissipating its energy through non radiative decay [86]. UV exposure stimulates the production of melanin in skin (this is the mechanism of sun tanning), and it also increases the risk of melanoma, which is a form of skin cancer involving the abnormal development of melanocytes [87]. There are two types of melanin in skin: eumelanin, which is black, and pheomelanin, which is brown-red [88]. Both are polymers that have close interactions with proteins and metal ions in melanocytes. Eumelanin and pheomelanin have different pump-probe responses that have been studied [89, 90] and applied to melanoma imaging [91].

3.2 Pump-probe experiment with soliton delay

As mentioned in Section 1.3.3, a femtosecond soliton propagating and redshifting through SSFS in a PCF is sensitive to a change of input power, that (i) modifies the wavelength of the soliton at the output of the fiber, and (ii) also changes its delay. The SC-PBG fiber described in Section 2.3.2 can then be used for generation of the probe wavelength in a dual-color pump-probe, and for the delay scanning realized before through mechanical stage translation.

The scheme of the proposed setup for transient absorption measurements in a pump-probe configuration is shown in Fig. 3.3. It is very similar to the setup used in Warren's group (Fig. 3.2). The 1 GHz, 800 nm Ti:sapphire laser presented in Chapter 2 was used for generating both the pump and probe beams. The 800 nm beam passes through the AOM for modulation at 1 MHz, it is the pump beam. A mechanical delay line is placed on the path of the pump beam in order to temporally overlap the pump and probe beam on the sample. On the other arm of the setup, the probe beam is generated by soliton formation and redshift in the SC-PBG-2 fiber. The delay scanning is obtained by changing the input power with a Pockels cell and a polarizer. The Pockels cell turns the linear polarization of the light, and the polarizer only let pass the light along its main polarization axis, hence the intensity modulation. The Pockels cell's

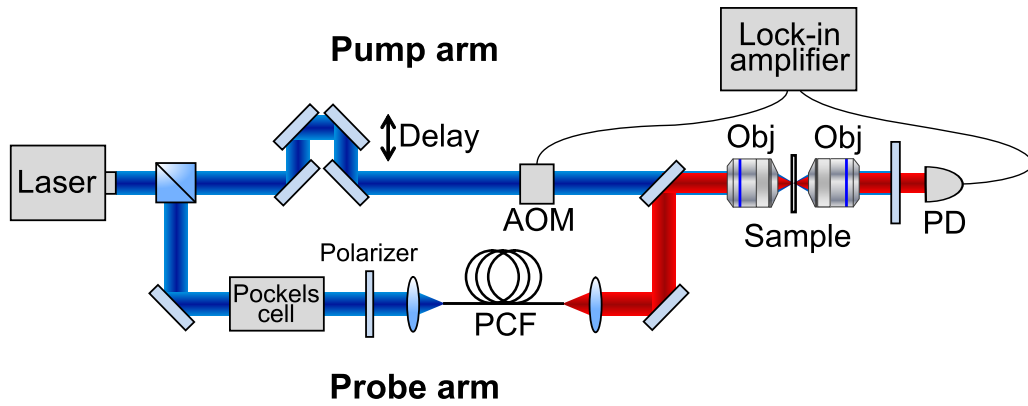


Figure 3.3: Setup for nonlinear pump-probe microscopy with Pockels cell scanning. The mechanical delay line on the pump arm was set up for calibration of the Pockels scan and comparison between the two scanning methods.

input voltage is changed through a National Instrument acquisition card, so the power at the input of the fiber is modified in a controlled way. In order to control the delay of the soliton at the output, the relationship between applied voltage and delay through input power and soliton wavelength has to be studied and calibrated. This calibration can be done by comparing the pump-probe traces of a strongly absorbing sample first acquired by the scanning of the translation stage on the pump beam and then by the scanning of the Pockels cell's input voltage.

SSFS induced delay

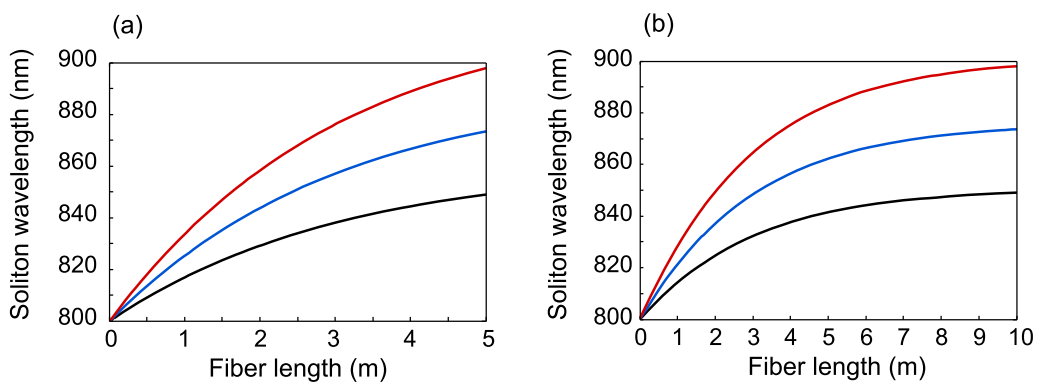


Figure 3.4: Trajectories of a few solitons in the $\lambda(z)$ plane for two different fiber lengths. (a) $L = 5$ m; (b) $L = 10$ m.

The soliton wavelength changes through SSFS when the power at the input of the fiber is modified. As a result, the trajectory of those two solitons in the (λ, z) plane will be different. Many parameters of the fiber are wavelength dependent, such as the group-velocity dispersion and the nonlinear coefficient. In a similar way, the group velocity of the pulse is also wavelength-dependent. Let us recall that the group velocity v_g is related to the first order coefficient of the Taylor development of the pulse's spectral phase, β_1 (see Eq. 1.26), in the following way: $v_g = \beta_1^{-1}$. Knowing the fibers parameters as a function of λ , and knowing the trajectory $\lambda(z)$ of each soliton, it is possible to estimate the delay accumulated by the solitons when they experience a different series of group velocities during their propagation. With Fig. 2.11, we can estimate what is the trajectory of one soliton in a fiber of a given length, at maximum power. As an approximation, we can consider that the trajectories for lower powers have the same shape. It is then possible to compute the delay accumulated by each soliton. Some of those estimated trajectories are shown in Fig. 3.4. This calculation has been done for the SC-PBG-2 fiber, for which all the fiber parameters are known.

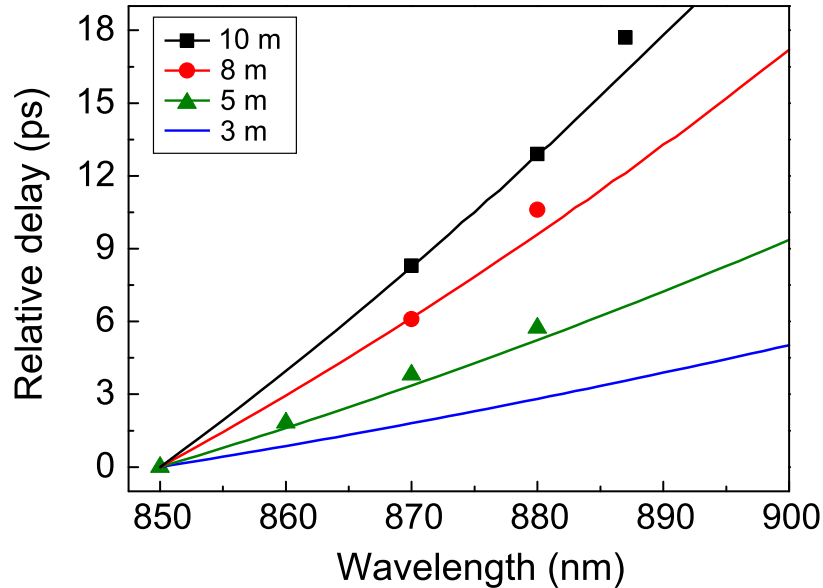


Figure 3.5: Comparison between calculated and experimental relative delay of redshifted solitons for four fiber lengths. The lines are the calculated data, and the square markers are the experimental values.

The relative delay of shifted solitons has also been experimentally measured for fibers of three different lengths. The comparison between calculation and experiments are presented in Fig. 3.5 and shows a very good agreement. The delay to wavelength relationship is close to linear for short fibers over a short

range of soliton shift differences.

For pump-probe experiments, it is desirable to get the highest possible delay shift per wavelength unit, because the transient response of a sample might change if the probe wavelength is too much changed. In that respect, the longer fiber would be the best as it provides the highest delay shift per wavelength unit. However, the delay fluctuation due to small input power fluctuation or small changes in the coupling are bigger in longer fibers. The time resolution of the technique is linked to the duration of the pulses and its precision, so for this practical reason, the 5 m fibers was chosen for performing the experiments. The overlap between pump and probe was estimated at the sample plane by measuring their cross-correlation on a BBO crystal. The width of the autocorrelation was $\Delta t_{AC} = 180$ fs, which approximately corresponds to two overlapping 120 fs pulses.

3.3 Experimental results

As a first demonstration of feasibility, the pump-probe trace of an absorbing sample was acquired by scanning a delay stage, for four different soliton wavelengths. The sample was chosen to be a diluted solution of black ink (Quink black from Parker), because it gives a strong pump-probe signal and is readily available. In order to compare them to each other, the pump-probe time traces were normalized, and the origin of the delay axis was arbitrarily chosen at the minimum of the signal for each trace. The results are presented in Fig. 3.6. In the probe wavelength range 850 – 880 nm, no significant change in the pump-probe trace. This means that for this sample and in this wavelength range, the soliton delay shift can be used as a scanning mechanism.

However, a calibration procedure has to be followed in order to obtain the same results from the scanning with the translation stage and the scanning via soliton shift. Figure 3.7 shows eight scans that were performed with translation stage scanning, for eight different soliton wavelengths. The delay shift is clearly visible. However, this experiment also reveals the change in signal amplitude, mainly due to the difference in transmission of the optics. This needs to be taken into account in the signal processing step.

Figure 3.8 shows the amplitude and delay dependence to the soliton wavelength shift obtained from the scans showed in Fig. 3.7. A linear fit perfectly matches the delay to wavelength relationship, as predicted in Section 3.2. The slope is about 0.15 ps/nm, so a delay scan of 4.5 ps in the investigated 30 nm wavelength shift range. The characteristic time of the processes involved in transient absorption is about 1 ps, so the delay range is appropriate for pump-probe experiments.

The amplitude to wavelength relationship is less obvious, as it depends on

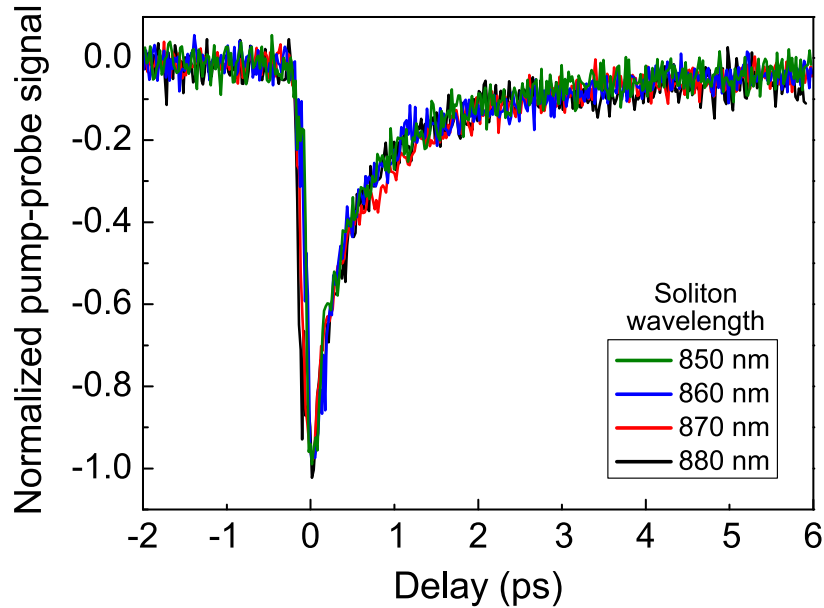


Figure 3.6: Normalized pump-probe trace of black ink (dilution factor 8), acquired by scanning the delay stage with different soliton wavelengths. For comparison purposes, the arbitrary origin of the relative delay axis has been assigned to the minimum value of the pump-probe trace, for each scan.

many parameters such as the optical power of the soliton that varies with the wavelength, and the optical transmission of the optics. In this configuration, a third-order polynomial functions seems to fit the data quite well. A zone of constant amplitude is also observed for soliton wavelengths between 860 and 875 nm, which provides a 2.25 ps distortion-free delay range.

One of the most critical step of the calibration is the voltage to delay relationship. The voltage generated from the NI acquisition card is between -0.5 V and +2 V, then it is linearly amplified by the Pockels cell amplifier to the -50 V to 250 V range. This linearly turns the polarization of the light. The polarizer then cuts the part of the light that is not along its main axis, which results in a sine-square dependence of the intensity of the light on the applied voltage. This is verified in Fig. 3.9(a), where the sine-square fit perfectly matches the experimental data.

Figure 3.9(b) shows the most critical part of the calibration that is the link between optical power at the input of the fiber and soliton wavelength. This relation is not straightforward, as it depends on coupling efficiency and soliton generation, which cannot be controlled. The best solution is then to carefully establish a calibration table, that can be fitted with a fifth order polynomial

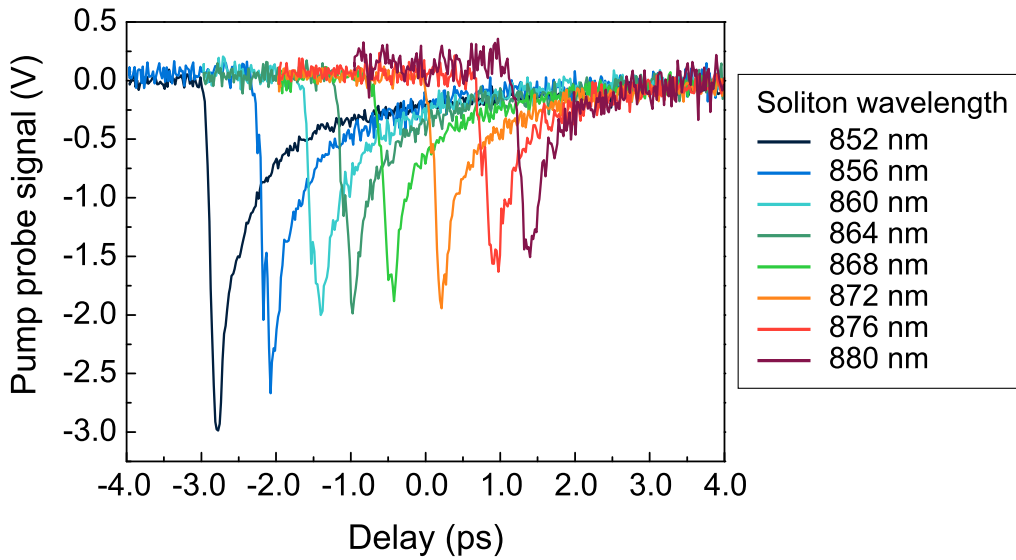


Figure 3.7: Pump-probe traces of black ink (dilution factor 2) acquired by scanning the delay stage, for eight different soliton wavelengths. Gain of the lock-in amplifier: 10^6 .

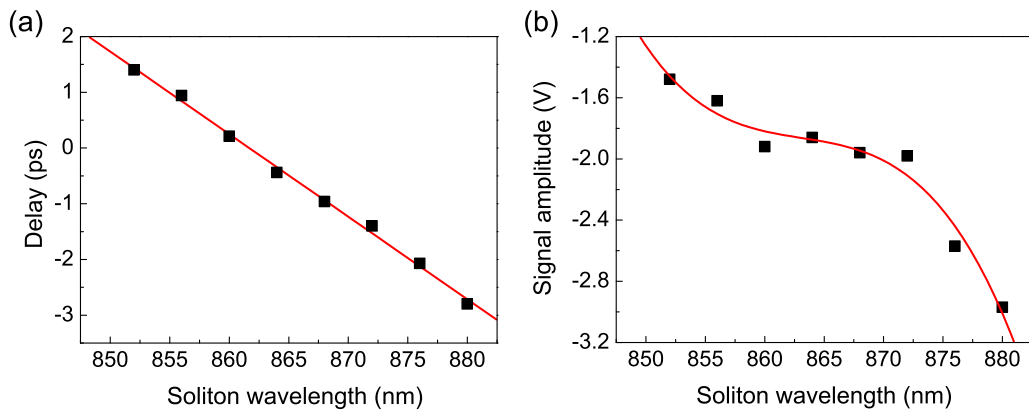


Figure 3.8: Calibration curves retrieved from Fig. 3.7. (a) Soliton delay as a function of soliton wavelength. Black squares: experimental data, red line: linear fit. (b) Maximum amplitude of the pump-probe signal as a function of soliton wavelength. Black squares: experimental data, red line: third-order polynomial fit.

function for practical reasons. Then, this calibrated function can be used to assign each data point acquired at a certain applied voltage value to a certain delay.

In order to compare mechanical with voltage-induced delay scanning, several

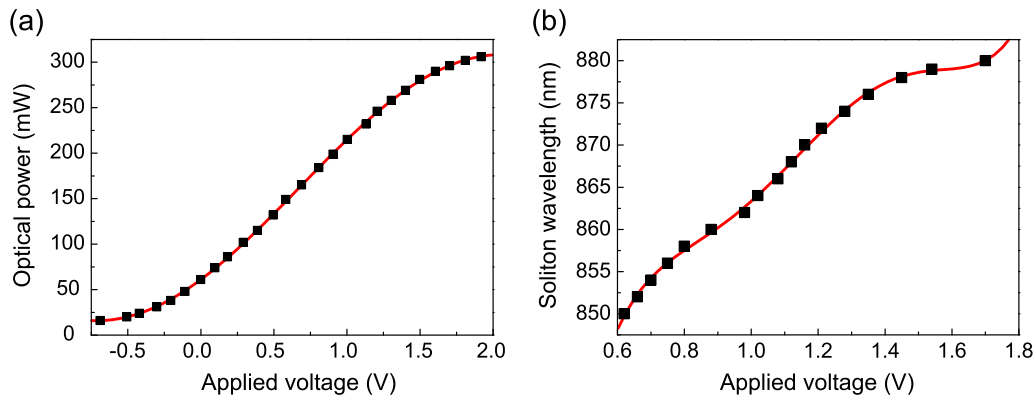


Figure 3.9: (a) Optical power after the Pockels cell and the polarizer as a function of the voltage applied to the Pockels cell amplifier. The black squares are the experimental data and the red line is the sine-square fit. (b) Wavelength of the soliton as a function of the voltage applied to Pockels cell before amplification. Black squares: experimental data, red line: fifth order polynomial fit.

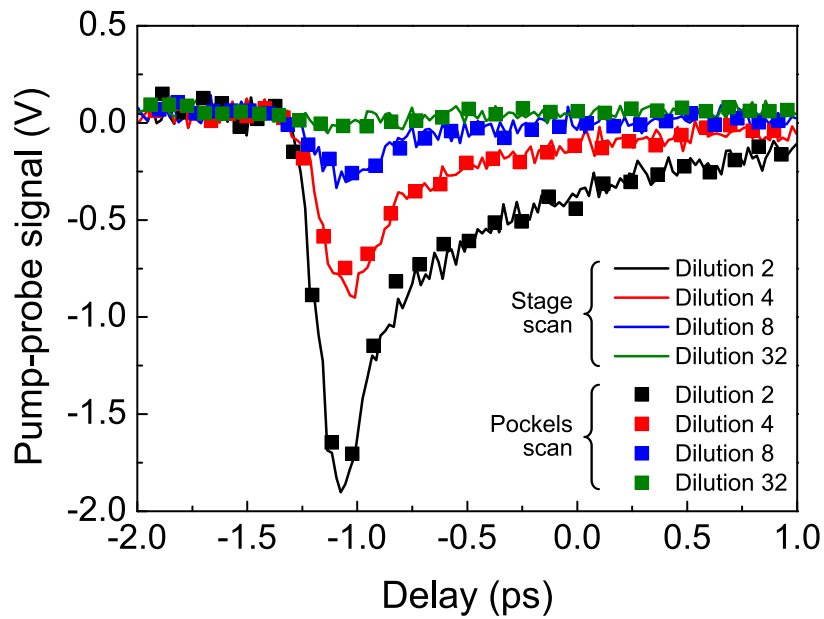


Figure 3.10: Comparison between translation stage scan (solid lines) and Pockels cell scan (squares), for four different concentrations of black ink. Gain of the lock-in amplifier: 10^6 .

pump-probe traces were acquired with both methods, on four solutions of black ink of different concentration. The power at the sample were identical for the

two sets of experiments: about 10 mW for each pump and probe beam. The results are shown in Fig. 3.10. The solid lines represent the data acquired by mechanically scanning the delay. For each curve, 150 points were taken with a dwell time of 100 ms for the three most concentrated solutions, and 200 ms for the solution with dilution factor 32. The time of acquisition has also to take into account the communication time between the computer and the translation plate, that added an extra 150 ms for each point. In total, the acquisition time was 30 and 50 s per curve for 100 and 200 ms dwell time, respectively. The square markers represent the data acquired by scanning through the change of voltage applied to the Pockels cell. This time, 30 points were taken for each solution. The dwell times per point varied with concentration in order to keep a good signal to noise ratio: dwell times of 10, 50, 100 and 200 ms were used for solutions with dilution factor 2, 4, 8 and 32, respectively. Although the dwell times are comparable with the ones used in the previous configuration, the use of the voltage scan allowed to considerably reduce the communication times. Indeed, the total time of acquisition for 50 points with a dwell time of 100 ms was about 5 s, so the communication time has become negligible compared to the dwell time.

The agreement between the traces obtained with mechanical delay and voltage-induced delay is very good, for the four tested solutions. This demonstrates the reliability of the calibration procedure, and validates the technique as a powerful method to recover pump-probe traces.

3.4 Conclusion

The interest of voltage-controlled soliton delay scanning for transient absorption measurements in a pump probe configuration was demonstrated. This system allows for faster acquisition, up to the MHz range, and an increased versatility as any delay can be probed at any time upon the change of the voltage applied to the Pockels cell. This way, strategies for more efficient sampling of the delay traces can be designed, and applied for imaging of absorbing materials such as melanin.

4 Chapter 4: Coherent Raman scattering

4.1 Principles of coherent Raman scattering

Every molecule is made of molecular bonds that can vibrate in response to an excitation. A molecular bond can be modeled by a harmonic oscillator, similar to a mass/spring system for example. Then, each chemical bond possesses its own resonance frequency that depends on the atoms that are linked and on the environment of the bond (other atoms in the molecule, hydrogen bonds, temperature, etc.) A molecule is characterized by a vibrational spectrum from which it is possible to retrieve information about the bonds it contains and their environment. Similarly, the vibrational spectrum of a mixture of molecules carries information about its chemical composition. Two modalities are possible to retrieve vibrational information from a sample. The first one is a spectroscopic approach; the goal is to measure the vibrational spectrum of the sample. The second is a microscopic approach; instead of probing the whole vibrational range, an image of the sample is acquired, based on vibrational contrast. In practice, the excitation has to probe one particular vibrational resonance in order to get a map of presence of the molecular bond responsible for the probed resonance. Those two modalities can be combined; this is hyperspectral imaging. Then, a stack of images is retrieved, and the vibrational spectrum can be recovered for each pixel in the image.

There are several ways of probing the vibrational spectrum of a sample. The range of vibrational resonance frequencies of molecular bonds lie in the 10–100 THz range, which corresponds to infrared wavelengths (3 – 30 μm). The direct measure of the absorption of infrared light by a material to investigate its vibrational spectrum falls into the field of infrared spectroscopy. The main drawback of using infrared light for imaging applications is the bad spatial resolution, which is proportional to the wavelength. One way to avoid working in the infrared range for vibrational spectroscopy is to use the effect discovered in 1928 by Nobel prize winner Chandrashekhara Venkata Râman [92, 93] and physicist Leonid Issaakovitch Mandelstam [94], that is know as the Raman effect.

4.1.1 Spontaneous Raman scattering

When sending visible or near-infrared light to a sample, two different scattering processes occur. Rayleigh scattering is an elastic process: the energy and momentum of scattered photons are preserved. A photon penetrating a medium

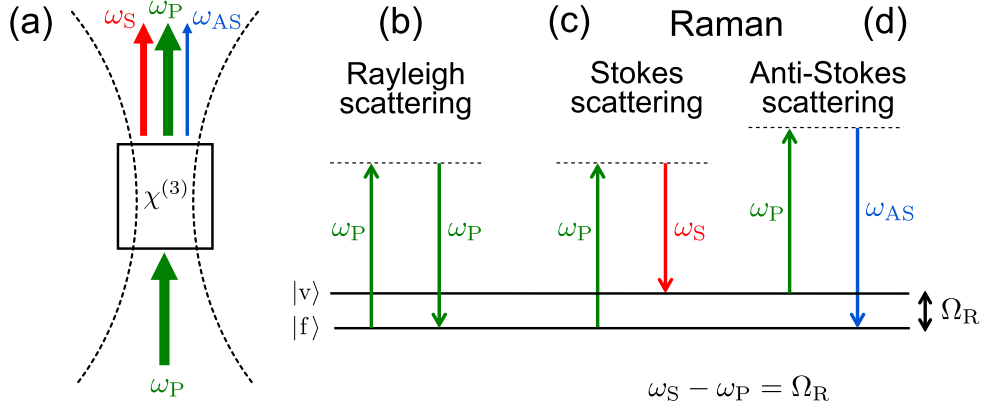


Figure 4.1: (a) Schematic view of Stokes and anti-Stokes radiations generation in a medium. $\chi^{(3)}$ is the third-order susceptibility of the medium (see Section 4.1.2). (b), (c) and (d) Rayleigh and Raman scattering energy diagrams. In the case of (b) Rayleigh scattering, the frequency does not change, whereas for Raman scattering, the light is either redshifted (Stokes scattering) or blueshifted (anti-Stokes scattering). (c) Stokes scattering: the pump photon interacts with a molecule in the fundamental state, and some of this energy is transferred to the molecule. In the end, the scattered Stokes photon is less energetic and the molecule is in an excited vibrational state. (d) Anti-Stokes scattering: the pump photon interacted with an already excited molecule, and the scattered anti-Stokes photon takes some of the vibrational energy of the molecule. As this process starts from the excited state, it is less probable, so the anti-Stokes radiation is less intense than the Stokes one. Both the Stokes and anti-Stokes fields carry with them the information about the energy of the vibrational level that was excited.

whose particles are much smaller than its wavelength will keep the same energy but its direction of propagation can change. In other words, the frequency of the light experiencing Rayleigh scattering is unchanged, but it is scattered in all directions.

On the contrary, Raman scattering is an inelastic process. The energy of the photon changes: there can occur either a energy transfer from the matter to the photon or from the photon to the matter. As a result, the photon can be redshifted or blueshifted. More specifically, if one considers a molecular bond with resonance frequency Ω_R , the frequency ω_P of the incoming photon can be changed to $\omega_P + \Omega_R$ (blueshifted) or $\omega_P - \Omega_R$ (redshifted). The redshifted radiation is called the Stokes (ω_S), whereas the blueshifted one is called the anti-Stokes (ω_{AS}). Those energy scheme of those two processes are compared

to each other and to the one of Rayleigh scattering in Fig. 4.1. In principle, Stokes scattering and anti-Stokes scattering have the same efficiency. In practice however, it is not the case. Due to Boltzmann distribution, the probability of a particle to be in a state of energy E is proportional to $\exp\left(\frac{-E}{k_B T}\right)$, where k_B is the Boltzmann constant and T is the temperature. At room temperature, all population is virtually in the fundamental level, because $k_B T$ is much smaller than one quantum of vibrational energy. From this level, no anti-Stokes process is possible. Therefore, intensity of anti-Stokes radiation is much smaller than the intensity of Stokes radiation. In fact, both Stokes and anti-Stokes scattering have a very low efficiency. The cross-section of spontaneous Raman is typically 14 orders of magnitude lower than the cross-section of fluorescence. Stimulated Raman schemes described in the next section are a way to improve the efficiency.

4.1.2 Coherent Raman scattering

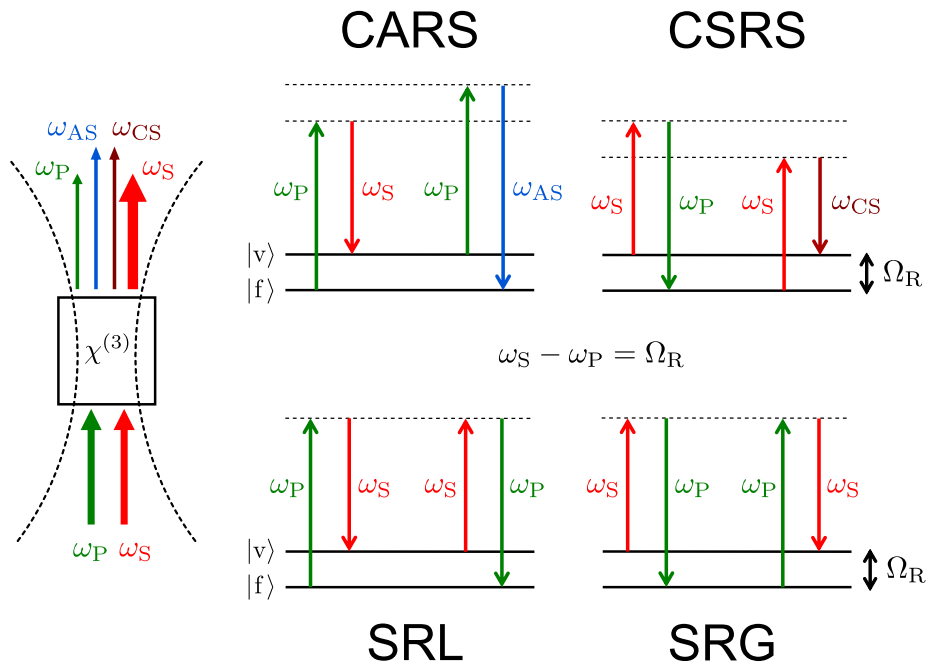


Figure 4.2: Energy diagrams of the four CRS processes.

In spontaneous Raman, one radiation is sent to the sample at ω_P to detect scattered radiations at $\omega_S = \omega_P - \Omega_R$ or $\omega_{AS} = \omega_P + \Omega_R$ in order to get information about the molecular vibration of resonance frequency Ω_R .

In coherent Raman scattering (CRS), two radiations are sent at two frequencies, called pump (ω_P) and Stokes (ω_S). Those two fields interfere, producing a

beating at frequency $\Omega = \omega_P - \omega_S$. If the beating frequency matches the resonance frequency of a molecular bond ($\Omega = \Omega_R$), the vibration of this particular bond is strongly enhanced compared to the other bonds vibrating in the sample. Moreover, if coherent light is sent to the sample, all the excited molecules in the excitation volume will vibrate in phase, which enhances the generation of scattered fields. The cross-sections of coherent Raman scattering are typically six orders of magnitude higher than the ones for spontaneous Raman scattering. Four processes can be considered, generating fields at frequencies:

- $\omega_P + \Omega_R = 2\omega_P - \omega_S = \omega_{AS}$,
- $\omega_P - \Omega_R = \omega_S$,
- $\omega_S + \Omega_R = \omega_P$,
- $\omega_S - \Omega_R = 2\omega_S - \omega_P = \omega_{CS}$.

The first process leads to the generation of an anti-Stokes radiation, it is called coherent anti-Stokes Raman scattering (CARS). The second and third processes generate fields that interfere with the incident fields, they are respectively called stimulated Raman gain (SRG) and stimulated Raman loss (SRL) and are grouped under the common name stimulated Raman scattering (SRS). The last process is called coherent Stokes Raman scattering (CSRS), but as the frequency it generates is redshifted with respect to the excitation fields, its detection can be made difficult because (i) it lies in the near-infrared where detectors are less sensitive and (ii) there might be fluorescence from one or both of the fields in the same spectral region, so this will not be discussed further.

CRS can be implemented in spectroscopic mode, by changing the frequency of one of the two exciting beams. Then the probed frequency $\Omega = \omega_P - \omega_S$ scans the vibrational spectrum of the molecule.

CRS can also be used in microscopy, by tuning the frequencies of the pump and Stokes beams so that their difference matches the resonance frequency of a targeted molecular bond. The observed signal then comes from the vibration of this molecular bond, creating a map of the sample that highlights the regions where this molecular bond is present. Quantitative aspects and possible artifacts of CARS and SRS will be addressed later on.

Coherent anti-Stokes Raman scattering

Like in Section 1.2.1, the propagation equation can be obtained from Maxwell's equations. The difference with the calculation presented earlier is that here, the nonlinear polarization is not treated in a perturbative manner. The Helmholtz equation (Eq. 1.8) then becomes:

$$\frac{\partial^2 \tilde{E}(z, \omega)}{\partial z^2} + \frac{n^2 \omega^2}{c^2} \tilde{E}(z, \omega) = -\frac{\omega^2}{\varepsilon_0 c^2} P_{NL}(z, \omega). \quad (4.1)$$

Once again, with the slowly-varying envelope approximation, the second derivative coming from the development of the Laplacian operator can be neglected. The anti-Stokes field in the time domain is written: $E_{AS}(z, \omega) = A_{AS}e^{i(k_{AS}z - \omega_{AS}t)} + c.c.$. In the frequency domain, under the monochromatic approximation, this translates to:

$$\frac{\partial^2 \tilde{E}_{AS}(z, t)}{\partial z^2} \approx \left(2ik_{AS} \frac{\partial A_{AS}}{\partial z} - k_{AS}^2 A_{AS} \right) e^{ik_{AS}z}. \quad (4.2)$$

A_{AS} is the integral of the delta function of the anti-Stokes field, considered quasi-monochromatic and, with Eq. 4.1:

$$\frac{\partial A_{AS}}{\partial z} = \frac{i\omega}{2n\varepsilon_0 c} P_{AS}(\omega) e^{ik_{AS}z}. \quad (4.3)$$

The nonlinear polarization associated with CARS is written [95]:

$$\mathbf{P}_{AS}(\omega_{AS}) = \varepsilon_0 \chi^{(3)}(-\omega_{AS} : \omega_P, -\omega_S, \omega_P) \mathbf{E}_P(\omega_P) : \mathbf{E}_S^*(\omega_S) : \mathbf{E}_P(\omega_P), \quad (4.4)$$

We consider a propagation along the z direction, with all the fields linearly polarized in the same direction. The pump and Stokes beams are respectively written $E_P = A_P e^{i(k_P z - \omega_P t)} + c.c.$ and $E_S = A_S e^{i(k_S z - \omega_S t)} + c.c.$. With this, Eq. 4.4 becomes:

$$P_{AS}(\omega_{AS}) = 3\varepsilon_0 \chi_{AS}^{(3)}(\omega_{AS}) A_P^2 A_S^* e^{-ik_{AS}z}, \quad (4.5)$$

where $\chi_{AS}^{(3)} = 2\chi_{xyyy}^{(3)}$. Then:

$$\frac{\partial A_{AS}}{\partial z} = \frac{3i\omega_{AS}}{2n\varepsilon_0 c} A_P^2 A_S^* e^{-i\Delta k z}, \quad (4.6)$$

with $\Delta k = \Delta \vec{k} \cdot \vec{e}_z = (2\vec{k}_P - \vec{k}_S - \vec{k}_{AS}) \cdot \vec{e}_z$, and the anti-Stokes intensity is:

$$I_{AS}(L) \approx |\chi^{(3)}(\omega_{AS})|^2 L^2 \text{sinc}^2 \left(\frac{\Delta k L}{2} \right) I_P^2 I_S, \quad (4.7)$$

L being the length of the material. The CARS signal is maximum for $\Delta \vec{k} = \vec{0}$, this is the phase-matching condition. In microspectroscopy and in microscopy, the phase-matching condition is relaxed by using high numerical aperture objective so that many \vec{k} are available and the CARS signal is efficiently generated, as suggested by Zumbusch and co-workers in 1999 [96]. Equation 4.7 shows that the CARS signal varies quadratically with the pump intensity and linearly with the Stokes intensity.

The $\chi^{(3)}$ tensor represents the response from the material. It consists in two parts, a resonant and a non-resonant one:

$$\chi^{(3)} = \chi_R^{(3)} + \chi_{NR}^{(3)}. \quad (4.8)$$

The resonant contribution is the one that was already discussed in the previous section. The molecule is excited to a vibrational state by a pair of photons (pump/Stokes), then this vibrational excited state is probed by another pump photon, and an anti-Stokes photon is generated. However, photons at the same anti-Stokes frequency can be generated by another pathway that does not depend on the vibrational states of the molecule (see Fig. 4.3). The resonant CARS is strongly enhanced when the difference between pump and Stokes matches a vibrational frequency of the molecule. On the contrary, non-resonant signal will be generated for any combination of pump and Stokes frequencies. Although several groups have found ways to take advantage of it, the non-resonant background is often seen as a drawback. For example, in an imaging configuration where one wants to locate a targeted compound in a sample, there will be non-resonant signal even in places where the compound is absent.

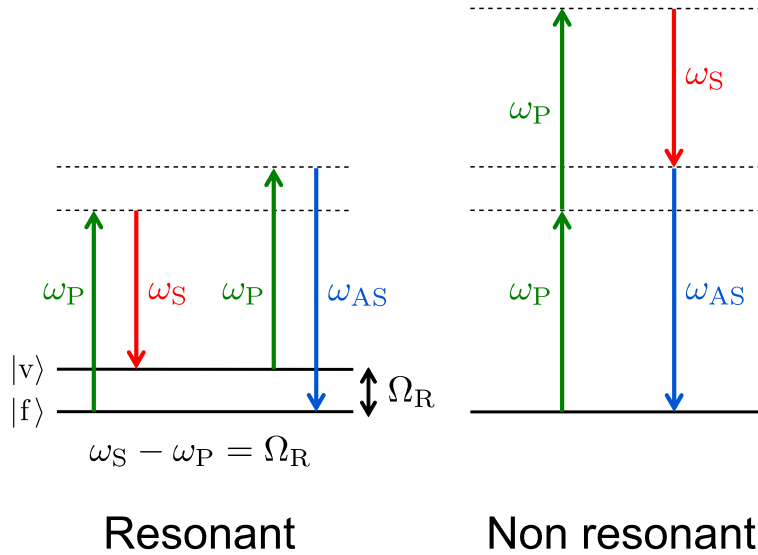


Figure 4.3: Energy diagrams for the resonant and non resonant contributions to the CARS signal.

With Eqs. 4.7 and 4.8:

$$I_{AS}(L) \propto \left| \chi_R^{(3)} + \chi_{NR}^{(3)} \right|^2 \quad (4.9)$$

$$\propto \left| \chi_R^{(3)} \right|^2 + \left| \chi_{NR}^{(3)} \right|^2 + 2\chi_{NR}^{(3)} \text{Re} \left[\chi_R^{(3)} \right]. \quad (4.10)$$

The resonant term $\chi_R^{(3)}$ contains the spectral information about the molecular vibration. It can be related to the number of scatterers per unit volume N in the following way:

$$\chi_R^{(3)} = \frac{N \cdot A}{\Omega - (\omega_P - \omega_P) - i\Gamma} \quad (4.11)$$

where A , Ω , and Γ are the amplitude, angular frequency, and line width of the vibrational mode. $\chi_{\text{NR}}^{(3)}$ only depends on the non resonant signal. It is spectrally flat because it is instantaneous in the time-domain, so the non resonant background is assumed to be constant over the investigated range of vibrational frequencies. The last term in Eq. 4.11 is a crossed term that results from the interference between the resonant and the non resonant signal. One of the main effect of this term is the spectral distortion of the CARS spectrum compared to the Raman spectrum.

Due to the non resonant contribution, the signal is not proportional to the concentration. If the resonance is strong, the first term is much larger than the others and the dependence is nearly quadratic [97].

Stimulated Raman scattering

As already stated in previous paragraphs, the interaction of two excitation fields whose frequency difference $\omega_{\text{P}} - \omega_{\text{S}}$ matches the resonance frequency Ω_{R} of a molecular vibration generates four fields at ω_{P} , ω_{S} , $\omega_{\text{P}} + \Omega_{\text{R}}$ and $\omega_{\text{S}} - \Omega_{\text{R}}$. For the two last processes, it is easy to separate the generated fields from the exciting fields as they do not have the same frequencies. However, the two generated fields at ω_{P} and ω_{S} interfere with the exciting fields, and the observable signal is the result of the interference.

By writing the equation for the nonlinear polarization density of the material upon excitation by pump and Stokes radiation, one can get the expression for the polarization density at the two frequencies of interest.

The polarization density of the medium at ω_{P} and ω_{S} are written

$$P(\omega_{\text{P}}) = 6\varepsilon_0\chi_{\text{R}}^{(3)}(\omega_{\text{P}})|A_{\text{S}}|^2A_{\text{P}}e^{i(k_{\text{P}}z)} \quad (4.12)$$

$$P(\omega_{\text{S}}) = 6\varepsilon_0\chi_{\text{R}}^{(3)}(\omega_{\text{S}})|A_{\text{P}}|^2A_{\text{S}}e^{i(k_{\text{S}}z)}, \quad (4.13)$$

with $\chi_{\text{R}}^{(3)}(\omega_{\text{P}}) = \chi_{\text{R}}^{(3)}(\omega_{\text{S}})^*$. From these equations, one can calculate the fields $E_{\text{P}}^{(3)}$ and $E_{\text{S}}^{(3)}$ that are generated and interfere with the exciting fields, with $E_{\text{P}}^{(3)} = A_{\text{P}}^{(3)}e^{i(k_{\text{P}}z - \omega_{\text{P}}t)} + c.c.$ and $E_{\text{S}}^{(3)} = A_{\text{S}}^{(3)}e^{i(k_{\text{S}}z - \omega_{\text{S}}t)} + c.c.$. The intensities at the two frequencies of interest are then:

$$I_{\text{P}} \propto |A_{\text{P}}|^2 - 2|A_{\text{P}}A_{\text{P}}^{(3)}| \quad (4.14)$$

$$I_{\text{S}} \propto |A_{\text{S}}|^2 + 2|A_{\text{S}}A_{\text{S}}^{(3)}| \quad (4.15)$$

The pump field experiences a depletion, while the Stokes field experiences a gain. This is why the two process are respectively called stimulated Raman loss (SRL) and stimulated Raman gain (SRG).

4.2 Spectral focusing

4.2.1 Spectral resolution

As explained in Section 1.2.2, there is a relationship linking the duration and the bandwidth of unchirped Gaussian and sech-squared pulses. Let us rewrite the time-bandwidth product that defines this relationship: $\Delta t \Delta f = C_{\text{TBP}}$, where $C_{\text{TBP}} = 2 \ln 2 / \pi \approx 0.441$ for Gaussian pulses and $C_{\text{TBP}} = 4 (\ln(1 + \sqrt{2}))^2 / \pi^2 \approx 0.315$ for sech-squared pulses. In the field of Raman spectroscopy, it is common to use wavenumbers ($\bar{\nu}$, expressed in inverse centimeters) instead of frequencies. The time-bandwidth product can be re-written this way:

$$\Delta \bar{\nu} = C_{\text{TBP}} \frac{1}{c \Delta t}. \quad (4.16)$$

Figure 4.4 shows the time-bandwidth dependence for Gaussian and sech-squared Fourier-transform-limited pulses.

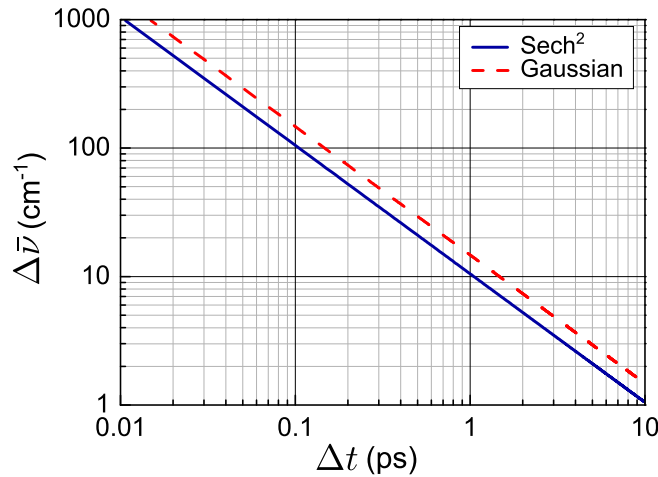


Figure 4.4: Optical bandwidth of Fourier-transform pulses with durations from 10 fs to 10 ps, for Gaussian and sech-squared shapes.

The Ti:Sapphire lasers that were used in the frame of this work deliver sech-squared shaped pulses. This is also the typical pulse shape of solitons. Then, the bandwidth for a 100-fs long pulse is about 100 cm^{-1} , while it is about 10 cm^{-1} for a 1-ps long pulse.

In Raman spectroscopy schemes, the vibrational resonances are probed by the beating between the pump and Stokes frequencies. The bandwidth of the exciting pulses therefore define the spectral resolution of the measured Raman spectrum. The typical width of vibrational resonances is about $5\text{--}10 \text{ cm}^{-1}$. It can be intuitively understood that in order to resolve the Raman lines, one

should work with picosecond pulses so that the optical bandwidth matches the width of the probed Raman lines.

One of the most used schemes for CRS indeed relies on ps/ps excitation at 80 MHz, because it provides high spectral resolution without degrading the sensitivity [98]. However, several schemes have been developed to take advantage of the properties of fs pulses while preserving spectral resolution. For example, multiplex CARS uses a ps pulse train as pump and a fs supercontinuum generated in a fiber as Stokes to probe a broad spectral range in a single shot. In single-beam CARS, a pulse shaper is used to periodically modulate the spectral phase of a broadband fs pulse to target a specific molecular vibration. The spectrum is then recovered by changing the period of the phase modulation and Fourier-transforming the intensity signal [99]. The methods briefly presented above are rather complex ways to use fs pulses for CRS spectroscopy. There is a simple way to obtain spectral selectivity equivalent to the one of a ps/ps system from a fs/fs source, it is called spectral focusing.

4.2.2 Principle of spectral focusing

The principle of spectral focusing is shown in Fig. 4.5. The two exciting fs pulses are equally chirped through propagation in a dispersive system [100]. The group-delay dispersion then induced by such a system can be positive, for example when the pulses travel in pieces of glass; or negative, for example by using gratings or prisms pair in a double-pass configuration. This way, the instantaneous frequency difference is the same over the whole overlap of the two pulses and the instantaneous spectral width is much smaller than in the transform-limited case. Therefore, the spectral resolution is dramatically increased compared to the initial fs/fs configuration. The spectral resolution is then defined by the chirp of the pulses: the more chirped the pulses are, the higher the spectral resolution will be. It is then possible to optimize the chirp of the pulses to match the spectral width of the targeted Raman line [101]. However, the increase of spectral resolution by chirping the pulses comes at the price of decreased peak power, so there has to be a trade off between peak power and spectral resolution. Typically, 100-fs long pulses chirped to a few picoseconds are a good compromise. Spectral focusing also brings an additional feature to the CRS setup: by changing the delay of one of the pulses, the instantaneous frequency difference is changed. A small spectral scanning can then be performed within the spectral bandwidth of the pulses.

As previously stated, the spectral resolution $\delta\bar{\nu}$ depends on the duration of the chirped pulses at the sample plane Δt_P (pump) and Δt_S (Stokes), whereas the scanning range of the system $\delta\bar{\nu}$ depends on the duration of the FTL pulses $\Delta t_{P,FTL}$ and $\Delta t_{S,FTL}$. Andresen and co-workers showed that spectral focusing with fs pulses gives the same signal as classical CRS with ps pulses for identical

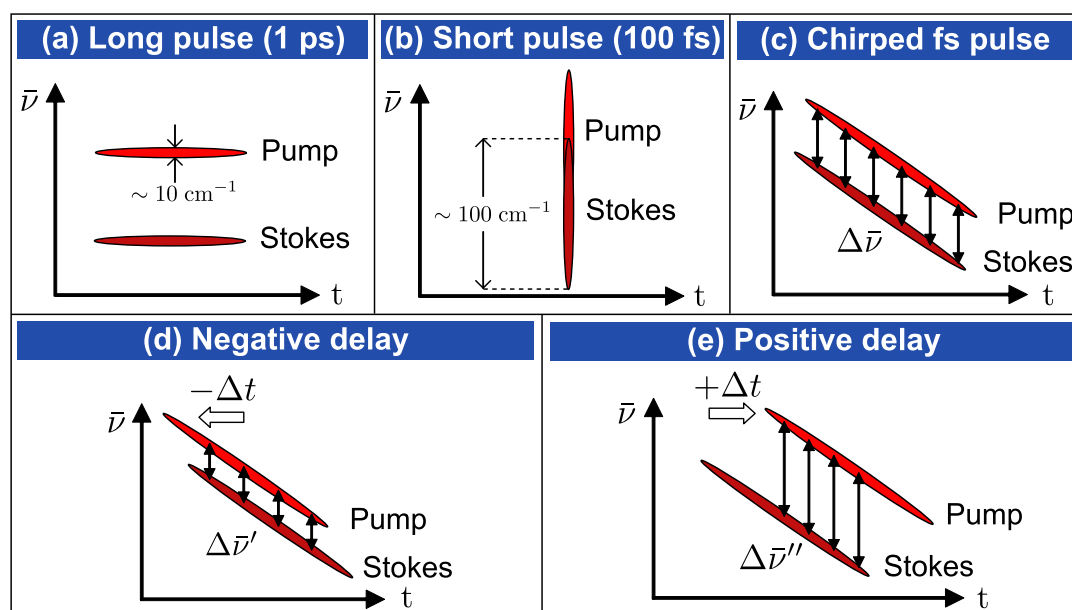


Figure 4.5: Comparison of the optical bandwidths and spectral resolutions in a CRS setup using as pump and Stokes (a) two unchirped picosecond pulses; (b) two unchirped femtosecond pulses; and (c) two chirped femtosecond pulses. (d) and (e): Principle of spectral focusing. By moving a delay line with a motorized translation stage, the instantaneous frequency difference between pump and Stokes beams scans the range of targeted vibrational frequencies.

temporal envelopes [102]. As a first approximation:

$$\delta\bar{\nu} = \frac{0.315}{c} \sqrt{\frac{1}{(\Delta t_P)^2} + \frac{1}{(\Delta t_S)^2}} \quad (4.17)$$

$$\Delta\bar{\nu} = \frac{0.315}{c} \sqrt{\frac{1}{(\Delta t_{P,FTL})^2} + \frac{1}{(\Delta t_{S,FTL})^2}}. \quad (4.18)$$

4.2.3 Chirping femtosecond pulses

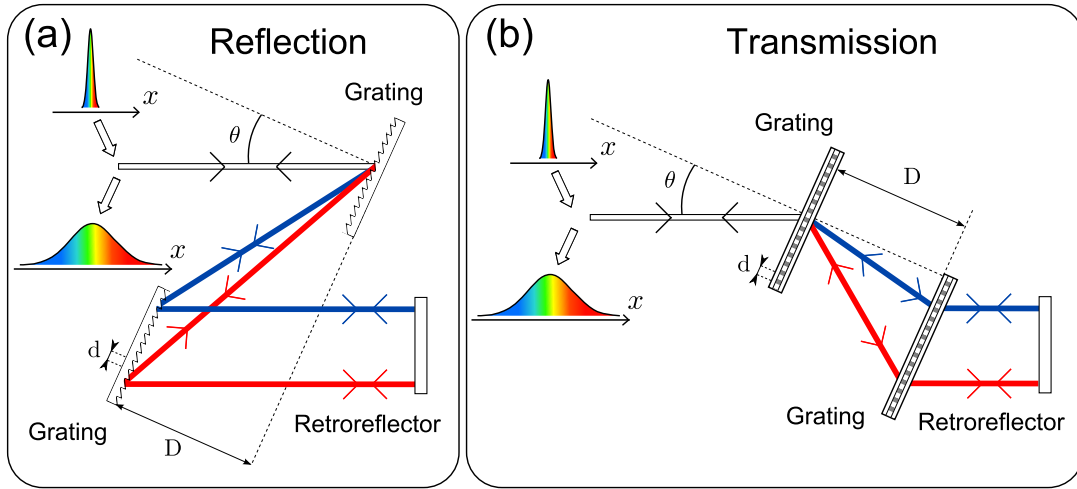


Figure 4.6: (a) Reflection grating pair. (b) Transmission grating pair.

At optical frequencies, the refractive index of most materials decreases with increasing wavelength. It means that when a pulse of light propagates in such a medium, the leading edge of the pulse contains the most red wavelengths, whereas the trailing edge of the pulse contains the most blue ones.

In a grating pair, the diffraction of the light associated with the geometry of the system allows the reverse situation to happen. Indeed, the blue part of the pulse has a shorter optical path than its red part (see Fig. 4.6). The group-delay dispersion induced when a pulse of light passes through a grating pair is written [103]:

$$\Phi^{(2)} = \frac{d^2\phi}{d\omega^2} = -\frac{4\pi^2 cD}{\omega^3 d^2 \cos^3(\theta)} = -\frac{\lambda^3 D}{2\pi c^2 d^2 \cos^3(\theta)}, \quad (4.19)$$

where $\phi(\omega)$ is the phase of the wave, λ is the central wavelength of the pulse and ω is the angular frequency defined by $\omega = 2\pi c/\lambda$, D is the distance between the two gratings, d is the groove spacing of the gratings (or pitch) and $d\theta$ is the diffraction angle as shown in Fig. 4.6. This formula is valid for reflection gratings as well as for transmission gratings.

After the first pass in the grating pair, the pulse is negatively chirped in time, but the spectral components are also spatially dispersed. The light is sent back to the grating pair by the means of a retro-reflector to cancel this effect. As a result, the final group-delay dispersion added to the pulse by the system is doubled:

$$\Phi_{2\text{ pass}}^{(2)} = -\frac{\lambda^3 D}{\pi c^2 d^2 \cos^3(\theta)}. \quad (4.20)$$

Figure 4.7 presents the principle of the light source that is proposed for CRS. The pump and Stokes beams are generated from the same fs laser. This makes the setup more compact and less complex because no electronic synchronization is required between the two pulse trains. Then, the Stokes wavelength is created via soliton generation and soliton self-frequency shift. Then pump and Stokes pulses are chirped in two separate grating pairs before they are recombined on a dichroic filter, spatially and temporally overlapped and sent to the sample. The spectral scan is obtained by moving a delay line mounted on a motorized translation stage.

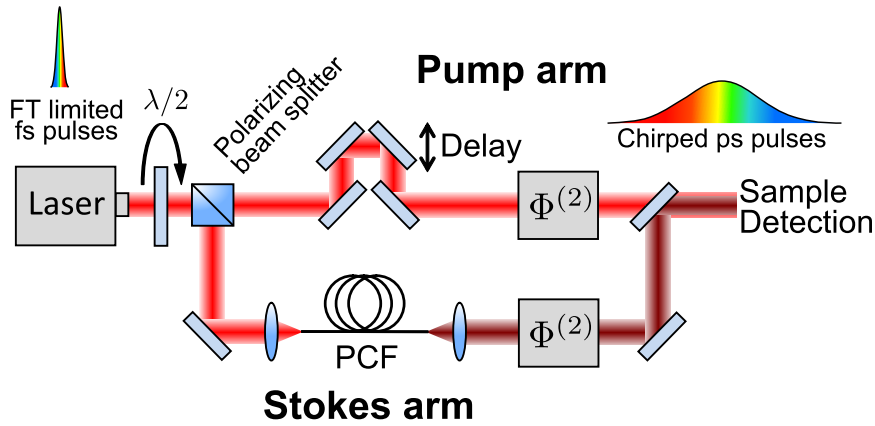


Figure 4.7: Principle of the CRS setup.

Previous works report spectral focusing setups with positively chirped pulses using pieces of glass (see e.g. [104–106]), or negatively chirped pulses using prism pairs or grating pairs (see e.g. [107]). In principle, negative or positive chirp can be used for spectral focusing, although Andresen and co-workers suggested that negative chirp could partially cancel time jitter effects [108]. In this work, grating pairs were used to chirp the pulse, as they have several advantages over pieces of glass.

First, the dispersion induced by the gratings can be much bigger than the one induced by glass over the same distance. For example, two gratings with 600 lines per mm ($d = 1/1200$ mm), separated by $D = 5$ cm will add a group-delay dispersion of 130,000 fs² to a 800 nm pulse impinging on the surface of

the first grating at normal incidence ($\theta = 0$). For comparison, 5 cm of SF57 glass adds 11,000 fs² GDD to the same 800 nm pulse. Consequently, a much more compact system can be obtained with grating pairs for the same amount of induced group-delay dispersion.

A second point is the flexibility allowed by such a system. By slightly changing the distance between the gratings, the group-delay dispersion can be modified in order to adjust the chirp of the pulse. This is convenient for the fine adjustment of the two chirps that has to be perfectly equal on the two pulses in order to get maximum spectral selectivity. Moreover, the amount of group-delay dispersion needed to chirp a pulse is wavelength-dependent. In the spectral focusing scheme, the investigated spectral range is limited by the bandwidth and duration of the chirped pulses. However, it is rather easy to change this range by modifying the soliton wavelength. In this case, the GDD induced by the grating pair on the Stokes pulse has to be adjusted to recover the same chirp as the one induced on the pump pulse. For example, if the soliton is set to be centered around 870 nm, the range of accessible probed vibrational wavenumbers is about 750 – 1150 cm⁻¹. Other spectral regions can be reached by changing the soliton redshift via a change of input power in the PCF and adapting the inter-grating distance to the new wavelength on the Stokes arm.

The major drawback to using this system for chirping the pulses is the power losses caused by the higher order diffraction on the gratings. For classical blazed reflection gratings, the losses go up to 30 % per reflection, then the total power loss for the 4 reflections amounts to about 75 %. This can be reduced by using transmission gratings. Then the losses can be as low as a few percents per transmission, which can result in a total loss of 10 – 20 % for 4 transmissions.

For Gaussian pulses, it is easy to calculate the FWHM duration of the pulse after it passes through the grating pairs:

$$\Delta t = \Delta t_{\text{FTL}} \sqrt{1 + \left(\frac{4 \ln(2) \Phi^{(2)}}{\Delta t_{\text{FTL}}^2} \right)^2}, \quad (4.21)$$

where Δt_{FTL} is the Fourier-transform-limited duration of the pulse. For large chirps, the duration tends to vary linearly with the added GDD. It is interesting to notice the $1/\Delta t_{\text{FTL}}$ dependence of the duration of the chirped pulse. The shortest the FTL duration of the pulse is, the strongest the effect of the GDD will be (see Fig. 4.8). This means that very short pulses are very sensitive to GDD: they are easier to chirp and they result in longer final pulses. This means that if the pulse is very short, the small GDD induced by the optics (e.g. lenses, objectives) start to play an important role and have to be taken into account in the calculation of the pulse duration at the sample plane.

For sech-squared pulses, the calculation can be numerically done in the fol-

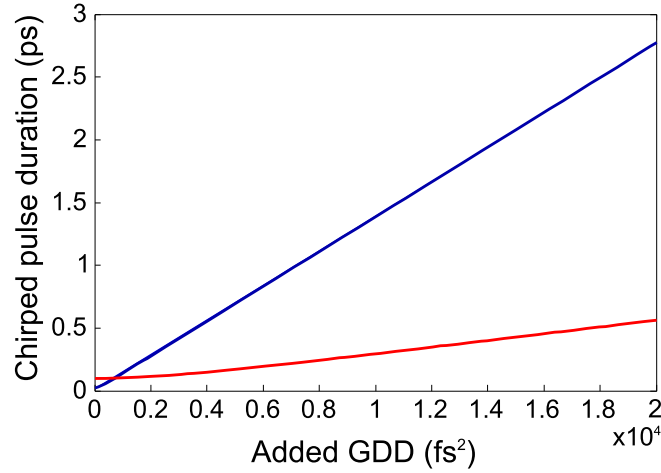


Figure 4.8: Calculated duration of pulses as a function of the GDD they experienced, for two 800 nm pulses of 2 different Fourier-transform-limited durations: 20 fs (blue line) and 100 fs (red line).

lowing way:

$$E(t) = E(0) \operatorname{sech} \left(2 \ln(1 + \sqrt{2}) \frac{t}{\Delta t_{\text{FT}}} \right) \quad (4.22)$$

$$\tilde{E}(\omega) = \text{FT}[E(t)] = \tilde{E}(0) \operatorname{sech} \left(\frac{\Delta t_{\text{FT}}}{2 \ln(1 + \sqrt{2})} \frac{\pi}{2} \omega \right) \quad (4.23)$$

$$\tilde{E}_{\text{chirped}}(\omega) = \tilde{E}(0) \operatorname{sech} \left(\frac{\Delta t_{\text{FT}}}{2 \ln(1 + \sqrt{2})} \frac{\pi}{2} \omega \right) \exp \left(i \frac{\Phi^{(2)}}{2} \omega^2 \right) \quad (4.24)$$

$$E_{\text{chirped}}(t) = \text{IFT}[\tilde{E}_{\text{chirped}}(\omega)] \quad (4.25)$$

$$(4.26)$$

Then it is easy to compute the FWHM duration from the calculated chirped pulse intensity. This calculation can also be done for Gaussian pulse, or any other pulse shape, and gives the same results as the analytical formula.

4.3 Experimental setup

The two pulses required for CARS and SRS are generated from the same Ti:Sapphire laser. Two lasers were successively used: the GigaJet20 from LaserQuantum (1 GHz, 30 fs, 803 nm) pumped by a 532 nm, 10 W continuous laser (Coherent Verdi-V10); and Chameleon from Coherent Inc. (80 MHz, 150 fs, tunable from 680 to 1080 nm), used at 800 nm. Both lasers deliver sech-square-shaped pulses which are well suited to the soliton formation in the fiber, because of

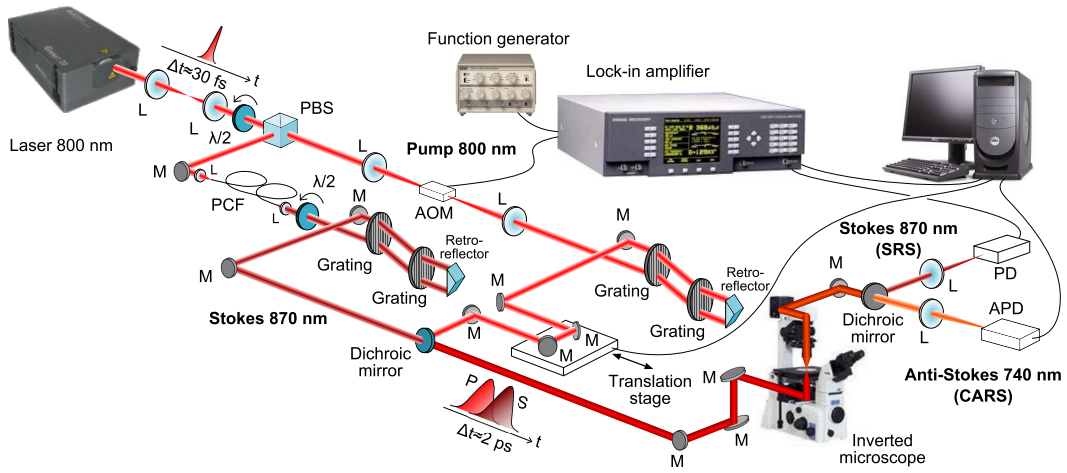


Figure 4.9: Detailed scheme of the optical setup. PBS: polarizing beam splitter, PCF: photonic crystal fiber, AOM: acousto-optic modulator.

the inherent sech-squared shape of solitons. A half-wave plate and a polarizing beam splitter separate the pump and Stokes beams and allow to tune the wavelength of the soliton. It has to be noted that the SC-PBG fiber presented in Section 2.3 was not used in this part of the work. The PCF that was used instead has a $1.5 \mu\text{m}$ solid core and shows anomalous group-velocity dispersion (GVD) between 600 nm and 2000 nm, which covers the wavelength range of interest (800 – 1000 nm). The pulses are chirped independently from each other, with two pairs of either reflection or transmission gratings. After recombination on a dichroic mirror, the beams are directed to an inverted microscope (Nikon Eclipse TiU) where the light is focused on the sample by a 0.45 NA objective (Olympus) and the signal is collected in the forward direction by a 0.6 NA objective (Olympus). The pump and Stokes beams have been optimized so that they reach high power levels at the sample plane, respectively 50 mW and 10 mW. The CARS signal at the AS frequency is spectrally filtered and focused onto an avalanche photodiode (Perkin Elmer SPCM) for detection. For the SRS mode, the pump beam is modulated by an acousto-optic modulator (AA Opto Electronic) driven by a function generator operating at 1 MHz, the Stokes beam is sent to a photodiode (DET10A Thorlabs), and a lock-in amplifier (Signal Recovery) extracts the SRS signal at the modulation frequency. Thanks to a set of filters and a parallel detection scheme via a National Instruments acquisition board (NI USB-6351), CARS and SRS measurement pathways can operate simultaneously. A detailed scheme of the setup is presented in Fig. 4.9.

4.4 Characterization on chlorobenzene

In order to characterize the optical setup, a series of experiments was performed on liquid chlorobenzene, which is known for its strong Raman lines in the targeted spectral range ($950 - 1200 \text{ cm}^{-1}$). For comparison purposes, the spontaneous Raman spectrum of chlorobenzene in this region was first measured with a standard Raman spectrometer. The spectrum is shown in Fig. 4.10.

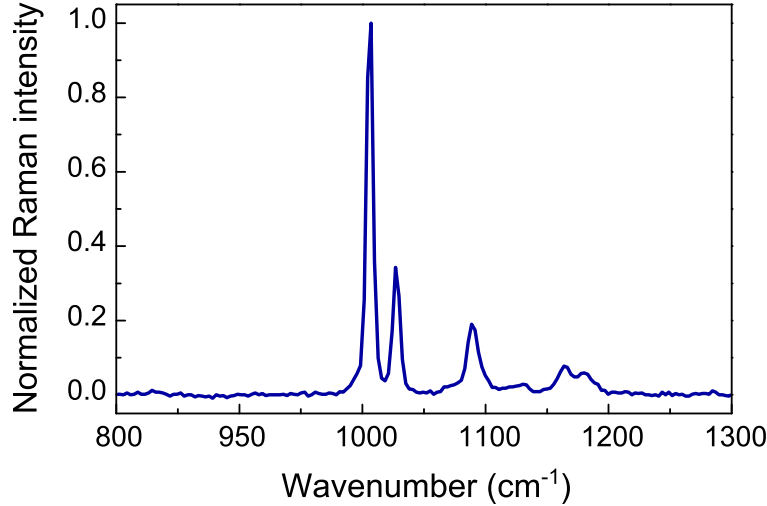


Figure 4.10: Raman spectrum of chlorobenzene.

Several Raman lines can be identified, they can be assigned to vibrational modes of chlorobenzene [109]. The strongest line at 1007 cm^{-1} can be assigned to a ring vibration mode (or in plane bending β -CCC). The lines at 1027 , 1159 and 1175 cm^{-1} can all be assigned to in plane C-H bending modes (β -CH). The 1187 cm^{-1} line is assigned to a C-Cl stretching mode.

The setup was first used with the Chameleon laser and reflection gratings. The pulses of the laser have a narrow spectrum: $\Delta\lambda_P = 6 \text{ nm}$, which corresponds to a Fourier transform-limited (FTL) pulse duration $\Delta t_{P,FTL} = 157 \text{ fs}$. The soliton is inherently Fourier transform-limited at the output of the fiber ($\Delta\lambda_S = 11 \text{ nm}$, $\Delta t_{S,FTL} = 73 \text{ fs}$ at 872 nm). The GDD added to both pulses by the grating pairs was carefully set by adjusting the inter-grating distance in order to compensate for the different positive GDD added by the optics on both pathways. This was first done by roughly estimating the required inter-grating distance with Eq. 4.20. The fine adjustment was then found by acquiring spectra and changing the position of one grating to obtain the narrowest lines in the spectrum. Finally, the total GDD applied on pump and Stokes pulses was estimated to be $\Phi^{(2)} = -45,000 \text{ fs}^2$, stretching them in time to $\Delta t_P = 1.2 \text{ ps}$ and $\Delta t_S = 0.67 \text{ ps}$, respectively. With Eqs. 4.17 and 4.18, the spectral resolution

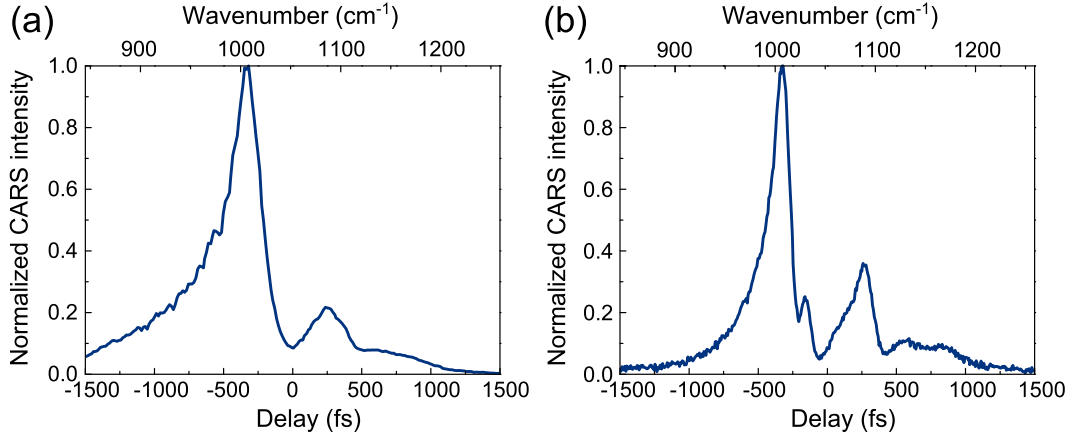


Figure 4.11: (a) CARS spectrum of chlorobenzene acquired with the Chameleon laser (80 MHz) and the reflection gratings (average of 8 scans). Pump: 800 nm, 15 mW , Stokes: 872 nm, 0.3 mW. (b) CARS spectrum of chlorobenzene acquired with the GigaJet20 laser (1 GHz) and the transmission gratings (average of 2 scans). Pump: 800 nm, 50 mW , Stokes: 872 nm, 10 mW.

and the scanning range are estimated to be $\delta\bar{\nu} = 18 \text{ cm}^{-1}$ and $\Delta\bar{\nu} = 160 \text{ cm}^{-1}$.

A CARS spectrum of chlorobenzene acquired in this configuration is shown in Fig. 4.11(a). The spectral resolution is not good enough to resolve the 1007 and 1027 cm^{-1} . This is because the pulses are not stretched to a long enough duration. As the Fourier-transform-limited duration is rather high, especially for the pump beam, more added GDD is required to significantly chirp the pulses (see Fig. 4.8). More GDD could be added by increasing the inter-grating distances, however it was decided not to try this option because the peak power of the Stokes beam and the signal were already low in this configuration.

Instead, the Chameleon laser is replaced by the GigaJet20 laser. Its higher bandwidth $\Delta\lambda_P = 25 \text{ nm}$ corresponds to a shorter Fourier transform-limited pulse duration ($\Delta t_{P,\text{FTL}} = 27 \text{ fs}$). The soliton generated in the fiber has also a broader spectrum and a shorter Fourier-transform-limited duration ($\Delta\lambda_S = 18 \text{ nm}$, $\Delta t_{S,\text{FTL}} = 47 \text{ fs}$ at 872 nm). The reflection gratings have been replaced by transmission gratings to reduce the losses to 14 % per transmission, which results in a loss of 45 % for 4 transmissions. This is still a high power loss, and it is the price to pay for compactness and flexibility. By applying a total GDD of $\Phi^{(2)} = -37,600 \text{ fs}^2$, the pulses are stretched in time to $\Delta t_P = 1.6 \text{ ps}$ and $\Delta t_S = 2.8 \text{ ps}$, respectively. As expected, the spectral resolution and the scanning range are improved and estimated to be $\delta\bar{\nu} = 8 \text{ cm}^{-1}$ and $\Delta\bar{\nu} = 450 \text{ cm}^{-1}$. The GHz repetition rate results in higher average power, so the total CARS signal is overall higher. Figure 4.11(b) shows a spectrum acquired in the new

configuration. It indeed shows an improved resolution, although it is not as good as the predicted one because the spectrum is strongly distorted by the nonresonant background.

The power dependence of CARS and SRS signals were measured to verify the agreement of the experiment with the theory. Eqs. 4.27 and 4.28 recall the expressions of CARS and SRS intensities versus the incoming pump (I_P) and Stokes (I_S) intensities ($\chi^{(3)}$ being the nonlinear susceptibility).

$$I_{\text{CARS}} \propto |\chi^{(3)}|^2 I_P^2 I_S \quad (4.27)$$

$$I_{\text{SRS}} \propto \text{Im}(\chi^{(3)}) I_P I_S \quad (4.28)$$

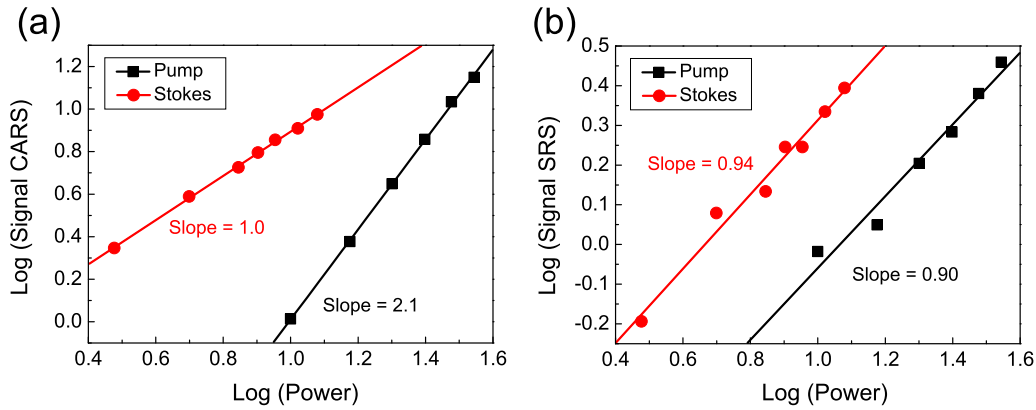


Figure 4.12: Dependence of (a) CARS and (b) SRS signal on pump power (black squares) and Stokes power (red circles). The lines are the linear fits of the experimental data. The measurements were done on the 1007 cm^{-1} Raman line of chlorobenzene. (a) Decimal logarithm of the CARS signal (in 10^5 cps) divided by 10^5 cps versus decimal logarithm of the pump and Stokes power (in mW) divided by 1 mW. The slopes of the linear fits shows the linear dependence of CARS signal with Stokes power and its quadratic dependence with pump power. (b) Decimal logarithm of the SRS signal (in μV) divided by $1 \mu\text{V}$ versus decimal logarithm of the pump and Stokes power (in mW) divided by 1 mW. The slopes of the linear fits shows the linear dependence of SRS signal with Stokes and pump powers.

In Fig. 4.12 are plotted the logarithm of CARS and SRS signals against the logarithm of pump and Stokes powers, measured with the CRS light source tuned to the 1007 cm^{-1} line of chlorobenzene. The slope of the linear fit of the data match with what is expected from the theory. CARS signal is quadratic with I_P and linear with I_S while SRS is linear with I_P and I_S .

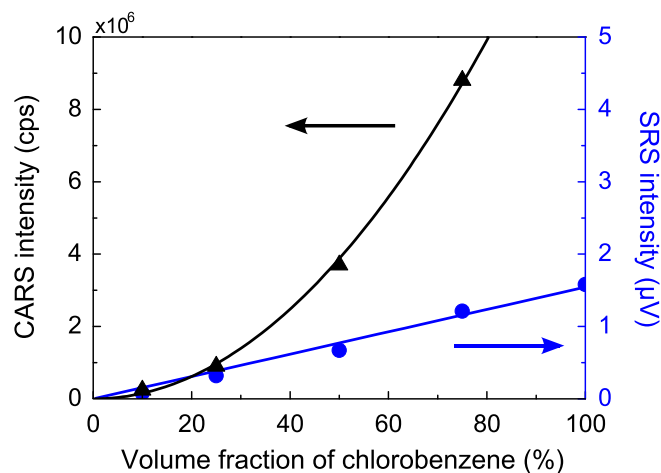


Figure 4.13: Dependence of CARS signal (black triangles) and SRS signal (blue circles) on concentration of chlorobenzene diluted in chloroform. The measurements were done on the 1007 cm^{-1} Raman line of chlorobenzene. Black line: quadratic fit of CARS data points. Blue line: linear fit of SRS data points.

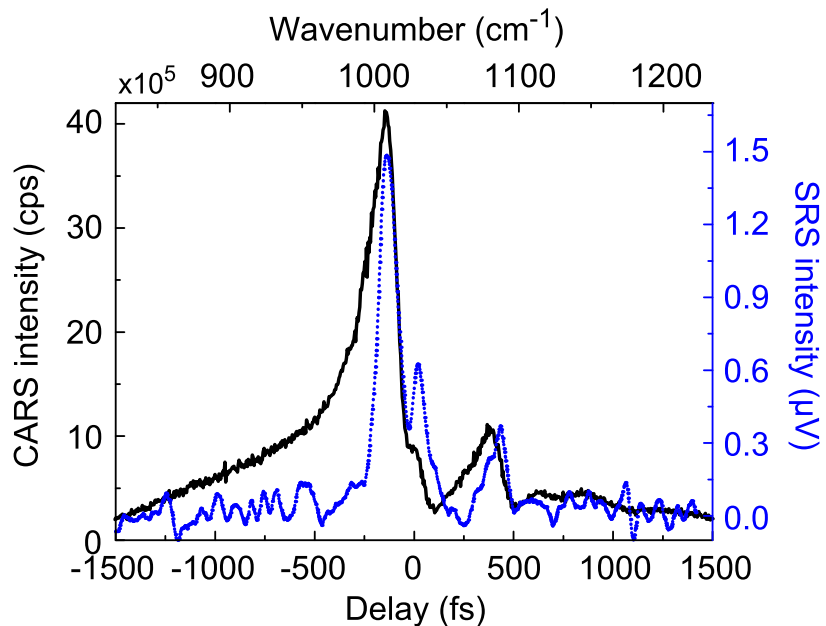


Figure 4.14: CARS (solid black line) and SRS (dotted blue line) spectra of liquid chlorobenzene.

Figure 4.13(b) shows CARS and SRS signal dependencies with concentration for a mixture of chlorobenzene in chloroform. While SRS shows a linear evolution with concentration, the CARS signal is well fitted by a parabola. This can be explained by the fact that chlorobenzene has a very high Raman polarizability, therefore the resonant signal contribution overwhelms the non-resonant one:

$$I_{\text{CARS}} \propto |\chi_{\text{R}}^{(3)} + \chi_{\text{NR}}^{(3)}|^2 \quad (4.29)$$

$$= |\chi_{\text{R}}^{(3)}|^2 + 2\chi_{\text{NR}}^{(3)} \text{Re}(\chi_{\text{R}}^{(3)}) + |\chi_{\text{NR}}^{(3)}|^2, \quad (4.30)$$

where $\chi_{\text{R}}^{(3)}$ and $\chi_{\text{NR}}^{(3)}$ are the resonant and non-resonant susceptibilities, respectively. For high concentration or strong Raman cross section, $\chi_{\text{R}}^{(3)} \gg \chi_{\text{NR}}^{(3)}$, then $I_{\text{AS}} \propto |\chi^{(3)}|^2 \approx |\chi_{\text{R}}^{(3)}|^2$ and the CARS signal is quadratic with the concentration [97].

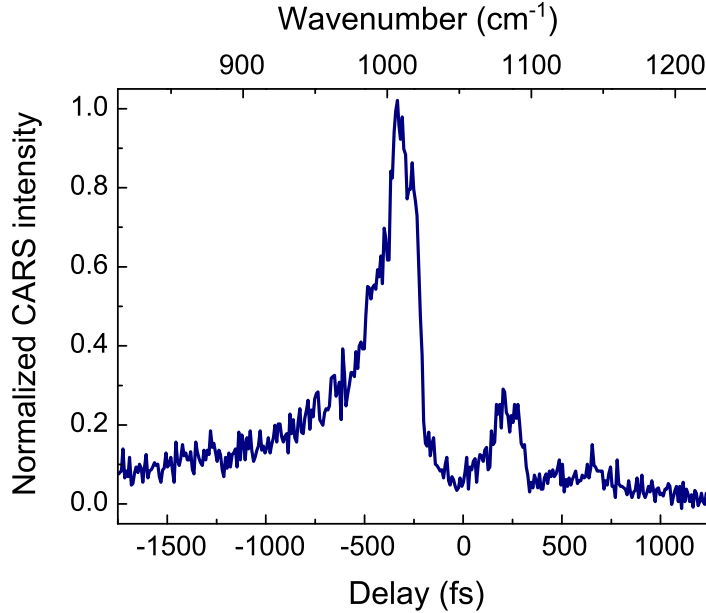


Figure 4.15: CARS spectrum of chlorobenzene acquired in 50 ms.

Figure 4.14(c) shows examples of CARS and SRS spectra. The non-resonant background strongly distorts the CARS spectrum, resulting in broader peaks, degraded spectral resolution ($\Delta\bar{\nu}_{\text{CARS}} \approx 30 \text{ cm}^{-1}$), and a shift to lower wavenumbers of the maximum spectral position of each Raman line. The SRS spectrum shows more detailed spectral features, in particular, the 1027 cm^{-1} Raman line is now resolved ($\Delta\bar{\nu}_{\text{CARS}} < 20 \text{ cm}^{-1}$), and the non-resonant background is absent.

The CARS spectrum was recorded in 0.7 s with a 400 signal-to-noise ratio (SNR), whereas 17 s were necessary to obtain a SNR of 15 in SRS for

an integration time of the lock-in amplifier $t_{\text{int}} = 100$ ms. CARS spectra can be acquired with a SNR of 70 in times as short as 50 ms, which corresponds to $125 \mu\text{s}/\text{cm}^{-1}$ (see Fig. 4.15). The only reason why CARS spectra were not recorded in even shorter times was the fact that the maximum speed of the motorized translation stage was reached. The SNR difference between CARS and SRS modes are further discussed in Section 4.6.

4.5 Study of a chemical equilibrium

A simple chemical system consisting of two molecular species in equilibrium in an aqueous solution was studied in order to demonstrate the performances of this setup. More specifically, the acid-base equilibria of aqueous phosphate in water was considered.

Aqueous phosphate can exist in four different forms depending on the acidity of its environment. Phosphoric acid is a weak acid, so the dissociation of solid phosphoric acid in water is only partial. The prevalent form is aqueous phosphoric acid (H_3PO_4). The pH of the solution is still very acid (close to 1). When adding a strong base to the solution, the pH increases and each of the three hydroxyl groups of phosphoric acid will successively get deprotonated. The following species are created: dihydrogen phosphate ion (H_2PO_4^-), hydrogen phosphate ion (HPO_4^{2-}) and phosphate ion (PO_4^{3-}). The three protonation reactions are characterized by three equilibrium constants $\text{pK}_{\text{A}1}$, $\text{pK}_{\text{A}2}$ and $\text{pK}_{\text{A}3}$, with

$$\text{pK}_{\text{A}} = -\log \left(\frac{[\text{X}^-][\text{H}_3\text{O}^+]}{[\text{XH}]} \right), \quad (4.31)$$

where $[\text{XH}]$ is concentration of the acid and $[\text{X}^-]$ is the concentration of the base.

The presence or absence of the four species at different pH values can be inferred from the results of a standard titration experiment. Figure 4.16(a) shows the titration curve obtained by slowly adding a 3 M sodium hydroxide solution to a 1 M phosphoric acid solution while monitoring the pH of the mixture with a pH-meter. Figure 4.16(b) shows the relative molar fraction of each of the four species calculated from the results obtained from the titration curve.

For solutions between pH 4 and pH 9, an equilibrium involving dihydrogen phosphate ion and hydrogen phosphate ion takes place in the solution:



It is assumed that the other forms of phosphate are only present in negligible quantities, as explained in Fig. 4.16. The equilibrium constant for this reaction

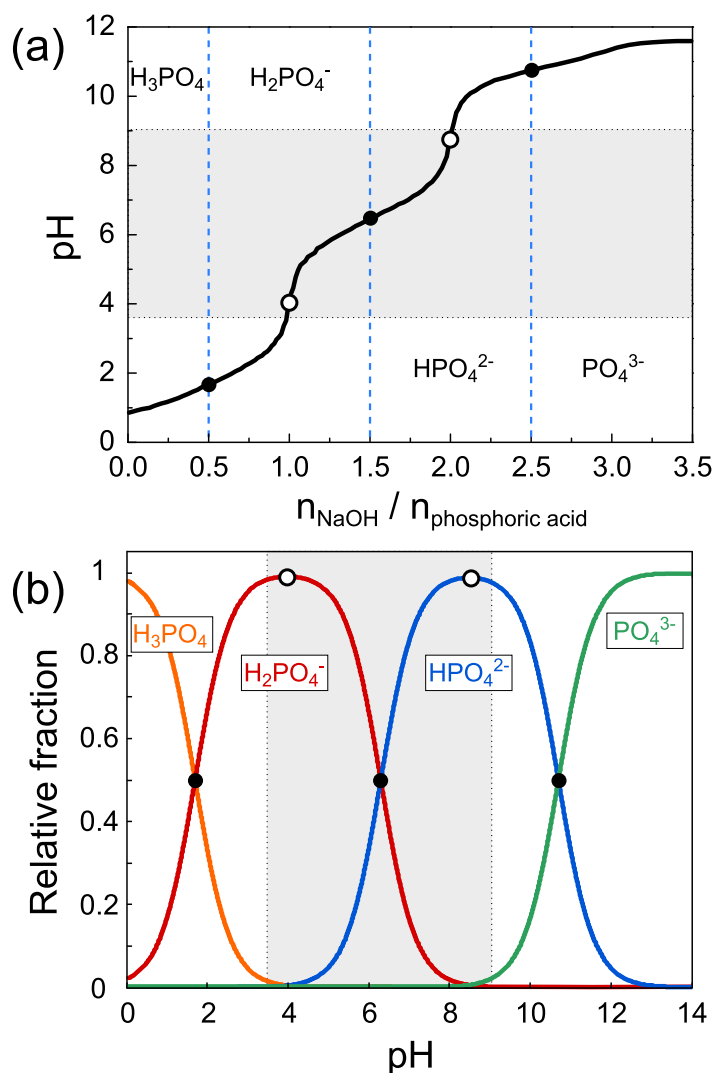


Figure 4.16: (a) Titration of 1 M aqueous solution of phosphoric by 3 M aqueous solution of sodium hydroxide solution. (b) Relative molar fraction of the four forms of phosphoric acid. (a) and (b) The full black dots mark the points where $\text{pH} = \text{pK}_A$ and the two species present in the solution have the same concentration. The circled white dots mark the equivalence points, where the pH is exactly halfway between two pK_A and there is only one of the four species present in the solution. The grayed out area on both plots shows the range of pH for which dihydrogen phosphate ions and hydrogen phosphate ions can be considered as the only two species present in the solution.

is written:

$$\text{pK}_{\text{A}2} = -\log\left(\frac{[\text{HPO}_4^{2-}][\text{H}_3\text{O}^+]}{[\text{H}_2\text{PO}_4^-]}\right). \quad (4.33)$$

The main Raman lines associated with H_2PO_4^- and HPO_4^{2-} are the $\text{P}(\text{OH})_2$ symmetric stretching at 874 cm^{-1} and PO_3 symmetric stretching at 987 cm^{-1} , respectively. The goal is to monitor the equilibrium change between hydrogen phosphate and dihydrogen phosphate (Eq. 4.32) by performing CARS and SRS spectra in the $800 - 1100\text{ cm}^{-1}$ spectral region which is directly accessible with the CRS setup.

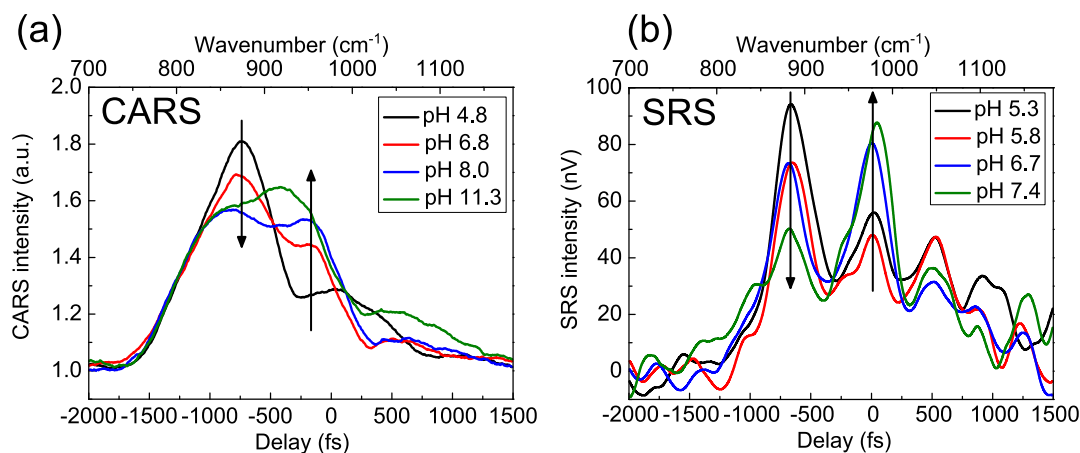


Figure 4.17: (a) CARS and (b) SRS spectra of 4 M mixtures of phosphoric acid and sodium hydroxide of different pH. Black arrows indicate the H_2PO_4^- (874 cm^{-1}) and HPO_4^{2-} (987 cm^{-1}) peaks evolution for increasing values of the pH.

CARS and SRS spectra have been recorded on several solutions of various pH that were prepared by mixing a phosphoric acid solution with sodium hydroxide solutions (Fig. 4.17). The pH values of the solutions were measured with a pH meter (Eutech Instruments) at room temperature. The three visible peaks correspond to the two aforementioned vibrational features plus the PO_2 symmetric stretching at 1074 cm^{-1} . The observed peaks are slightly shifted compared to the values in standard conditions due to the high concentration that was used here (4 M), in agreement with previous work [110]. Such high concentrations were used because of the small cross sections of the addressed Raman lines.

In both CARS and SRS experiments, the general evolution of the two main Raman peaks (874 cm^{-1} and 987 cm^{-1}) are in qualitative agreement with their expected behavior. Indeed, as the pH increases, the concentration of H_3O^+ in the solution decreases and the equilibrium is shifted to the right in Eq. 4.32, hence the respective decrease and increase of the H_2PO_4^- and HPO_4^{2-} peaks.

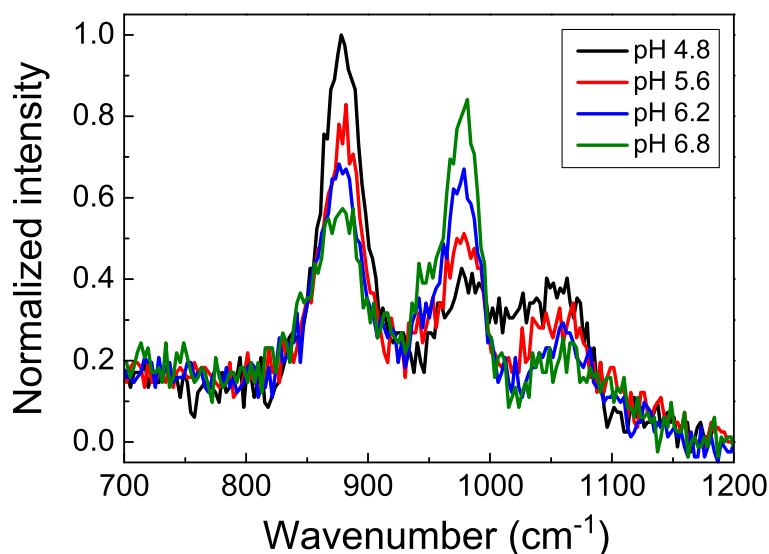


Figure 4.18: Raman spectra of mixtures of phosphoric acid and sodium hydroxide of different pH.

In Fig. 4.17 are plotted the CARS and SRS spectra that were obtained after a deconvolution procedure that takes into account the fact that the spectral and temporal overlap between the pump and Stokes pulses change when scanning the delay. The raw spectra were then weighted by the crosscorrelation function arising from the pump/Stokes overlap, resulting in the processed spectra shown in Fig. 4.17. The crosscorrelation function was obtained in two different ways for CARS and SRS. For CARS, it was assumed to be similar to the nonresonant background that was recovered by making the spectrum of water. For SRS, the overlap was estimated from the temporal shape of the pulses.

As previously mentioned, CARS spectra are strongly distorted by the interference between the resonant and the non-resonant contributions (Fig. 4.17(a)) whereas SRS (Fig. 4.17(b)) is expected to be proportional to the concentration.

In order to prove the ability of the system to get quantitative information about the concentration, the decimal logarithm of the ratio between the H_2PO_4^- (874 cm^{-1}) and HPO_4^{2-} (987 cm^{-1}) is plotted versus the pH value in Fig. 4.19, where CARS, SRS and spontaneous Raman data are presented.

Whereas CARS is very distorted compared to spontaneous Raman, SRS shows a good agreement with the Raman data, affirming its usefulness for quantifying concentrations.

The conducted chemical equilibrium monitoring between dihydrogen phosphate and hydrogen phosphate ions under pH change proves to be in favor of SRS for quantitative analysis. We emphasize here that the H_2PO_4^- (874 cm^{-1}) and HPO_4^{2-} (987 cm^{-1}) are particularly weak Raman lines that require 10 s

integration time in spontaneous Raman to get a SNR of 10. This is in contrast with the CH bands usually addressed in CRS technology that require a much shorter (10 times less) integration time.

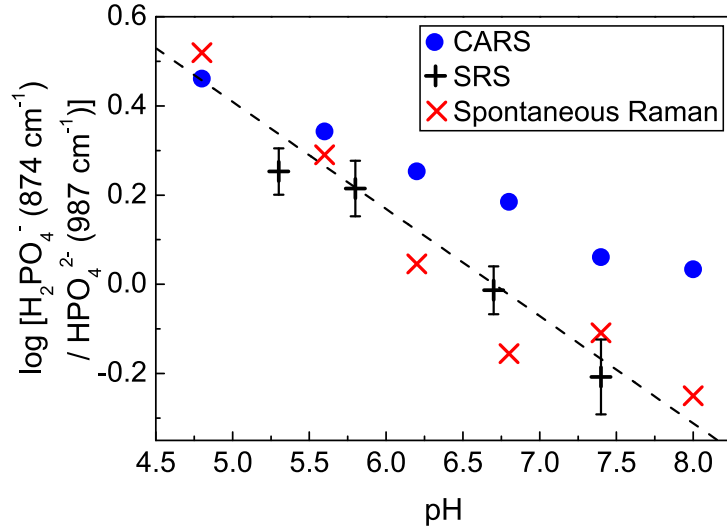


Figure 4.19: pH dependence of the decimal logarithm of the ratio between the intensity of the H₂PO₄⁻ (874 cm⁻¹) and HPO₄²⁻ (987 cm⁻¹) peaks for CARS, SRS and spontaneous Raman. The dashed black line corresponds to the linear fit of the spontaneous Raman data.

4.6 Signal-to-noise ratio

Ozeki and co-workers [111] have shown that the sensitivities of CARS and SRS microscopy are theoretically similar if the SRS signal is shot-noise-limited. In our CRS source, we consider that:

$$\frac{\text{SNR}_{\text{CARS}}^{\text{SN}}}{\text{SNR}_{\text{SRS}}^{\text{SN}}} \approx 1, \quad (4.34)$$

where $\text{SNR}_{\text{CARS}}^{\text{SN}}$ and $\text{SNR}_{\text{SRS}}^{\text{SN}}$ are the shot-noise-limited SNRs for CARS and SRS, respectively.

We can assume that the CARS signal is shot-noise-limited, however this is not the case for SRS. Noise measurements have shown that $\sigma_{\text{tot}}/\sigma_{\text{SN}} = 7$ dB in SRS, where σ_{tot} is the total noise and σ_{SN} is the shot noise. As a result, the ratio between the total SNRs of CARS and SRS reads:

$$\frac{\text{SNR}_{\text{CARS}}^{\text{tot}}}{\text{SNR}_{\text{SRS}}^{\text{tot}}} = \frac{\text{SNR}_{\text{CARS}}^{\text{SN}}}{\text{SNR}_{\text{SRS}}^{\text{SN}}} \times \frac{\sigma_{\text{tot}}}{\sigma_{\text{SN}}} \approx 5. \quad (4.35)$$

The experimentally observed ratio is 25, a factor 5 higher than predicted by Eq. 4.35. The outstanding factor can be explained by the difference in CARS and SRS collection efficiencies (factor 3.5) due to the different transmission of the optics at the two wavelengths. Additionally, the lock-in amplifier which only permitted modulation frequencies up to 2 MHz may have contributed to the electronic noise.

4.7 Conclusion

A compact CRS light source suitable to perform CARS and SRS vibrational spectroscopy of liquid samples was realized. Fast spectral scanning was made possible by tuning a delay line between two equally chirped pump and Stokes pulses, the latter being generated as a redshifted soliton in a PCF. The CRS source can address any vibrations up to 3000 cm^{-1} by means of soliton spectral tuning and can perform ultrafast spectral scanning (down to 20 ms for chlorobenzene sample) over a limited 400 cm^{-1} bandwidth. The ability of the developed light source to monitor acid/base molecular equilibrium change between dihydrogen phosphate and hydrogen phosphate ions under pH change. The system takes advantage of both fast signal acquisition in CARS and quantitative molecular concentration provided by SRS.

Conclusions and perspectives

In the first part of this work, the interest of a fiber-delivery scheme based on the generation of optical solitons was demonstrated. The design of the SC-PBG fiber made in IRCICA (Lille, France) was optimized to generate higher energy solitons than in classical PCFs, by adjusting the geometrical parameters to increase the group-velocity dispersion to nonlinear coefficient ratio. TPEF and SHG images of biological samples were obtained. The time of acquisition and signal-to-noise ratio were limited by the non-Gaussian shape of the beam in far-field. The wavelength tunability of the soliton was proven useful to recover the general features of the two-photon absorption cross-section spectrum of a fluorescent dye. Finally, the increase of the repetition rate from 80 MHz to 1 GHz was shown to improve the signal-to-noise ratio in TPEF measurements. The tunability of solitons could be further exploited in a multi-spectral or hyperspectral scheme. For instance, one could imagine a setup to obtain images of a biological sample marked with two dyes that would be selectively excited one after the other by switching the soliton wavelength at a high frequency.

The second part was dedicated to the time-resolved measurement of transient absorption in a pump-probe configuration. The mechanical delay scanning was successfully replaced by a high-speed voltage control of the soliton delay through a Pockels cell. This opens the door to faster measurements, but also to custom sampling strategies. This technique could be applied in the future for investigation of melanoma, as melanin is a strongly absorbing substance.

Finally, a single oscillator CRS setup was realized, where the Stokes wavelength was generated in the fiber through soliton soliton and SSFS. The spectral resolution was recovered by chirping the femtosecond pulses to a picosecond duration by grating pairs, following the spectral focusing strategy. CARS and SRS spectra could be acquired over a 400 cm^{-1} bandwidth, and the chemical equilibrium between two molecular species in aqueous solution was monitored upon pH variation. The signal-to-noise ratio was limited by the rather low energy of the solitons, as a regular PCF was used for this series of experiments. In the future, it would be interesting to increase the soliton energy by generating the soliton in a SC-PBG similar to the one that was used in the two previous parts.

The present work focused on the fiber delivery part of the problem of applying nonlinear microscopy to an endoscopic scheme and therefore can be seen as the

first step in the design of a nonlinear endoscope based on soliton generation. The development of a microscanning system would be the next step toward the miniaturization of the required optics to scan the focus over a sufficient field-of-view. Finally, the collection of the signal in the epi direction through the same fiber could be done with a double-clad fiber.

Appendix A

Permittivity, refractive index and absorption coefficient

Linear case

Let us write again the propagation equation:

$$\Delta \mathbf{E}(\mathbf{r}, t) - \frac{1}{c^2} \frac{\partial^2 \mathbf{E}}{\partial t^2}(\mathbf{r}, t) = \mu_0 \frac{\partial^2 \mathbf{P}}{\partial t^2}(\mathbf{r}, t). \quad (36)$$

Assuming the polarization density to be linear, it is possible to show that:

$$\Delta \tilde{\mathbf{E}}(\mathbf{r}, \omega) + \frac{\varepsilon(\omega)\omega^2}{c^2} \tilde{\mathbf{E}}(\mathbf{r}, \omega) = 0. \quad (37)$$

$\tilde{\mathbf{E}}(\mathbf{r}, \omega)$ is the Fourier transform of the electric field $\mathbf{E}(\mathbf{r}, t)$, and:

$$\varepsilon(\omega) = 1 + \chi^{(1)}(\omega) = \left(n(\omega) + \frac{i\alpha(\omega)}{2k_0} \right)^2, \quad (38)$$

where $\chi^{(1)}(\omega)$ is the linear susceptibility, $n(\omega)$ is the refractive index $\alpha(\omega)$ is the absorption coefficient.

From Eq. 38, we can draw:

$$\begin{aligned} n(\omega) &= \operatorname{Re} \left(\sqrt{\varepsilon(\omega)} \right) \\ &= \operatorname{Re} \left(\sqrt{1 + \chi^{(1)}(\omega)} \right) \\ &\approx \operatorname{Re} \left(1 + \frac{1}{2} \chi^{(1)}(\omega) \right) \\ &\approx 1 + \frac{1}{2} \operatorname{Re} (\chi^{(1)}(\omega)). \end{aligned} \quad (39)$$

And

$$\begin{aligned} \alpha(\omega) &= \frac{2\omega}{c} \operatorname{Im} \left(\sqrt{\varepsilon(\omega)} \right) \\ &\approx \frac{2\omega}{c} \operatorname{Im} \left(1 + \frac{1}{2} \chi^{(1)}(\omega) \right) \\ &\approx \frac{\omega}{c} \operatorname{Im} (\chi^{(1)}(\omega)). \end{aligned} \quad (40)$$

Nonlinearities

In the frame of the perturbation theory, we can introduce a nonlinear polarization of the form:

$$\mathbf{P}_L(\mathbf{r}, t) = \varepsilon_0 \iiint \chi^{(3)}(t - t_1, t - t_2, t - t_3) : \mathbf{E}(\mathbf{r}, t_1) \mathbf{E}(\mathbf{r}, t_2) \mathbf{E}(\mathbf{r}, t_3) dt_1 dt_2 dt_3. \quad (41)$$

Unlike the linear response of a medium to the excitation of the electric field, its nonlinear response can be assumed to be instantaneous:

$$\mathbf{P}_{NL}(\mathbf{r}, t) = \varepsilon_0 \chi^{(3)} : \mathbf{E}(\mathbf{r}, t) \mathbf{E}(\mathbf{r}, t) \mathbf{E}(\mathbf{r}, t). \quad (42)$$

For the treatment of a nonlinear problem by using the complex notation, we should not forget to include the complex conjugate part in the expression of the fields. The electric field then writes:

$$\mathbf{E}(\mathbf{r}, t) = \frac{1}{2} (E(\mathbf{r}, t)e^{-i\omega_0 t} + E^*(\mathbf{r}, t)e^{i\omega_0 t}) \hat{x}. \quad (43)$$

By introducing Eq. 43 into Eq. 42, we get:

$$\mathbf{P}_{NL}(\mathbf{r}, t) = \frac{1}{8} \varepsilon_0 \chi^{(3)} (E(\mathbf{r}, t)e^{-i\omega_0 t} + E^*(\mathbf{r}, t)e^{i\omega_0 t})^3 \hat{x}. \quad (44)$$

The development gives:

$$\begin{aligned} \mathbf{P}_{NL}(\mathbf{r}, t) &= \frac{1}{8} \varepsilon_0 \chi^{(3)} \left(E^3(\mathbf{r}, t)e^{-3i\omega_0 t} + 3E^2(\mathbf{r}, t)e^{-2i\omega_0 t} E^*(\mathbf{r}, t)e^{i\omega_0 t} \right. \\ &\quad \left. + 3E(\mathbf{r}, t)e^{-i\omega_0 t} E^{*2}(\mathbf{r}, t)e^{2i\omega_0 t} + E^{*3}(\mathbf{r}, t)e^{3i\omega_0 t} \right) \hat{x} \\ &= \frac{1}{8} \varepsilon_0 \chi^{(3)} \left(E^3(\mathbf{r}, t)e^{-3i\omega_0 t} + E^{*3}(\mathbf{r}, t)e^{3i\omega_0 t} \right. \\ &\quad \left. + 3|E(\mathbf{r}, t)|^2 (E(\mathbf{r}, t)e^{-i\omega_0 t} + E^*(\mathbf{r}, t)e^{i\omega_0 t}) \right) \hat{x}. \end{aligned} \quad (45)$$

The $3\omega_0$ terms require phase matching and can be neglected in optical fibers. Then:

$$\mathbf{P}_{NL}(\mathbf{r}, t) = \frac{3}{8} \varepsilon_0 \chi^{(3)} |E(\mathbf{r}, t)|^2 (E(\mathbf{r}, t)e^{-i\omega_0 t} + E^*(\mathbf{r}, t)e^{i\omega_0 t}) \hat{x}. \quad (46)$$

And, with Eq. 43:

$$\mathbf{P}_{NL}(\mathbf{r}, t) = \frac{3}{4} \varepsilon_0 \chi^{(3)} |E(\mathbf{r}, t)|^2 \mathbf{E}(\mathbf{r}, t) \hat{x}. \quad (47)$$

We can define ε_{NL} as:

$$\varepsilon_{NL} = \frac{3}{4} \chi^{(3)} |E(\mathbf{r}, t)|^2, \quad (48)$$

and then:

$$\mathbf{P}_{\text{NL}}(\mathbf{r}, t) = \varepsilon_0 \varepsilon_{\text{NL}} \mathbf{E}(\mathbf{r}, t) \hat{x}. \quad (49)$$

We then have:

$$\varepsilon(\omega) = 1 + \chi^{(1)}(\omega) + \varepsilon_{\text{NL}} = 1 + \chi^{(1)}(\omega) + \frac{3}{4} \chi^{(3)} |E|^2 \quad (50)$$

Justification by Agrawal [33]: “ To obtain the wave equation for the slowly varying amplitude $\mathbf{E}(\mathbf{r}, t)$, it is more convenient to work in the Fourier domain. This is generally not possible as the equation is non linear because of the intensity dependence of ε_{NL} . In one approach, ε_{NL} is treated as a constant during the derivation of the propagation equation. The approach is justified in view of the SVEA and the perturbative nature of \mathbf{P}_{NL} .”

The small perturbation induces the following changes for $n(\omega)$ and $\alpha(\omega)$:

$$\left\{ \begin{array}{l} n(\omega) \rightarrow n(\omega) + n_2 |E|^2 \\ \alpha(\omega) \rightarrow \alpha(\omega) + \alpha_2 |E|^2 \end{array} \right. \quad (51a)$$

$$\quad (51b)$$

In a similar manner as in Eq. 39 and 40, we draw:

$$\begin{aligned} n(\omega) &= \text{Re} \left(\sqrt{\varepsilon(\omega)} \right) \\ &= \text{Re} \left(\sqrt{1 + \chi^{(1)}(\omega) + \frac{3}{4} \chi^{(3)} |E|^2} \right) \\ &\approx \text{Re} \left(1 + \frac{1}{2} \chi^{(1)}(\omega) + \frac{3}{8} \chi^{(3)} |E|^2 \right) \\ &\approx \underbrace{1 + \frac{1}{2} \text{Re}(\chi^{(1)}(\omega))}_{n_{\text{lin}}} + \underbrace{\frac{3}{8} \text{Re}(\chi^{(3)}) |E|^2}_{n_2}. \end{aligned} \quad (52)$$

And

$$\begin{aligned} \alpha(\omega) &= \frac{2\omega}{c} \text{Im} \left(\sqrt{\varepsilon(\omega)} \right) \\ &\approx \frac{2\omega}{c} \text{Im} \left(1 + \frac{1}{2} \chi^{(1)}(\omega) + \frac{3}{8} \chi^{(3)} |E|^2 \right) \\ &\approx \underbrace{\frac{\omega}{c} \text{Im}(\chi^{(1)}(\omega))}_{\alpha_{\text{lin}}} + \underbrace{\frac{3\omega}{4c} \text{Im}(\chi^{(3)}) |E|^2}_{\alpha_2}. \end{aligned} \quad (53)$$

Appendix B

Thoughts on the time-bandwidth product

1 Gaussian pulse

Fourier transform of a Gaussian pulse:

$$e^{-at^2} \rightarrow Ae^{-\omega^2/(4a)} \quad (54)$$

Full width at half maximum of a Gaussian pulse written $E_0e^{-\alpha x^2}$:

$$E_0e^{-\alpha x_{1/2}^2} = E_0/2 \quad (55)$$

$$\Delta x_{\text{FWHM}} = 2x_{1/2} = 2\sqrt{\frac{\ln 2}{\alpha}} \quad (56)$$

If we write the electric field in the time domain as follows:

$$E(t) = E(0)e^{-t^2/\tau^2}, \quad (57)$$

then in the frequency domain, the Fourier transform gives:

$$\tilde{E}(\omega) = \tilde{E}(0)e^{-\omega^2\tau^2/4}. \quad (58)$$

In the experiments, what we deal with are the optical intensities:

$$|E(t)|^2 = |E(0)|^2 e^{-2t^2/\tau^2} \quad (59)$$

$$|\tilde{E}(\omega)|^2 = |\tilde{E}(0)|^2 e^{-\omega^2\tau^2/2}. \quad (60)$$

Now we can write the full widths at half maximum for both time and frequency domains.

$$\Delta t_{\text{FWHM}} = 2\tau\sqrt{\frac{\ln 2}{2}} = \tau\sqrt{2 \ln 2} \quad (61)$$

$$\Delta \omega_{\text{FWHM}} = \frac{2}{\tau}\sqrt{2 \ln 2}. \quad (62)$$

From the last equation:

$$\Delta f_{\text{FWHM}} = \frac{\Delta \omega_{\text{FWHM}}}{2\pi} = \frac{1}{\pi\tau}\sqrt{2 \ln 2} \quad (63)$$

And finally:

$$\Delta t_{\text{FWHM}}\Delta f_{\text{FWHM}} = \frac{2 \ln 2}{\pi} \approx 0.441. \quad (64)$$

2 Sech-squared pulse

Fourier transform of a sech pulse:

$$\text{sech}(t/\tau) \rightarrow A \text{sech}\left(\frac{\pi}{2}\tau\omega\right) \quad (65)$$

Reciprocal function for a sech-square function $\text{sech}^2(y)$:

$$y_Y = \text{argsech2}(Y) = \ln\left(\sqrt{\frac{1}{Y}} + \sqrt{\frac{1}{Y} - 1}\right) \quad (66)$$

For $Y = 1/2$ we have:

$$y_{1/2} = \text{argsech2}(1/2) = \ln\left(1 + \sqrt{2}\right) \quad (67)$$

Full width at half maximum of a sech-squared pulse written $E_0 \text{sech}^2(x/\mu)$:

$$\Delta x_{\text{FWHM}} = 2 \ln\left(1 + \sqrt{2}\right) \mu \quad (68)$$

Electric field in the time domain:

$$E(t) = E(0) \text{sech}\left(\frac{t}{\tau}\right), \quad (69)$$

In the frequency domain, the Fourier transform gives:

$$\tilde{E}(\omega) = \tilde{E}(0) \text{sech}\left(\frac{\pi}{2}\omega\tau\right). \quad (70)$$

Optical intensities:

$$|E(t)|^2 = |E(0)|^2 \text{sech}^2\left(\frac{t}{\tau}\right) \quad (71)$$

$$|\tilde{E}(\omega)|^2 = |\tilde{E}(0)|^2 \text{sech}^2\left(\frac{\pi}{2}\omega\tau\right). \quad (72)$$

Full widths at half maximum:

$$\Delta t_{\text{FWHM}} = 2 \ln\left(1 + \sqrt{2}\right) \tau \quad (73)$$

$$\Delta \omega_{\text{FWHM}} = \frac{4 \ln\left(1 + \sqrt{2}\right)}{\pi \tau}. \quad (74)$$

From the last equation:

$$\Delta f_{\text{FWHM}} = \frac{\Delta \omega_{\text{FWHM}}}{2\pi} = \frac{2 \ln\left(1 + \sqrt{2}\right)}{\pi^2 \tau} \quad (75)$$

And finally:

$$\Delta t_{\text{FWHM}} \Delta f_{\text{FWHM}} = \frac{4 \left(\ln\left(1 + \sqrt{2}\right)\right)^2}{\pi^2} \approx 0.315. \quad (76)$$

Bibliography

- [1] G. Keiser, *Optical fiber communications* (McGraw-Hill, Boston, 2000), 3rd ed.
- [2] P. St. J. Russell, “Photonic crystal fibers,” *Science* **299**, 358–362 (2003).
- [3] J. E. Sharping, M. Fiorentino, P. Kumar, and R. S. Windeler, “Optical parametric oscillator based on four-wave mixing in microstructure fiber,” *Opt. Lett.* **27**, 1675–1677 (2002).
- [4] J. Hansryd, P. Andrekson, M. Westlund, J. Li, and P. Hedekvist, “Fiber-based optical parametric amplifiers and their applications,” *IEEE J. Sel. Top. Quant.* **8**, 506–520 (2002).
- [5] T. G. Philbin, C. Kuklewicz, S. Robertson, S. Hill, F. König, and U. Leonhardt, “Fiber-optical analog of the event horizon,” *Science* **319**, 1367–1370 (2008).
- [6] J. K. Ranka, R. S. Windeler, and A. J. Stentz, “Visible continuum generation in air-silica microstructure optical fibers with anomalous dispersion at 800 nm,” *Opt. Lett.* **25**, 25–27 (2000).
- [7] J. M. Dudley, G. Genty, and S. Coen, “Supercontinuum generation in photonic crystal fiber,” *Rev. Mod. Phys.* **78**, 1135–1184 (2006).
- [8] H. Kano and H. Hamaguchi, “*In vivo* multi-nonlinear optical imaging of a living cell using a supercontinuum light source generated from a photonic crystal fiber,” *Opt. Express* **14**, 2798–2804 (2006).
- [9] R. Holzwarth, T. Udem, T. W. Hänsch, J. C. Knight, W. J. Wadsworth, and P. St. J. Russell, “Optical frequency synthesizer for precision spectroscopy,” *Phys. Rev. Lett.* **85**, 2264–2267 (2000).
- [10] T. Udem, R. Holzwarth, and T. W. Hänsch, “Optical frequency metrology,” *Nature* **416**, 233–237 (2002).
- [11] B. Povazay, K. Bizheva, A. Unterhuber, B. Hermann, H. Sattmann, A. F. Fercher, W. Drexler, A. Apolonski, W. J. Wadsworth, J. C. Knight, P. St. J. Russell, M. Vetterlein, and E. Scherzer, “Submicrometer axial resolution optical coherence tomography,” *Opt. Lett.* **27**, 1800–1802 (2002).

- [12] D. L. Marks, A. L. Oldenburg, J. J. Reynolds, and S. A. Boppart, “Study of an ultrahigh-numerical-aperture fiber continuum generation source for optical coherence tomography,” *Opt. Lett.* **27**, 2010–2012 (2002).
- [13] T. A. Birks, J. C. Knight, and P. St. J. Russell, “Endlessly single-mode photonic crystal fiber,” *Opt. Lett.* **22**, 961–963 (1997).
- [14] P. St. J. Russell, “Photonic-crystal fibers,” *J. Lightwave Technol.* **24**, 4729–4749 (2006).
- [15] J. C. Knight, J. Broeng, T. A. Birks, and P. St. J. Russell, “Photonic band gap guidance in optical fibers,” *Science* **282**, 1476–1478 (1998).
- [16] T. Birks, P. Roberts, P. St. J. Russell, D. M. Atkin, and T. Shepherd, “Full 2-D photonic bandgaps in silica/air structures,” *Electron. Lett.* **31**, 1941–1943 (1995).
- [17] R. F. Cregan, B. J. Mangan, J. C. Knight, T. A. Birks, P. St. J. Russell, P. J. Roberts, and D. C. Allan, “Single-mode photonic band gap guidance of light in air,” *Science* **285**, 1537–1539 (1999).
- [18] G. Bouwmans, F. Luan, J. Knight, P. St. J. Russell, L. Farr, B. Mangan, and H. Sabert, “Properties of a hollow-core photonic bandgap fiber at 850 nm wavelength,” *Opt. Express* **11**, 1613–1620 (2003).
- [19] F. Benabid, “Hollow-core photonic bandgap fibre: new light guidance for new science and technology,” *Philos. T. Roy. Soc. B* **364**, 3439–3462 (2006).
- [20] P. J. Roberts, F. Couny, H. Sabert, B. J. Mangan, D. P. Williams, L. Farr, M. W. Mason, A. Tomlinson, T. A. Birks, J. C. Knight, and P. St. J. Russell, “Ultimate low loss of hollow-core photonic crystal fibres,” *Opt. Express* **13**, 236–244 (2005).
- [21] F. Benabid, J. C. Knight, G. Antonopoulos, and P. St. J. Russell, “Stimulated Raman scattering in hydrogen-filled hollow-core photonic crystal fiber,” *Science* **298**, 399–402 (2002).
- [22] F. Couny, F. Benabid, and P. S. Light, “Large-pitch kagome-structured hollow-core photonic crystal fiber,” *Opt. Lett.* **31**, 3574–3576 (2006).
- [23] G. J. Pearce, G. S. Wiederhecker, C. G. Poulton, S. Burger, and P. St. J. Russell, “Models for guidance in kagome-structured hollow-core photonic crystal fibres,” *Opt. Express* **15**, 12680–12685 (2007).

- [24] P. Ghenuche, S. Rammler, N. Y. Joly, M. Scharrer, M. Frosz, J. Wenger, P. St. J. Russell, and H. Rigneault, “Kagome hollow-core photonic crystal fiber probe for Raman spectroscopy,” *Opt. Lett.* **37**, 4371–4373 (2012).
- [25] F. Luan, A. K. George, T. D. Hedley, G. J. Pearce, D. M. Bird, J. C. Knight, and P. St. J. Russell, “All-solid photonic bandgap fiber,” *Opt. Lett.* **29**, 2369–2371 (2004).
- [26] A. Isomäki and O. G. Okhotnikov, “Femtosecond soliton mode-locked laser based on ytterbium-doped photonic bandgap fiber,” *Opt. Express* **14**, 9238–9243 (2006).
- [27] K. Saitoh, T. Muraio, L. Rosa, and M. Koshiha, “Effective area limit of large-mode-area solid-core photonic bandgap fibers for fiber laser applications,” *Opt. Fib. Technol.* **16**, 409–418 (2010).
- [28] A. Shirakawa, H. Maruyama, K. Ueda, C. B. Olausson, J. K. Lyngsø, and J. Broeng, “High-power Yb-doped photonic bandgap fiber amplifier at 1150–1200 nm,” *Opt. Express* **17**, 447–454 (2009).
- [29] A. Fuerbach, P. Steinvurzel, J. A. Bolger, A. Nulsen, and B. J. Eggleton, “Nonlinear propagation effects in antiresonant high-index inclusion photonic crystal fibers,” *Opt. Lett.* **30**, 830–832 (2005).
- [30] B. Kibler, T. Martynkien, M. Szpulak, C. Finot, J. Fatome, J. Wojcik, W. Urbanczyk, and S. Wabnitz, “Nonlinear femtosecond pulse propagation in an all-solid photonic bandgap fiber,” *Opt. Express* **17**, 10393–10398 (2009).
- [31] A. Bétourné, A. Kudlinski, G. Bouwmans, O. Vanvincq, A. Mussot, and Y. Quiquempois, “Control of supercontinuum generation and soliton self-frequency shift in solid-core photonic bandgap fibers,” *Opt. Lett.* **34**, 3083–3085 (2009).
- [32] J. D. Jackson, *Classical electrodynamics* (Wiley, New York, 1998), 3rd ed.
- [33] G. P. Agrawal, *Nonlinear fiber optics* (Academic Press, San Diego, 2001), 3rd ed.
- [34] C. Rullière, *Femtosecond laser pulses* (Springer, New York, NY, 2005), 2nd ed.
- [35] J. Y. Lee and D. Y. Kim, “Versatile chromatic dispersion measurement of a single mode fiber using spectral white light interferometry,” *Opt. Express* **14**, 11608–11615 (2006).

- [36] M. Oberthaler and R. A. Höpfel, “Special narrowing of ultrashort laser pulses by self-phase modulation in optical fibers,” *Appl. Phys. Lett.* **63**, 1017–1019 (1993).
- [37] A. Hasegawa and F. Tappert, “Transmission of stationary nonlinear optical pulses in dispersive dielectric fibers. I. Anomalous dispersion,” *Appl. Phys. Lett.* **23**, 142–144 (1973).
- [38] R. H. Stolen, W. J. Tomlinson, and L. F. Mollenauer, “Observation of pulse restoration at the soliton period in optical fibers,” *Opt. Lett.* **8**, 186–188 (1983).
- [39] J. Satsuma and N. Yajima, “Initial value problems of one-dimensional self-modulation of nonlinear waves in dispersive media,” *Prog. Theor. Phys. Suppl.* **55**, 284–306 (1974).
- [40] F. M. Mitschke and L. F. Mollenauer, “Discovery of the soliton self-frequency shift,” *Opt. Lett.* **11**, 659–661 (1986).
- [41] J. P. Gordon, “Theory of the soliton self-frequency shift,” *Opt. Lett.* **11**, 662–664 (1986).
- [42] A. Bondeson, M. Lisak, and D. Anderson, “Soliton perturbations: A variational principle for the soliton parameters,” *Phys. Scr.* **20**, 479 (1979).
- [43] A. V. Husakou and J. Herrmann, “Supercontinuum generation, four-wave mixing, and fission of higher-order solitons in photonic-crystal fibers,” *J. Opt. Soc. Am. B* **19**, 2171–2182 (2002).
- [44] W. Denk, J. Strickler, and W. Webb, “Two-photon laser scanning fluorescence microscopy,” *Science* **248**, 73–76 (1990).
- [45] K. König, “Multiphoton microscopy in life sciences,” *J. Microsc.* **200**, 83–104 (2000).
- [46] F. Helmchen and W. Denk, “Deep tissue two-photon microscopy,” *Nat. Methods* **2**, 932–940 (2005).
- [47] E. E. Hoover and J. A. Squier, “Advances in multiphoton microscopy technology,” *Nature Photon.* **7**, 93–101 (2013).
- [48] B. I. Hirschowitz, L. E. Curtiss, C. W. Peters, and H. M. Pollard, “Demonstration of a new gastroscope, the fiberscope,” *Gastroenterology* **35**, 50–53 (1958).

- [49] W. R. Zipfel, R. M. Williams, and W. W. Webb, “Nonlinear magic: multiphoton microscopy in the biosciences,” *Nat. Biotechnol.* **21**, 1369–1377 (2003).
- [50] B. W. Atherton and M. K. Reed, “Prechirped fiber transport of 800-nm 100-fs pulses,” *Proc. SPIE* pp. 22–25 (1998).
- [51] S. W. Clark, F. Ö. Ilday, and F. W. Wise, “Fiber delivery of femtosecond pulses from a Ti:sapphire laser,” *Opt. Lett.* **26**, 1320–1322 (2001).
- [52] M. T. Myaing, D. J. MacDonald, and X. Li, “Fiber-optic scanning two-photon fluorescence endoscope,” *Opt. Lett.* **31**, 1076–1078 (2006).
- [53] H. Bao, J. Allen, R. Pattie, R. Vance, and M. Gu, “Fast handheld two-photon fluorescence microendoscope with a $475\ \mu\text{m} \times 475\ \mu\text{m}$ field of view for *in vivo* imaging,” *Opt. Lett.* **33**, 1333–1335 (2008).
- [54] D. R. Rivera, C. M. Brown, D. G. Ouzounov, I. Pavlova, D. Kobat, W. W. Webb, and C. Xu, “Compact and flexible raster scanning multiphoton endoscope capable of imaging unstained tissue,” *Proc. Natl. Acad. Sci. U.S.A.* **108**, 17598–17603 (2011).
- [55] M. T. Myaing, J. Y. Ye, T. B. Norris, T. Thomas, J. R. Baker Jr., W. J. Wadsworth, G. Bouwmans, J. C. Knight, and P. St. J. Russell, “Enhanced two-photon biosensing with double-clad photonic crystal fibers,” *Opt. Lett.* **28**, 1224–1226 (2003).
- [56] L. Fu, A. Jain, C. Cranfield, H. Xie, and M. Gu, “Three-dimensional nonlinear optical endoscopy,” *J. Biomed. Opt.* **12**, 040501 (2007).
- [57] S. Tang, W. Jung, D. McCormick, T. Xie, J. Su, Y.-C. Ahn, B. J. Tromberg, and Z. Chen, “Design and implementation of fiber-based multiphoton endoscopy with microelectromechanical systems scanning,” *J. Biomed. Opt.* **14**, 034005 (2009).
- [58] M. Lelek, E. Suran, F. Louradour, A. Barthelemy, B. Viellerobe, and F. Lacombe, “Coherent femtosecond pulse shaping for the optimization of a non-linear micro-endoscope,” *Opt. Express* **15**, 10154–10162 (2007).
- [59] C. Lefort, T. Mansuryan, F. Louradour, and A. Barthelemy, “Pulse compression and fiber delivery of 45 fs Fourier transform limited pulses at 830 nm,” *Opt. Lett.* **36**, 292–294 (2011).
- [60] B. A. Flusberg, J. C. Jung, E. D. Cocker, E. P. Anderson, and M. J. Schnitzer, “*In vivo* brain imaging using a portable 3.9 gram two-photon fluorescence microendoscope,” *Opt. Lett.* **30**, 2272–2274 (2005).

- [61] C. J. Engelbrecht, R. S. Johnston, E. J. Seibel, and F. Helmchen, “Ultra-compact fiber-optic two-photon microscope for functional fluorescence imaging *in vivo*,” *Opt. Express* **16**, 5556–5564 (2008).
- [62] S. Brustlein, P. Berto, R. Hostein, P. Ferrand, C. Billaudeau, D. Marguet, A. Muir, J. Knight, and H. Rigneault, “Double-clad hollow core photonic crystal fiber for coherent Raman endoscope,” *Opt. Express* **19**, 12562–12568 (2011).
- [63] D. M. Huland, K. Charan, D. G. Ouzounov, J. S. Jones, N. Nishimura, and C. Xu, “Three-photon excited fluorescence imaging of unstained tissue using a GRIN lens endoscope,” *Biomed. Opt. Express* **4**, 652–658 (2013).
- [64] S. Moon, G. Liu, and Z. Chen, “Multiphoton endoscopy based on a mode-filtered single-mode fiber,” *Proc. SPIE* **7903**, 79032P (2011).
- [65] D. G. Ouzounov, F. R. Ahmad, D. Müller, N. Venkataraman, M. T. Gallagher, M. G. Thomas, J. Silcox, K. W. Koch, and A. L. Gaeta, “Generation of megawatt optical solitons in hollow-core photonic band-gap fibers,” *Science* **301**, 1702–1704 (2003).
- [66] K. Wang and C. Xu, “Tunable high-energy soliton pulse generation from a large-mode-area fiber and its application to third harmonic generation microscopy,” *Appl. Phys. Lett.* **99**, 071112 (2011).
- [67] P. Mahou, M. Zimmerley, K. Loulier, K. S. Matho, G. Labroille, X. Morin, W. Supatto, J. Livet, D. Débarre, and E. Beaurepaire, “Multicolor two-photon tissue imaging by wavelength mixing,” *Nat Meth* **9**, 815–818 (2012).
- [68] R. D. Roorda, T. M. Hohl, R. Toledo-Crow, and G. Misenböck, “Video-rate nonlinear microscopy of neuronal membrane dynamics with genetically encoded probes,” *Journal of Neurophysiology* **92**, 609–621 (2004).
- [69] K. Murari, Y. Zhang, S. Li, Y. Chen, M.-J. Li, and X. Li, “Compensation-free, all-fiber-optic, two-photon endomicroscopy at 1.55 μm ,” *Opt. Lett.* **36**, 1299–1301 (2011).
- [70] G. Liu, K. Kieu, F. W. Wise, and Z. Chen, “Multiphoton microscopy system with a compact fiber-based femtosecond-pulse laser and handheld probe,” *J. Biophotonics* **4**, 34–39 (2011).
- [71] O. Vanvincq, A. Kudlinski, A. Bétourné, Y. Quiquempois, and G. Bouwmans, “Extreme deceleration of the soliton self-frequency shift by the third-order dispersion in solid-core photonic bandgap fibers,” *J. Opt. Soc. Am. B* **27**, 2328–2335 (2010).

- [72] O. Vanvincq, B. Barviau, A. Mussot, G. Bouwmans, Y. Quiquempois, and A. Kudlinski, “Significant reduction of power fluctuations at the long-wavelength edge of a supercontinuum generated in solid-core photonic bandgap fibers,” *Opt. Express* **18**, 24352–24360 (2010).
- [73] O. Vanvincq, “Étude théorique des propriétés optiques linéaires et non-linéaires des fibres à bandes interdites photoniques à cœur solide,” Ph.D. thesis, Université Lille 1 - Sciences et technologies (2011).
- [74] A. Bendahmane, A. Mussot, O. Vanvincq, G. Bouwmans, A. Kudlinski, S. Saint-Jalm, E. R. Andresen, and H. Rigneault, “Solid-core photonic bandgap fiber for the generation of tunable high-energy solitons,” in “3rd Workshop on Specialty Optical Fibers and their applications,” (Optical Society of America, 2013), p. W3.36.
- [75] M. A. Albota, C. Xu, and W. W. Webb, “Two-photon fluorescence excitation cross sections of biomolecular probes from 690 to 960 nm,” *Appl. Opt.* **37**, 7352–7356 (1998).
- [76] N. Ji, J. C. Magee, and E. Betzig, “High-speed, low-photodamage nonlinear imaging using passive pulse splitters,” *Nat. Methods* **5**, 197–202 (2008).
- [77] N. S. Makarov, M. Drobizhev, and A. Rebane, “Two-photon absorption standards in the 550–1600 nm excitation wavelength range,” *Opt. Express* **16**, 4029–4047 (2008).
- [78] B. Chance, “The accelerated flow method for rapid reactions,” *J. Franklin I.* **229**, 737–766 (1940).
- [79] G. Porter, “Flash photolysis and spectroscopy. a new method for the study of free radical reactions,” *Proc. R. Soc. Lond. A* **200**, 284–300 (1950).
- [80] W. Min, C. W. Freudiger, S. Lu, and X. S. Xie, “Coherent nonlinear optical imaging: Beyond fluorescence microscopy,” *Annu. Rev. Phys. Chem.* **62**, 507–530 (2011).
- [81] R. Berera, R. van Grondelle, and J. T. M. Kennis, “Ultrafast transient absorption spectroscopy: principles and application to photosynthetic systems,” *Photosynth. Res.* **101**, 105–118 (2009).
- [82] D. Fu, T. Ye, T. E. Matthews, G. Yurtsever, and W. S. Warren, “Two-color, two-photon, and excited-state absorption microscopy,” *J. Biomed. Opt.* **12**, 054004 (2007).

- [83] T. Ye, D. Fu, and W. S. Warren, “Nonlinear absorption microscopy,” *Photochem. Photobiol.* **85**, 631–645 (2009).
- [84] F. E. Robles, J. W. Wilson, M. C. Fischer, and W. S. Warren, “Phasor analysis for nonlinear pump-probe microscopy,” *Opt. Express* **20**, 17082–17092 (2012).
- [85] P. A. Riley, “Melanin,” *Int. J. Biochem. Cell B.* **29**, 1235–1239 (1997).
- [86] M. Brenner and V. J. Hearing, “The protective role of melanin against UV damage in human skin,” *Photochem. Photobiol.* **84**, 539–549 (2008).
- [87] B. A. Gilchrest, M. S. Eller, A. C. Geller, and M. Yaar, “The pathogenesis of melanoma induced by ultraviolet radiation,” *New. Engl. J. Med.* **340**, 1341–1348 (1999).
- [88] A. J. Thody, E. M. Higgins, K. Wakamatsu, S. Ito, S. A. Burchill, and J. M. Marks, “Pheomelanin as well as eumelanin is present in human epidermis,” *J. Investig. Dermatol.* **97**, 340–344 (1991).
- [89] D. Fu, T. Ye, T. E. Matthews, J. Grichnik, L. Hong, J. D. Simon, and W. S. Warren, “Probing skin pigmentation changes with transient absorption imaging of eumelanin and pheomelanin,” *J. Biomed. Opt.* **13**, 054036 (2008).
- [90] I. R. Piletic, T. E. Matthews, and W. S. Warren, “Probing near-infrared photorelaxation pathways in eumelanins and pheomelanins,” *J. Phys. Chem. A* **114**, 11483–11491 (2010).
- [91] T. E. Matthews, I. R. Piletic, M. A. Selim, M. J. Simpson, and W. S. Warren, “Pump-probe imaging differentiates melanoma from melanocytic nevi,” *Sci. Transl. Med.* **3**, 71ra15 (2011).
- [92] C. V. Râman, “A new radiation,” *Indian J. Phys.* **2**, 387–398 (1928).
- [93] C. V. Râman and K. S. Krishan, “A new type of secondary radiation,” *Nature* **121**, 501–502 (1928).
- [94] G. S. Landsberg and L. I. Mandelstam, “New phenomenon in scattering of light (preliminary report),” *Journal of the Russian Physico-Chemical Society* **60**, 335 (1928).
- [95] R. W. Boyd, *Nonlinear optics* (Academic Press, San Diego, 2008), 3rd ed.
- [96] A. Zumbusch, G. R. Holtom, and X. S. Xie, “Three-dimensional vibrational imaging by coherent anti-Stokes Raman scattering,” *Phys. Rev. Lett.* **82**, 4142–4145 (1999).

- [97] J. P. R. Day, K. F. Domke, G. Rago, H. Kano, H. Hamaguchi, E. M. Vartiainen, and M. Bonn, “Quantitative coherent anti-Stokes Raman scattering (CARS) microscopy,” *J. Phys. Chem. B* **115**, 7713–7725 (2011).
- [98] J.-X. Cheng, A. Volkmer, L. D. Book, and X. S. Xie, “An epi-detected coherent anti-Stokes Raman scattering (E-CARS) microscope with high spectral resolution and high sensitivity,” *J. Phys. Chem. B* **105**, 1277–1280 (2001).
- [99] N. Dudovich, D. Oron, and Y. Silberberg, “Single-pulse coherently controlled nonlinear Raman spectroscopy and microscopy,” *Nature* **418**, 512–514 (2002).
- [100] T. Hellerer, A. M. Enejder, and A. Zumbusch, “Spectral focusing: High spectral resolution spectroscopy with broad-bandwidth laser pulses,” *Appl. Phys. Lett.* **85**, 25–27 (2004).
- [101] A. F. Pegoraro, A. Ridsdale, D. J. Moffatt, Y. Jia, J. P. Pezacki, and A. Stolow, “Optimally chirped multimodal CARS microscopy based on a single Ti:sapphire oscillator,” *Opt. Express* **17**, 2984–2996 (2009).
- [102] E. R. Andresen, P. Berto, and H. Rigneault, “Stimulated Raman scattering microscopy by spectral focusing and fiber-generated soliton as Stokes pulse,” *Opt. Lett.* **36**, 2387–2389 (2011).
- [103] O. E. Martinez, J. P. Gordon, and R. L. Fork, “Negative group-velocity dispersion using refraction,” *J. Opt. Soc. Am. A* **1**, 1003–1006 (1984).
- [104] I. Rocha-Mendoza, W. Langbein, and P. Borri, “Coherent anti-Stokes Raman microspectroscopy using spectral focusing with glass dispersion,” *Appl. Phys. Lett.* **93**, 201103 (2008).
- [105] B.-C. Chen, J. Sung, X. Wu, and S.-H. Lim, “Chemical imaging and microspectroscopy with spectral focusing coherent anti-Stokes Raman scattering,” *J. Biomed. Opt.* **16**, 021112 (2011).
- [106] C. Di Napoli, F. Masia, I. Pope, C. Otto, W. Langbein, and P. Borri, “Chemically-specific dual/differential CARS micro-spectroscopy of saturated and unsaturated lipid droplets,” *J. Biophotonics* **7**, 68–76 (2014).
- [107] A. F. Pegoraro, A. Ridsdale, D. J. Moffatt, J. P. Pezacki, B. K. Thomas, L. Fu, L. Dong, M. E. Fermann, and A. Stolow, “All-fiber CARS microscopy of live cells,” *Opt. Express* **17**, 20700–20706 (2009).

- [108] E. R. Andresen, P. Berto, S. Saint-Jalm, and H. Rigneault, “Stimulated Raman scattering microscopy by spectral focussing and fiber-generated soliton as Stokes pulse,” *Proc. SPIE* **8226**, 822606 (2012).
- [109] D. H. Whiffen, “Vibrational frequencies and thermodynamic properties of fluoro-, chloro-, bromo-, and iodo-benzene,” *J. Chem. Soc.* pp. 1350–1356 (1956).
- [110] C. M. Preston and W. A. Adams, “A laser Raman spectroscopic study of aqueous orthophosphate salts,” *J. Phys. Chem.* **83**, 814–821 (1979).
- [111] Y. Ozeki, F. Dake, S. Kajiyama, K. Fukui, and K. Itoh, “Analysis and experimental assessment of the sensitivity of stimulated Raman scattering microscopy,” *Opt. Express* **17**, 3651–3658 (2009).

Abstract

The implementation of nonlinear contrasts in an endoscopic scheme is highly desirable for biomedical applications. One of the issues that has to be overcome to realize a nonlinear endoscope is the propagation of ultra-short pulses in an optical fiber. Indeed, nonlinear processes require high peak powers in the focal volume in order to generate observable signals. Therefore, the pulses should have high energy, and be as short as possible, which makes them sensitive to the dispersion and nonlinearities of the optical fibers. This results in distortion and temporal broadening of the pulses. Most of the existing techniques of ultra-short pulses fiber-delivery rely on complex pre-compensation systems to counteract these effects. In this work, we explore the possibilities offered by the generation of high-energy solitons, launched by 800 nm pulses from a Ti:sapphire laser into a custom-built solid-core photonic bandgap fiber, for nonlinear microscopy and spectroscopy. Optical solitons have the remarkable property of preserving their shape when they propagate in a fiber, and their duration remains close to the minimum value physically allowed by their bandwidth, without the need of any pre-compensation. Moreover, the wavelength and delay of the soliton can be tuned by changing the power at the input of the fiber. Several soliton-based light sources were designed and realized, generating contrast in the most prevalent nonlinear microscopy modalities: two-photon excited fluorescence (TPEF), second-harmonic generation (SHG), coherent anti-Stokes Raman scattering (CARS), stimulated Raman scattering (SRS), and transient absorption. TPEF and SHG images of biological samples were first realized by taking advantage of the short duration of the solitons. By controlling the delay of the soliton, transient absorption measurements were then realized in a pump-probe configuration. Finally, the wavelength tunability of the soliton was used to generate the Stokes beam in a coherent Raman scattering setup based on the spectral focusing technique. The capabilities of this scheme were demonstrated by performing CARS and SRS microspectroscopy to monitor a chemical equilibrium in aqueous solutions.

Keywords : Nonlinear microscopy, nonlinear spectroscopy, fiber delivery, ultra-short pulses, photonic crystal fibers, photonic bandgap fibers, optical solitons.

Résumé

La mise en œuvre de contrastes non linéaires dans un mode endoscopique est d'un grand intérêt pour des applications dans le domaine médical. Un des problèmes à résoudre lors de la réalisation d'un endoscope non linéaire concerne la propagation d'impulsions ultra courtes dans une fibre optique. En effet, les processus non linéaires concernés nécessitent de grandes puissances d'excitation, réalisables seulement pour des impulsions de très courte durée, et de grande énergie, qui sont déformés et allongés par la dispersion et les non linéarités des fibres. La plupart des techniques d'illumination fibrées pour la microscopie non linéaire emploient des systèmes de pré-compensation pour neutraliser les effets de ces phénomènes. Dans ce travail, nous explorons les possibilités offertes par la formation de solitons de grande énergie, générés par l'éclairement d'une fibre à bandes interdites photoniques à cœur solide par un laser titane-saphir pulsé. Les solitons optiques ont la remarquable propriété de conserver leur forme lors de leur propagation dans la fibre, et leur durée reste proche de la valeur minimum définie par la limite physique imposée par leur largeur spectrale, sans avoir besoin de recourir à un système de pré-compensation. De plus, la longueur d'onde et le retard relatif des solitons peuvent être accordés en changeant la puissance lumineuse en entrée de fibre. Plusieurs sources de lumière ont été conçues et réalisées, pour générer de nombreux contrastes non linéaires, tels que la fluorescence à deux photons (TPEF), la génération de seconde harmonique (SHG), la diffusion cohérente Raman anti-Stokes (CARS), la diffusion Raman stimulée (SRS), et l'absorption transitoire. Des images d'échantillons biologiques ont tout d'abord été réalisées en tirant profit de la courte durée des solitons. Dans un second temps, des mesures d'absorption transitoire ont été menées dans une configuration pompe-sonde en contrôlant le retard des solitons dans la fibre. Finalement, un montage de CARS et SRS basé sur le principe de focalisation spectrale a été réalisé. Le décalage spectral du soliton a été mis à profit pour générer deux faisceaux synchronisés à deux longueurs d'onde différentes, utilisés par la suite comme faisceaux pompe et Stokes. L'utilité de ce montage a été démontré en suivant un équilibre chimique en solution aqueuse par des mesures de microspectroscopie CARS et SRS.

Mots-clefs : Microscopie non linéaire, spectroscopie non linéaire, illumination par fibre optique, impulsions ultra courtes, fibres à cristaux photoniques, fibres à bandes interdites photoniques, solitons optiques.